Faculty of Physics and Astronomy

University of Heidelberg

Diploma thesis in Physics

submitted by

Katharina Müller
born in Würzburg

2008

Diffusion-interaction analysis of heterochromatin protein 1 in the nucleus by fluorescence fluctuation microscopy

This diploma thesis has been carried out by **Katharina Müller** at the

BIOQUANT and DKFZ Heidelberg

under the supervision of

PD Dr. Karsten Rippe

and

Prof. Dr. Dr. Christoph Cremer,
Kirchhoff-Institute of Physics

Analyse des Diffusions- und Bindungsverhaltens von Heterochromatin Protein 1 im Zellkern mittels Fluoreszenz-Fluktuations-Mikroskopie

Die Mobilität und das Bindungsverhalten von Makromolekülen in lebenden Zellen wurde mit Methoden der Fluoreszenz-Fluktuations-Mikroskopie (FFM) untersucht. FFM ermöglicht die Analyse der räumlichen Verteilung fluoreszenz-markierter Proteine mittels konfokaler Laser-Scanning-Mikroskopie sowie die Untersuchung lokaler Beweglichkeit mittels fluorescence recovery after photobleaching (FRAP) und Fluoreszenz-Korrelations-Spektroskopie (FCS). Da FCS speziell für die Beobachtung schnell diffusiver Prozesse und FRAP zur Beobachtung langsamerer oder immobiler Teilchen geeignet ist, gewinnt man mit beiden Methoden komplementäre Informationen. Zur Auswertung der Messdaten wurden verschiedene mathematisch Modelle, die Diffusion, Bindung, Immobilisation und die Zugänglichkeit nuklearer Regionen berücksichtigen, herangezogen.

Die entwickelten Mess- und Analyse-Methoden wurden zur Untersuchung der DNA-Kompaktierung unter der Mitwirkung von Heterochromatin Protein 1 (HP1) im Zellkern herangezogen. Mit FCS- und FRAP-Messungen konnten drei unterschiedlich mobile HP1-Komponenten nachgewiesen werden: ein Anteil stark beweglicher HP1-Moleküle, transient gebundene Moleküle und ein kleinerer Anteil, der stabil in die dichteren Chromatinstrukturen integriert ist. Auf diesen Ergebnissen basierend wurde eine quantitative Beschreibung der HP1-Dynamik im Bezug auf die Diffusionskoeffizienten, Dissoziationskonstanten und den unterschiedlichen Bindungsstellen herausgearbeitet.

Diffusion-interaction analysis of heterochromatin protein 1 in the nucleus by fluorescence fluctuation microscopy

For analyzing the mobility and interaction behavior of macromolecules in living cells a fluorescence fluctuation microscopy approach was applied. It comprised an analysis of the spatial distribution of fluorescent molecules by confocal laser scanning microscopy and probing their local mobility with fluorescence recovery after photobleaching (FRAP) and fluorescence correlation spectroscopy (FCS). Because FCS is restricted to rapidly diffusing molecules and FRAP to the observation of slower or even immobile particles, they yield complementary information. For the analysis, different mathematical models including diffusion, binding, immobilization and accessibility were combined.

The developed measurement- and analysis-methods were used to investigate the compaction of DNA in the nucleus of living cells via heterochromatin protein 1 (HP1). FCS and FRAP revealed three fractions of HP1-molecules with different mobility: A highly mobile fraction of HP1, transiently bound molecules and a small fraction of HP1 stably incorporated into dense chromatin structures were observed. Based on these data a quantitative description of HP1 in terms of its diffusion coefficient, kinetic off-rate and its different types of binding sites was obtained.

Table of Contents

List of Figures

List of Tables

Introduction

All processes that access the DNA information in the cell nucleus, like DNA replication and repair, gene transcription and recombination, depend on an efficient transport of molecules to its target sites (Cremer and Cremer, 2001; Wachsmuth, 2001; Wachsmuth et al., 2008b). These processes also involve the formation of supramolecular protein complexes and the interaction of proteins with DNA or chromatin, which itself consists in a DNA-protein-complex. Understanding these transport and interaction mechanisms, in a quantitative manner is important to understand the fundamental cellular mechanisms (Elson, 2001; Wachsmuth, 2001). For *in vivo* experiments that address these questions, non-invasive methods based on optical microscopy can be applied (Heuvelman, 2008; Wachsmuth et al., 2008b). In some methods the fluorescence distribution is disturbed and the redistribution back to the equilibrium state is observed. The recovery data contain information about diffusion and binding processes of these proteins. In this fluorescence recovery after photobleaching (FRAP) method only the distribution of fluorescent labels gets altered, the proteins under investigation do not get damaged and work in their natural way. However, this method is limited in its temporal resolution to the imaging rate of the microscope and information about faster movements is lost. An alternative approach for studying protein dynamics is based on fluctuation measurements (Heuvelman, 2008; Wachsmuth, 2001), and is referred to as fluorescence correlation spectroscopy (FCS). Based on the analysis of temporally resolved fluctuations of the number of particles within a microscopic observation volume, parameters for particle concentration and their hydrodynamic properties can be estimated by autocorrelation analysis. An advantage of fluorescence correlation spectroscopy is its high local and temporal resolution. Both FRAP and FCS are based on a fluorescence microscopy setup and were combined to the so-called fluorescence fluctuation microscopy (FFM). FRAP and FCS technology can be applied to study mechanisms of DNA packaging in living cells.

On the level of microscopic analysis, chromatin can be divided into two compaction states: The less condensed euchromatin with most of the actively transcribed genes, and the highly condensed heterochromatin that includes gene loci that are mostly suppressed. This compartmentalization is achieved by properly controlled heterochromatin formation, propagation and maintenance. Two prominent marks of the highly compacted heterochromatin are the methylation at lysine 9 of histone H3 and the accumulation of heterochromatin protein 1 (HP1), which recognizes this posttranslational histone modification established by the histone methyl transferase Suv39h1. With its ability to bind a lot of other chromatin modifying proteins HP1 serves as an assembling platform in heterochromatin formation and being able to form a dimer, it is adequate to stabilize the condensed chromatin structure due to crosslinking nucleosomes.

In this thesis FRAP and FCS were applied to investigate the diffusion and interaction behavior of heterochromatin protein 1 in the cell nucleus. The understanding of mobility and interaction behavior of these macromolecules within the nucleus is important to learn about their functionality in chromatin organization. As HP1 is a multifunctional protein and takes part in a lot of different regulatory processes (Chapter 1) it is of major interest to investigate its intranuclear mobility and reaction kinetics spatially resolved. Background information on the underlying biological system, HP1 and chromatin organization, are given in Chapter 1. The following Chapter 2 describes the basics of microscopy and the basics about diffusion. In the first part of Chapter 3, it is described how the biological system of cells expressing the fluorescently tagged protein HP1 was established, furthermore, the design of adequate experimental protocols for combined fluorescence recovery after photobleaching measurements and fluorescence correlation spectroscopy is reviewed. Further on, the optimization of analysis methods for FRAP and FCS data, adjusted to the biological system, and the results are presented (Chapter 4). Comments on analysis methods and the combination of diverse measurement methods as well as the application of experimental results to create a kinetic model for HP1 within the nucleus, are given in Chapter 5.

1. Biological background

1.1. Chromatin organization

The whole genetic information of an organism is stored in the DNA (deoxyribonucleic acid) sequence. The human genome encodes ~24000 genes on the DNA chain with a total length of about 2 m. This amount of DNA is packed into a cell nucleus with about 10 – 20 µm in diameter.

This compaction is obtained via the DNA organization into chromatin. Chromatin describes the complex consisting of DNA and associated proteins (van Holde, 1989). The fundamental subunit of chromatin is the nucleosome, that consists of 146 DNA base pairs (bp) wrapped 1.67-fold around an octamer of strongly positively charged histone proteins H2A, H2B, H3 and H4 (two copies each) (Knippers, 1997). These highly conserved core histones contain a globular domain and flexible histone tails that protrude from the surface of chromatin polymer and provide exposed interaction sites for other proteins. Wrapping the DNA around the histones and connecting the neighboring nucleosomes by a short linker DNA, leads to a five- to tenfold compaction of the DNA in a 'beads on a string'-like structure (Fig. 1.1).

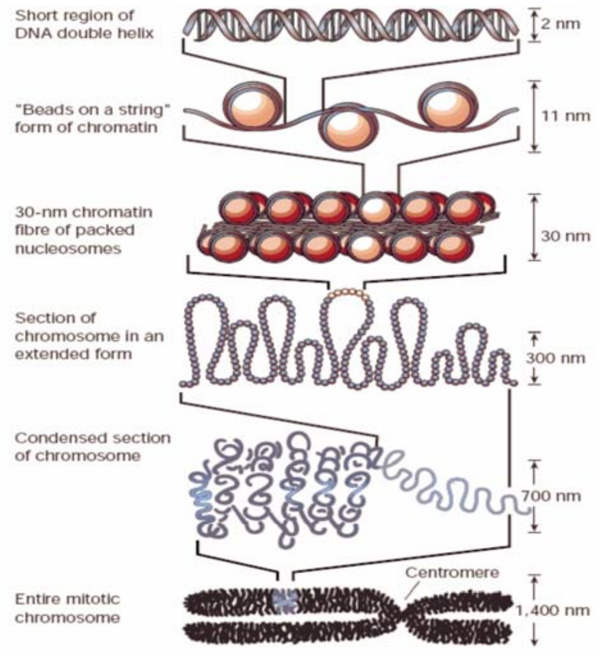

Figure 1.1: Organization levels of DNA within the chromatin structure. A first compaction of DNA is reached by nucleosomes forming 'beads on a string'. Histone H1 and other non-histone proteins stabilize a fiber of 30 nm in diameter. Further folding into higher order structures up to the mitotic chromosome structure is expected, but details of folding are still unknown. Image adapted from (Felsenfeld and Groudine, 2003).

A higher compaction (~50-fold) into a 30 nm diameter fiber is reached with the contribution of a fifth, so-called linker histone H1, that stabilizes each nucleosome and organizes the stretches of linker DNA, and other non-histone proteins (Zlatanova and van Holde, 1996).

The 30 nm fiber itself forms higher order structures up to the mitotic chromosome. This is supposed to happen due to folding and spiral shaped compaction, but details of folding are still unknown.

Although this high compaction ratio organizes the DNA in the nucleus, the genetic information has to remain accessible for processes like replication, transcription and repair. To fulfill these apparently contradicting requirements, interactions of proteins and DNA in the chromatin, have to be regulated in a dynamic manner to allow access to the DNA.

Euchromatin and Heterochromatin

Within the chromatin structure two different types of domains can be distinguished: One less condensed, gene rich and transcriptionally active structure, named euchromatin, and the highly condensed, inaccessible, gene poor heterochromatin, which is much less active in transcription. A first distinction between both subtypes was made because of different compaction levels during cell cycle based on observations in light microscopy (Heitz, 1928). Heterochromatin stays in a highly compacted state even during interphase, whereas euchromatin decondenses. Further investigation revealed, that heterochromatin is characterized by a high density of repetitive DNA elements and has several marks that are stable over cell generations: A high level of DNA-methylation and a typical profile of covalent modifications on amino-terminal histone tails, especially methylation of lysine residues 9 and 27 of histone H3 (H3K9me and H3K27me) and K20 of histone H4 (H4K20me), as well as low histone acetylation are observed. Furthermore, these chromatin domains are associated with different higher-order condensation levels and differ in nuclear organization (Grewal and Elgin, 2007). Heterochromatin is located in large blocks at centromeres and telomeres and smaller heterochromatin domains are distributed throughout the chromosomes. The blocks flanking the centromeres are known as pericentric regions. In mouse cells these regions form cluster and are intensely stained by 4’,6-diaminidino-2-phenylindole (DAPI). Besides repression of transcription, the role of heterochromatin includes the maintenance of genome stability, the regulation of gene expression during development and cellular differentiation as well as the stable maintenance of expression states through cell divisions (Grewal and Moazed, 2003; Maison and Almouzni, 2004).

1.2. Histone modifications and histone modifier

Posttranslational modifications of histones

Amino-terminal histone tails, protruding from the nucleosome, are subject to a variety of posttranslational covalent modifications, e.g. acetylation, methylation, ubiquitylation etc. of single amino acids. More than 60 residues on histone tails can be modified in different ways (e.g. mono-, di- or trimethylation), offering an enormous potential for functional responses (Kouzarides, 2007).

The different types of modifications and their positions on the histones were identified in the early years of chromatin research (van Holde, 1989). Their interaction with proteins and their impact on chromatin conformation, and therefore gene-activity, recently lead to the so-called 'histone-code' hypothesis and is still a topic of recent research (Jenuwein and Allis, 2001; Strahl and Allis, 2000). This hypothesis predicts that modifications interact in a synergistic, complementary, or antagonistic way and introduce interaction affinities for regulatory proteins. Euchromatin and heterochromatin conformations are dependent on local concentration and combination of modified nucleosomes. Especially histone acetylation and histone methylation play a fundamental role in regulation of transcriptional activity. The histone code is implemented by a large number of enzymes like histone methyl transferases (HMTase, e.g. Suv39h1) or histone acetyl transferases (HAT) and their counterparts that remove the modification marks when necessary, e.g. histone demethylases (HDM) or deacetylases (HDAC) etc. Most modifier enzymes are highly specific for one distinct histone and for a particular amino acid position. Even today not all histone modifying enzymes have been discovered.

There are different possibilities how histone modifications can influence the organization level of chromatin. Histone modifications can affect the contacts between different histones in adjacent nucleosomes or of histones and DNA (Rippe et al., 2008). Acetylation, for example, neutralizes the basic charge of lysine and therefore weakens electrostatic interactions. Histone modifications can also regulate the access to the underlying DNA. Furthermore, the modification marks could provide binding sites or induce the recruitment of effector proteins, therefore appropriate protein motifs evolved that recognize distinct histone modifications (Kouzarides, 2007). Proteins that form chromo-domains (as heterochromatin protein 1), for example, interact selectively with methylated histones.

Suv39h1, HP1 and LSD1

The HMTase, Suv39h1, and heterochromatin protein 1 (HP1) are highly negative regulators of position dependent gene activity and therefore prominent heterochromatin proteins in conjunction with H3K9 methylation. The lysine specific demethylase 1 (LSD1) was the first enzyme discovered to remove methylation marks from histone tails and thus discarded the hypothesis of a permanent histone methylation.

Suv39h1 exhibits an essential role in initial steps of heterochromatin formation by selective tri-methylation of H3K9 (Rice et al., 2003; Schotta et al., 2002) and therefore provides a binding platform for HP1 (Eskeland et al., 2007). This highly conserved HMTase Suv39h1 combines two prominent functional domains of chromatin modifiers, the chromo-domain used for chromatin binding and the SET-domain (acronym of its most important representatives Su(var)3-9, Enhancer-of-zeste and Trithorax (Schneider et al., 2002)) that exhibits the HMTase enzymatic activity. The amino-terminus serves as an interaction domain with other proteins, e.g. HP1. The mechanism by which Suv39h1 is recruited to and interacts with chromatin is unknown, but the RNAi (ribonucleic acid interference) pathway has been suggested to account for initial recruitment (Grewal and Elgin, 2007). Further attachment and restriction to heterochromatin is at least partly dependent on HP1. Because Suv39h1 is relatively stably associated to chromatin, a structural role (beside its catalytical role) of this protein in heterochromatin was assumed by (Krouwels et al., 2005).

A second major structural factor of heterochromatin is heterochromatin protein 1. HP1 is evolutionary highly conserved and homologues were found from yeast, *S. pombe* (Swi6), to mouse (M31, mHP1) and human (HP1) (Hiragami and Festenstein, 2005; Maison and Almouzni, 2004). In mammals three HP1 isoforms are known: HP1α, HP1β, and HP1γ, which have similarities in the amino acid-sequence and structural organization, but differ in their nuclear localization. The most dominant species HP1α and HP1β are primarily, but not exclusively associated with heterochromatin and colocalize in mouse cells, whereas HP1γ localizes predominantly in euchromatin and is completely excluded from pericentric heterochromatin (Dialynas et al., 2007; Maison and Almouzni, 2004; Minc et al., 1999). Factors that determine spatial and functional specialization are still unknown.

All HP1s contain an amino(N)-terminal chromo-domain (CD) and a carboxy(C)-terminal chromoshadow-domain (CSD). Both domains are connected by a flexible and less conserved hinge-region. The CD interacts specifically with the histone H3 tri-methylated at lysine 9. This binding is an important step for the initialization of heterochromatin formation. Although recognition of H3K9me3 by the CD is crucial for heterochromatin, HP1 binding to this site is not sufficient to ensure heterochromatin stability, and further binding interactions seem to be necessary (Eskeland et al., 2007; Maison and Almouzni, 2004). Recently, the linker histone variant H1.4 was reported to be a new binding partner to the CD (Daujat et al., 2005). A putative function of the hinge region is binding of RNA, DNA or chromatin. The less conserved hinge was supposed to direct the different HP1 isoforms to the different target loci. HP1 is able to form homo- or heterodimers among or between different isoforms. The self-association of HP1 is referred to the CSD domain. Furthermore, the CSD is also critical for correct binding of HP1 to chromatin and mediates protein-protein-interactions with HP1-associating proteins, amongst them Suv39h1 (Brasher et al., 2000; Hiragami and Festenstein, 2005). The interaction of Suv39h1 with HP1 depends on HP1-dimerization (Yamamoto and Sonoda, 2003). The connection between HP1 and Suv39h1 is an important aspect in heterochromatin spreading and maintenance. It is thought that HP1 provides an assembling platform for various proteins, which either set epigenetic marks or promote nucleosome assembly. A summary of proteins cooperating with HP1 is given in Fig. 1.2 (Hediger and Gasser, 2006; Hiragami and Festenstein, 2005).

In the current model, heterochromatin assembly is nucleated by the initial recruitment of HP1 due to tri-methylation of H3K9 by Suv39h1. Once bound to chromatin, HP1 recruits further histone modifying enzymes, among others again Suv39h1. This feedback loop creates HP1 binding sites on adjacent nucleosomes. This mechanism allows the maintenance of heterochromatin as well as heterochromatin spreading to adjacent chromatin regions (Grewal and Moazed, 2003). The formation of HP1-dimers generates a cross-linker and stabilizes the higher order structure (Jenuwein and Allis, 2001). Further stabilization of HP1 binding and therefore heterochromatin compactness is given by noncoding (nc)RNAs; experiments with the ribonuclease (RNase) A revealed a RNA- and histone modification-dependent structure of H3K9-tails required for HP1 accumulation (Maison et al., 2002; Muchardt et al., 2002; Rodriguez-Campos and Azorin, 2007). Methylation independent binding of HP1 to histones

H1 and H3 can also be involved in heterochromatin formation and maintenance (Schmiedeberg et al., 2004). A H3-methylation independent binding of HP1 occurs with the globular domain of H3 (Nielsen et al., 2001).

This model implies a stable and specific binding of HP1 to heterochromatin. However, HP1 is highly mobile and infrequent turnover in both euchromatin and heterochromatin occurs (Cheutin et al., 2003; Festenstein et al., 2003; Schmiedeberg et al., 2004). In vitro binding studies revealed only weak interaction and low occupancy times of HP1 at binding sites (Eskeland et al., 2007).

Furthermore, although HP1α and β are concentrated at pericentric heterochromatin, they are also found in euchromatin. Here they are thought to exert repression of euchromatic genes. Silencing effects in euchromatin seem to be short-ranged with HP1 forming a small repressive chromatin structure that resembles heterochromatin (Hiragami and Festenstein, 2005). Interestingly, it was discovered that gene repression in the less condensed chromatin can partially be executed independently from Suv39h1 (Hediger and Gasser, 2006). One intriguing difference in euchromatic gene repression by heterochromatin proteins is, that silencing is localized to specific loci or single nucleosomes, and a spreading mechanism like in heterochromatin seems not to exist (Grewal and Moazed, 2003). Interaction partners of HP1 in euchromatin are H3K9me2 and H3K9me3, euchromatic HMTases as well as the heterochromatic HMTase Suv39h1, and probably ncRNAs, linker histone H1 and the globular domain of H3.

The initial definition of HP1 as gene repressor had to be changed, when observations were made that HP1 is involved in gene activation even in heterochromatin and again works independently from Suv39h1, at least in some cases (Hiragami and Festenstein, 2005). The more detailed research was carried out, the more functions of HP1 have been discovered. A summary of the recent state of research is given in Fig. 1.2.

Figure 1.2: Summary of putative functions of HP1. **A** HP1-dimers cross-link H3K9-methytlated nucleosomes to form heterochromatin, interaction of HP1 with the HMTase (and HDAC) creates a positive feedback-loop for heterochromatin formation and maintenance. **B** Binding of HP1 to a transcriptional repressor and attachment to specific loci represses gene expression in euchromatin, this could be supported by euchromatic or heterochromatic histone modifiers. **C** Gene repression by HP1 at a single nucleosomal level. **D** Gene repression due to hindrance of association of the general transcriptional machinery by HP1 in complex with a TATA-binding protein associated factor. **E** Genes silenced by heterochromatin formation get attached to the nuclear periphery, this process is possible by interaction of HP1 with lamin B or other membrane components. **F** HP1 gets recruited to the replication fork in late S-phase of the cell cycle and presumably is responsible for both heterochromatin integrity (especially at centromeres and telomeres) and the epigenetic status of silenced genes. **G** During mitosis chromatin bound HP1 is responsible for the loading of sufficient cohesin complexes to centromeres for chromosomal segregation. **H** Interaction of HP1 with transcriptional activators and (H3K9me-dependent or independent) recruitment of this complex to a specific site of a gene induces active transcription. **I** Due to binding on nascent mRNA, HP1 stabilizes the RNA. Illustration taken from (Hiragami and Festenstein, 2005).

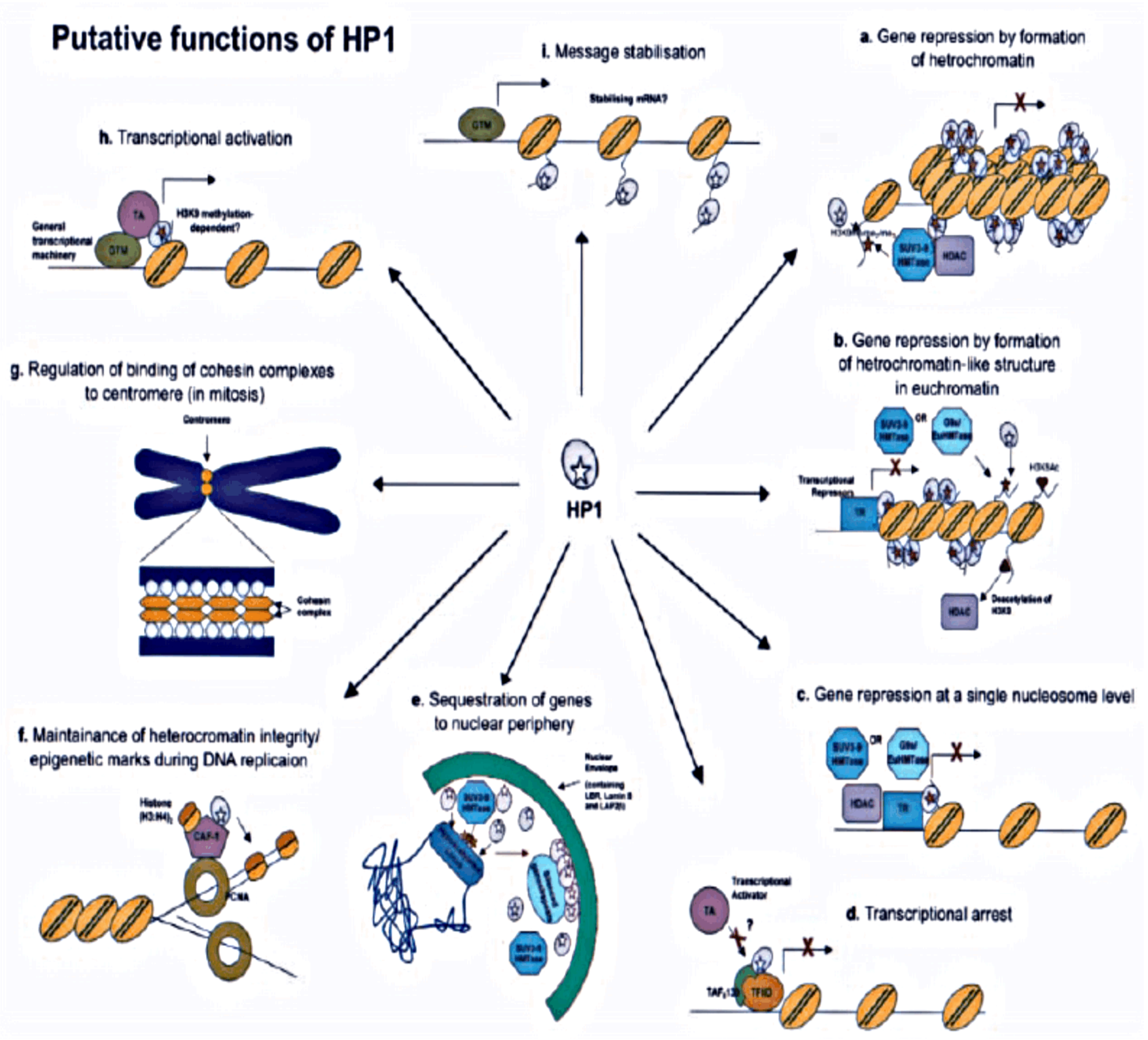

Chromatin methylation requires a balanced coordination of histone methylation and demethylation. Many years the methylation of histones was thought to be irreversible, until recently the first lysine specific demethylase, LSD1, was identified and described as a component of the co-repressor complex CoREST (Gamble and Kraus, 2007; Metzger et al., 2005). The enzyme consists in a centrally located SWIRM domain that regulates protein-protein-interaction and a C-terminal amine oxidase domain that harbors the demethylase activity (Metzger et al., 2005). In combination with CoREST, LSD1 demethylates mono- or dimethylated H3K4, i.e. methylation sites that are associated to an activated transcriptional state and therefore by eliminating these marks, LSD1 is involved in gene repression. But other proteins that associate with LSD1 like the androgen receptor (AR) appear to alter the specificity of LSD1 for H3K4 to H3K9 and thereby alter the repressor to an activator (Bannister and Kouzarides, 2005). More active genes than inactive genes were found associated with LSD1 (Garcia-Bassets et al., 2007). Thus, LSD1 is even more important for gene activation than gene repression. As a co-activator of AR, LSD1 correlates with H3K9me1 and H3K9me2 demethylation, both marks are associated with repressed genes. But LSD1 and AR do not influence the prominent heterochromatin mark H3K9me3. The first tri-demethylase was discovered recently and identified as JMJD2C. Interaction of ligand bound AR and JMJD2C demethylates H3K9me3 and in cooperation with LSD1 stimulate gene transcription (Wissmann et al., 2007).

1.3. Mobility in the mammalian nucleus

The mammalian nucleus is confined by a double-membrane structure, the nuclear envelope, and separates the genome from the cytoplasm; furthermore, it spatially separates nuclear and cytoplasmic processes. The nucleus is highly organized into various subcompartments or organelles, like nucleoli, speckles or nuclear bodies etc. that fulfill specific biological activities (Rippe, 2007). In total, the cell nucleus is densely packed with macromolecules at a concentration of ~200 mg/ml.

Within the nucleus each chromosome occupies a distinct region, the so-called ‘chromosome territory’ (CT) (Cremer and Cremer, 2001; Cremer and Cremer, 2006). Within whole chromosomes, sub-structures with a length of about 1 Mb (10^6 bases) and a diameter of 400 – 800 nm are observed, which are spatially and temporally stable except of constrained

Brownian motion. Experimental observations lead to a CT-IC-model (chromosome territory – interchromosomal space), which postulates a complex, folded structure that leads to a largely expanded surface with IC channels that penetrate into CT. Gene regulation is additionally influenced by accessibility for transcription-complexes, that are ‘stored’ within IC areas, to chromatin domains. Small molecules are able to intrude into the CT. A more quantitative approach offers the multiloop subcompartment (MLS) model, which describes the assembly of ~1 Mbp (10^6 base pairs) structures by folding a 30 nm-fiber into loops of roughly 50 – 100 kb forming a rosette.

Translocation of chromatin loci was measured and a relatively slow and confined movement in agreement with territorial organization of chromosomes was reported. As a part of larger chromatin domains an accessible region of 200 – 300 nm and an apparent diffusion coefficient of $1\cdot10^{-4} - 2\cdot10^{-4}$ µm²/s were reported (Görisch et al., 2005).

The motion of inert molecules within the nucleus (as well as in cytoplasm) is due to diffusion in the nucleoplasm that exhibits a 3.1-fold higher viscosity than water (Beaudouin et al., 2006; Pack et al., 2006). Nuclear organelles and chromatin fibers are recognized by the molecules as a network of obstacles; no difference in the level of hindrance between IC and CT regions was found (Wachsmuth, 2001). In contrast to inert molecules, reactive proteins can (transiently) bind to chromatin and only the unbound fraction is purely diffusive. This leads to a complex relation between mobility, accessibility and interactions of chromosomal proteins, like HP1, in the nucleus (Wachsmuth et al., 2008a). Non-invasive fluorescence microscopy based methods are predestined to reveal these parameters in living cells. In the following chapters, the framework for the experimental application as well as the theoretical analysis for this are described.

2. Physical fundamentals

2.1. Fluorescence microscopy for *in vivo* imaging of cells

2.1.1. Bright-field microscopy, resolving power and numerical aperture

To be able to resolve structures smaller than that seen by eye (resolution limit ≈ 70 µm) in the 16th/17th century the first light microscopes were developed and used for observational research by A. van Leuwenhoek and R. Hooke. The simplest setup for a bright field microscope just contains two lenses: The objective displays the object as heightened but inverted picture at the intermediate image plane, from where the intermediate image is amplified and inverted again by the ocular that works like a magnifying glass. Recently used microscopes are so called infinity-corrected microscopes and contain an additional tubular lens.

The resolving capacity of a microscope is defined by the minimum distance d_{min} of two resolvable points and obeys the Rayleigh criterion:

$$d_{\min} = 1.22 \cdot \frac{\lambda}{2 \cdot NA} \tag{2.1}$$

where λ means the wavelength and NA the numerical aperture. The numerical aperture of an objective is a measure of the range of angles over which it can collect light and thus indicates its resolving power. As a characteristic value of the objective the NA is defined as:

$$NA = n \cdot \sin\alpha \tag{2.2}$$

n according to the refraction index of the surrounding media (air: n = 1, water: n = 1.33 or immersion oil: n = 1.5) and 2α to the aperture angle of the objective. With regard to these criteria a good resolution can be achieved using short wavelength and objectives with high NA.

Many samples especially from living materials provide insufficient contrast and remain essentially invisible with bright-field microscopy. Therefore, contrast-enhancing techniques were developed, e.g. phase contrast microscopy or differential interference microscopy as well as fluorescence microscopy.

In this work only fluorescently labeled probes were investigated and therefore just fluorescence microscopy is discussed here. Bright-field microscopes and fluorescence microscopes are similar in their setup, yet the latter is extended with an excitation filter and an emission filter as well as with an additional dichroic mirror (Fig. 2.1). The first filter is located directly behind the light source and selects only the light with the excitation wavelength of the used fluorophore (alternatively a monochromatic laser light source can be chosen). The dichroic mirror directs the excitation light beam to the sample and the red-shifted emission light (see Chapter 2.1.2.) passes through this mirror directly to the detector. A second filter in front of the detector constrains the light to the wavelength of the red-shifted emission light and blocks light of the excitation frequency.

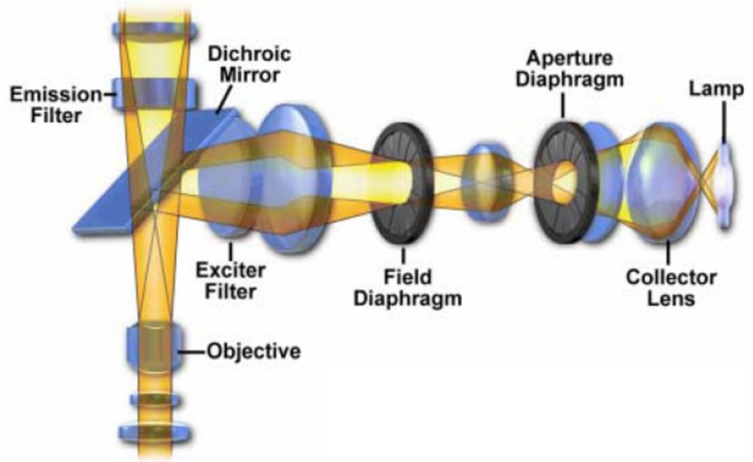

Figure 2.1: Schematic illustration of a fluorescence microscope setup, including excitation and emission filter and a dichroic mirror. Figure taken from (Davidson and Abramowitz, 1999)

2.1.2. Fluorescence

In a fluorophore-molecule different electronic states with discrete energy values exist (each of them split up into vibrational levels). Excitation of the fluorophore, by irradiation with photons of appropriate energy $E = h \cdot \nu$, raises the system from ground state S_0 to an excited state S_1, mostly also into higher vibrational levels of S_1 (transitions into higher states obey the so called Franck-Codon principle). Excited states are highly instable: Within picoseconds (10^{-12} s) vibrational relaxation takes place and upon returning to the ground state the emission of a fluorescence photon occurs on the timescale of a nanosecond (10^{-9} s). Further vibrational relaxation leads to the lowest energy state. No radiation, but heat is emitted during these vibrational relaxation steps. All processes can be illustrated in a so-called Jablonski-diagram (Fig. 2.2).

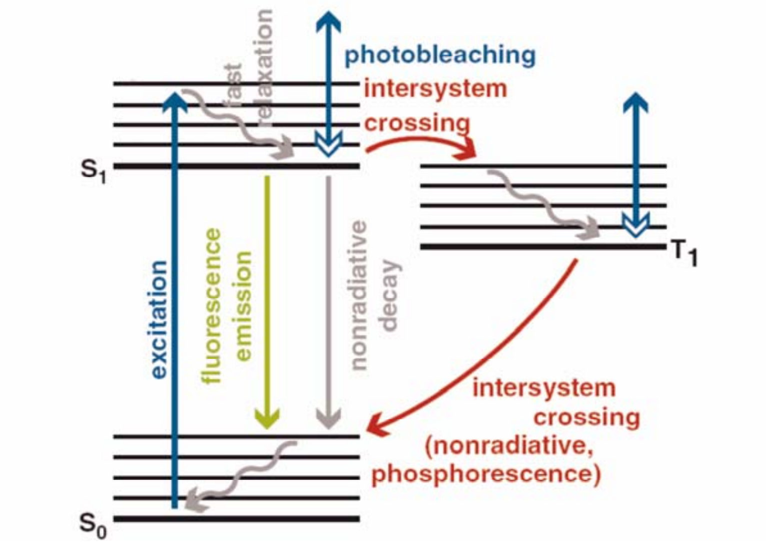

Figure 2.2: Jablonski-diagram of a fluorophore. Processes involved in fluorescence photon emission are illustrated. Image adapted from (Wachsmuth and Weisshardt, 2007)

This diagram also shows relaxation processes competing with fluorescence emission. Direct, non-radiative decay can be attributed to internal conversion processes, whereas intersystem crossing leads the system to the triplet state T_1. Relatively long lifetimes (about 10^{-6} s) of this triplet state excludes the fluorophore from the fluorescence cycle and is therefore called dark state. Final deactivation back to S_0 occurs either radiationless or due to emission of a phosphorescence photon (Wachsmuth and Weisshardt, 2007). A complete abortion of the fluorescence cycle can happen due to photobleaching when the fluorophore is illuminated over long terms or with too high intensity. Irreversible oxidation and conformational changes of molecules within an excited state are potential reasons for photobleaching. Reversible photobleaching or blinking can be observed especially at high intensity illumination when an excited fluorophore absorbs a second photon and is shifted to a higher excitation state. The lifetime of such a phenomenon lies between microseconds and seconds.

Another important aspect of fluorescence, that is apparent from the Jablonski-scheme, is the occurrence of the so-called Stokes-shift. Emitted light always carries a lower energy than the excitation photons. Because lower energy is equivalent to longer wavelength ($\Delta E = h \cdot \nu = h \cdot c / \lambda$) the emitted photon is shifted to a longer wavelength, the so-called red-shift. Fluorescence microscopy uses this displacement in wavelength to split excitation and emission light beams by dichroic mirrors and filter.

Sometimes it is possible to access the intrinsic fluorescence of a material like in animals or plants (primary or autofluorescence), but mostly it is necessary to label the samples with fluorescent dyes so that they show a so-called secondary fluorescence. Fluorescent probes can be used to label target structures in fixed cells (e.g. immunostaining or fluorescence in situ hybridization (FISH)), for *in vivo* imaging, they can be fused to genes and brought into the cell where they are expressed and located together with the encoded protein. Hundreds of fluorescent reporters are known that differ in intensity of fluorescence and quantum yield, in excitation and emission spectra, and their target specificities (Davidson and Abramowitz, 1999).

In Fig. 2.3 the spectra of the used fluorescent proteins GFP and TagRFP are shown. The wild type of green fluorescent protein ((wt)GFP) is a direct descendant of the jellyfish *Aequorea victoria* and transforms the blue light of the chemiluminescent protein Aequorin into green fluorescence (Tsien, 1998). GFP is the best characterized autofluorescent protein, its spectral properties were enhanced by mutation of distinct amino acids (enhancedGFP, EGFP). Since GFP can be fused to proteins *in vivo* and due to its high fluorescence quantum yield and photobleaching properties, it is well suited for imaging and measurements in living cells. The wild type of red fluorescent protein, RFP, stems from the sea anemone *Entacmaea quadricolor.* TagRFP was generated as very bright monomeric red fluorescent fusion protein (Merzlyak et al., 2007).

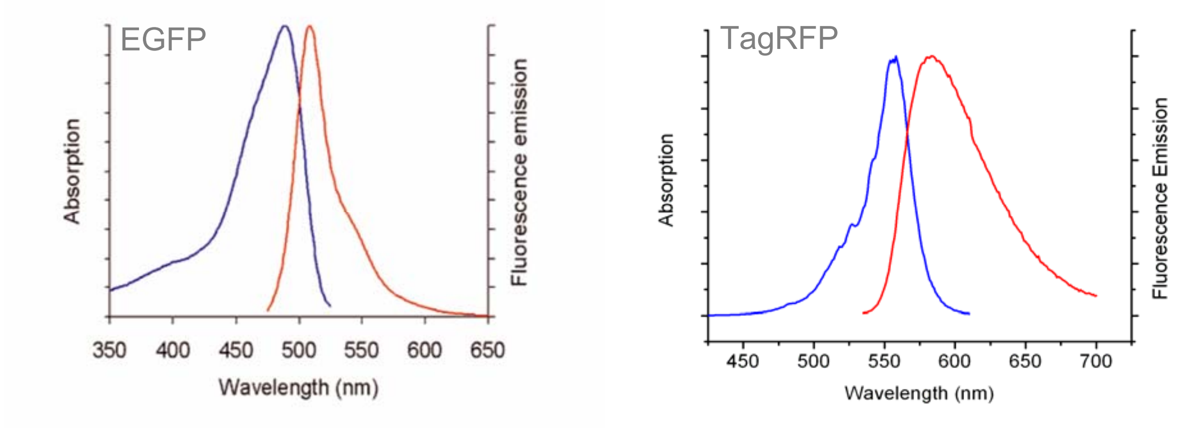

Figure 2.3: Absorption (blue) and emission (red) spectra of EGFP and TagRFP. Data from http://probes.invitrogen.com and http://www.evrogen.com/.

2.1.3. Confocal laser scanning microscopy

In wide-field fluorescence microscopes, as described above, the whole specimen is illuminated. Accordingly, not only fluorophores in the focal plane, but also fluorophores below and above the focal plane are excited and emit photons that could reach the detector. Thick specimen produce quite much of this ‘out-of-focus’ light (about 80 %), and this in turn contributes to a blurred background that distorts contrast and sharpness of the final image (Murray, 2005).

An optical setup that excludes the out-of-focus light from the final image was first described and patented by M. Minsky in 1957 (Minsky, 1957). He obtained astonishing sharp and highly detailed images from thick samples after insertion of a pinhole aperture into the optical path. Placed in front of the detector it rejected the light emerging from points above or below the focal plane. Only light from a central spot of the focal plane can pass the aperture. This is schematically described in Fig. 2.4.

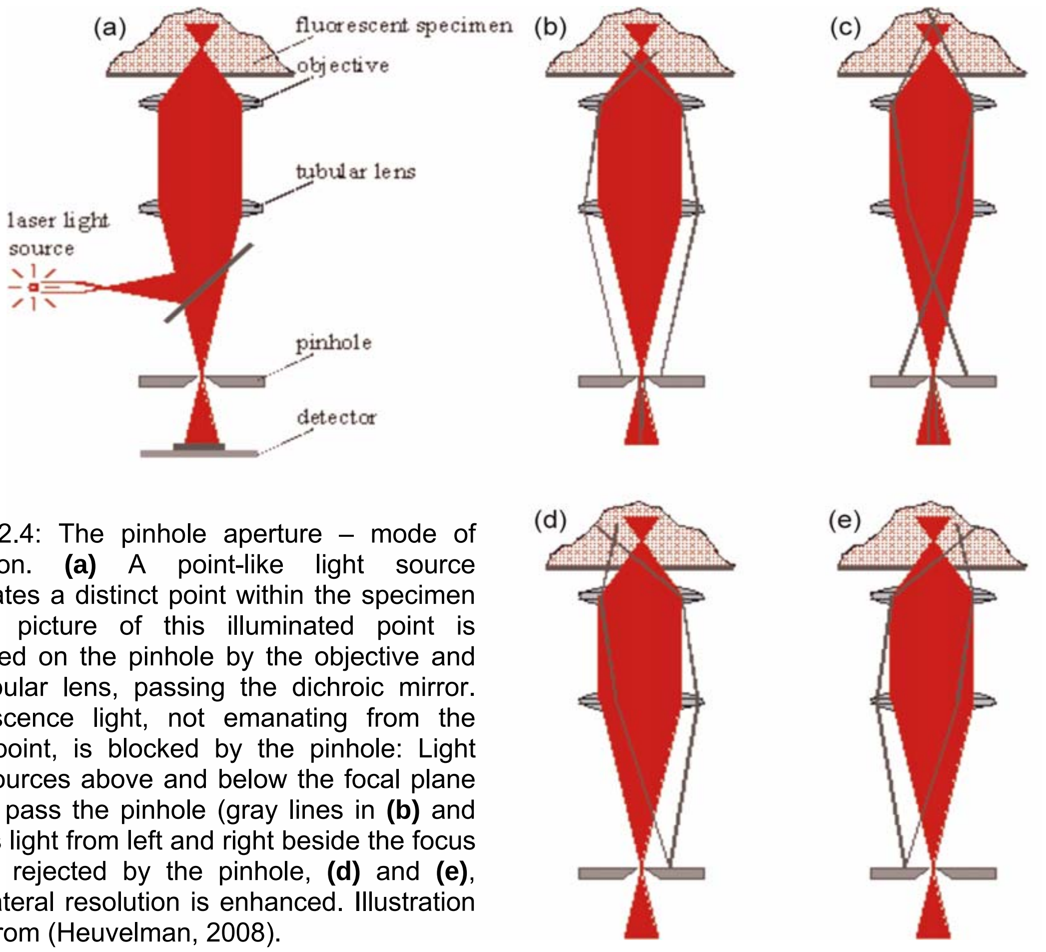

Figure 2.4: The pinhole aperture – mode of operation. **(a)** A point-like light source illuminates a distinct point within the specimen and a picture of this illuminated point is displayed on the pinhole by the objective and the tubular lens, passing the dichroic mirror. Fluorescence light, not emanating from the focus point, is blocked by the pinhole: Light from sources above and below the focal plane cannot pass the pinhole (gray lines in **(b)** and **(c)**). As light from left and right beside the focus is also rejected by the pinhole, **(d)** and **(e)**, even lateral resolution is enhanced. Illustration taken from (Heuvelman, 2008).

As only the central spot of the specimen is visible through the aperture, there is no need to illuminate the whole area of the probe. Using a second pinhole aperture directly behind the light source or using a point-like source instead, and therefore illuminating just a small focal volume has advantageous side effects: Contrast is further enhanced reducing scattered light from other parts of the specimen, photobleaching is minimized and the vertical resolution is improved (Murray, 2005). To obtain confocal images of larger regions of interest (ROI) the focal spot has to be scanned in a raster pattern over the specimen. Applying confocal microscopy one is able to image thin layers of a thick specimen, a method known as optical sectioning. Due to improved axial resolution also a three dimensional reconstruction of the probe is possible by assembling a z-stack of two dimensional (x-y-) images of successive focal planes.

With the progress in computer and laser technology as well as further development of new fluorophores, the confocal technique expanded also to fluorescence microscopy and ended up in CLSFM, confocal laser scanning fluorescence microscopy (Cremer and Cremer, 1978; Davidson and Abramowitz, 1999). Today fluorescence microscopy is mostly done using confocal laser scanning microscopes and therefore below is simply referred to as CLSM. The design of a confocal laser scanning microscope is shown in Fig. 2.5.

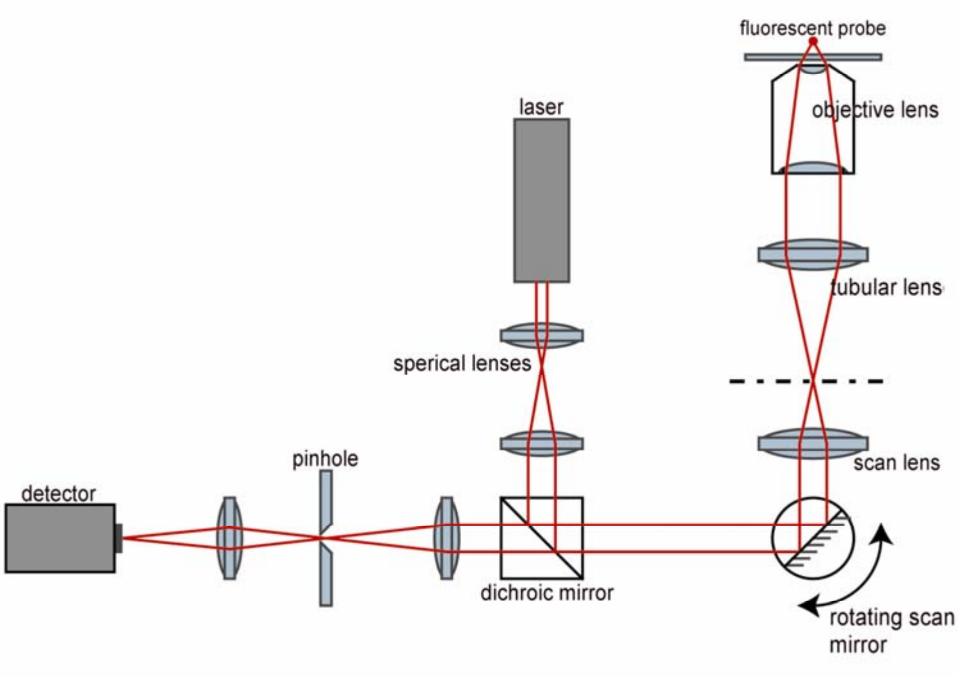

Figure 2.5: Confocal Laser Scanning Microscope setup. The tubular lens and the objective focus the laser light into a small, ideally diffraction limited focus volume within the fluorescent probe. Fluorescence photons emitted in the direction of the objective lens get recollected as well as some reflected illumination light. But passing the dichroic mirror (beam splitter) is only possible for the red shifted fluorescence light. Therefore only the emission light is able to reach the photodetector, e.g. photomultiplier tubes (PMT) or avalanche photo diodes (APD) that transform the photons into electric signals. The scan mirror allows to image larger regions by rastering the specimen. Image taken from (Heuvelman, 2008).

2.1.4. Illumination and detection in confocal laser scanning microscopy

In a CLSM the images or simpler the detected signals are generated in a 3-step-process: The excitation of the fluorophore by a point laser source, photon emission of the fluorophores and the detection of the photons by a highly sensitive detector. Each step can be described by partly wavelength-dependent functions that characterize instrument and probes (Wachsmuth, 2001). For illumination in a CLSM, laser light is applied that is focused to a small focal volume. Its overall intensity can be described by the wavelength dependent product of laser power *P* and $\Omega_i(\vec{r})$, an instrument specific function describing the laser beam profile together with imaging properties of the optical system. The function $\Omega_i(\vec{r})$ is wavelength dependent because of chromatic aberrations of the optical system with *i* describing laser lines of different wavelength. Therefore, the intensity is:

$$I_{ill,i} = P_i \cdot \Omega_i(\vec{r}) \tag{2.3}$$

The fluorescence emission characteristics of fluorophores differ over a wide range. Their spectral properties are described in the absorption spectrum, giving the probability $\varepsilon(\lambda)$ to excite the fluorescent dye at a distinct wavelength. The probability $q(\lambda)$ of emitting a photon of a distinct wavelength is according to the emission spectrum. Emission of fluorescence photons happens isotropically in all directions. To describe the probability that a photon emitted at position $\vec{r}$ in the sample reaches the detector *j,* the geometric transfer function $GTF_j(\vec{r})$ is defined. The spectral efficiency of each detector *j* as well as optical properties of emission filters get regarded in the so-called spectral transfer function $STF_j(\lambda_{\text{det}})$ of the detection system. Including all these dependencies, one is able to calculate the photon flux $f_j(\vec{r})$ at the detector *j* that is emanating from a fluorophore sitting at position $\vec{r}$ in the sample, excited by the laser line *i*:

$$f_j(\vec{r}) = P_i \cdot \Omega_i(\vec{r}) \cdot \varepsilon(\lambda_{ill,i}) \cdot GTF_j(\vec{r}) \cdot \int q(\lambda_{\text{det}}) \cdot STF_j(\lambda_{\text{det}}) \cdot d\lambda_{\text{det}} \tag{2.4}$$

The spatial detection probability is given by $\Omega_i(\vec{r})$ and $GTF_j(\vec{r})$:

$$\psi_{ij}(\vec{r}) = \Omega_i(\vec{r}) \cdot GTF_j(\vec{r}) \tag{2.5}$$

Because of diffraction and aberrations, in a lens-system a point-like light source will be smeared out to a three dimensional diffraction pattern which is still close to the diffraction limit. The *NA* of the objective and the wavelength λ of the excitation laser control the size of this diffraction pattern and thus, define the focal volume. All fluorophores within this diffraction pattern are targets for excitation to higher energy levels. Mathematically this spread of intensity and therefore the shape of excitation area can be described by the point spread function of illumination, $PSF_{ill}(\vec{r})$. Also the detection profile has to be considered with a point spread function $PSF_{\det}(\vec{r})$. In a confocal microscopy setup the spatial functions for illumination $\Omega_i(\vec{r})$ and detection $GTF_j(\vec{r})$ are equal to the corresponding point spread functions. Therefore the detection probability is given by the convolution product of illumination PSF and detection PSF:

$$\psi(\vec{r}) = PSF_{ill}(\vec{r}) \cdot PSF_{\det}(\vec{r}) \tag{2.6}$$

That means, only photons emitted within the illumination volume are effectively detected. This result is concordant with the confocal principle, where illumination volume and detection volume are overlaid.

2.1.5. Fluorescence fluctuation microscopy

Using techniques for *in vivo* labeling of cells while illuminating only infinitely small regions with low laser intensities (using highly sensitive detectors like CCD (charged coupled device)-cameras, photomultiplier tubes PMT or avalanche photo diodes APD), CLSM provides a non-invasive method for imaging living cells.

At the same time the CLSM optical setup can be used to follow the dynamics of molecular processes in the living cell in a time resolved image-series, when proteins or nucleic acids of interest are fluorescently labeled. This type of studies allows to observe molecular dynamics and molecular interactions in living cells. To get a fundamental understanding of the complex network of protein-protein and protein-nucleic acid interactions that regulate cellular processes, it is important to identify and quantify the fundamental behavior of individual proteins and their interaction behavior within protein complexes. Measurements of the dynamics of molecular processes require a sufficient temporal resolution. Temporal resolution in the case of CLSM is determined by the speed of the scanning and detection process. As to minimize imaging times usually only one focal plane is observed, the imaged region is chosen as small as possible and scanning speed is increased while preserving a sufficient signal-to-noise ratio.

The most common techniques for the *in vivo* analysis of transport and diffusion as well as interaction and immobilization of biological molecules are fluorescence recovery after photobleaching (FRAP, see Chapter 2.3.) and fluorescence correlation spectroscopy (FCS, see Chapter 2.4.). FRAP as a more global method is limited in its temporal resolution by the image acquisition rate of the microscope, and information about faster movement inside the cell is lost. In contrast, FCS measures particle fluctuations in small volumes and thus reaches a much higher temporal resolution. A combination of both methods displays a comprehensive picture of macromolecular dynamics.

2.2. Theoretical foundations of diffusion processes in the nucleus

In the first instance interacting molecules are widely spread all over the cell. Either they are brought together by directed movement due to cellular transport mechanisms (e.g. motor proteins) or one or both interacting species are free and thus, they seek each other by diffusion. This diffusion process has to be considered in conjunction with the reaction rates when molecule dynamics are studied (Berg and von Hippel, 1985).

2.2.1. Free translational diffusion

The diffusion of particles is based on random motion in infinite space resulting from continuous collisions with solvent particles due to its thermal energy $\left\langle mv^2/2 \right\rangle = k_B T/2$, where k_B denotes the Boltzmann constant, v the velocity , T describes the absolute temperature and $\left\langle ... \right\rangle$ denotes time/ensemble averaging. This so-called Brownian motion leads to an equal distribution of these particles in solution. Considering a random walk of independently moving particles the mean square displacement (*MSD*) as a measure of particle spreading can be calculated to:

$$\left\langle r^2(t) \right\rangle = 2dDt \tag{2.7}$$

with d being the dimensionality and D the so-called diffusion coefficient. The MSD goes linear in time. In general D depends on the absolute temperature T and is indirectly proportional to the friction coefficient of the medium. The friction coefficient of a particle, which can be approximated as a sphere with the hydrodynamic radius R_h (radius of a sphere exhibiting the same friction coefficient as the particle), in a solution with viscosity η follows Stokes law $f = 6\pi\eta R_h$. This results in the Stokes-Einstein-formula:

$$D = \frac{k_B T}{f} = \frac{k_B T}{6\pi\eta R_h} \tag{2.8}$$

a diffusion coefficient indirectly proportional to the viscosity and the hydrodynamic radius, respectively (Cantor and Schimmel, 1980). In the case of free diffusion due to concentration (c)-gradients without additional flux or forces, the net flux $\vec{j}(\vec{r},t)$ is described by Fick's first equation:

$$\vec{j}(\vec{r},t) = -\hat{D}(\vec{r},t)\vec{\nabla}c(\vec{r},t) \tag{2.9}$$

Normally $\hat{D}(\vec{r},t)$ is a 3 x 3 tensor but within an isotropic solution diffusion can be described by a constant diffusion coefficient D. Even though the adjustment of concentration gradients is connected with a flux of mass, no particles are destroyed nor created and the continuity equation holds:

$$\frac{\partial c(\vec{r},t)}{\partial t} = -\vec{\nabla}\vec{j}(\vec{r},t) \tag{2.10}$$

Replacing $\vec{j}(\vec{r},t)$ in the continuity equation with Eq. 2.9 results in Fick's second law:

$$\frac{\partial c(\vec{r},t)}{\partial t} = D\vec{\nabla}^2\vec{c}(\vec{r},t) \tag{2.11}$$

2.2.2. Anomalous diffusion

Within more complex environments containing obstacles like fixed structures or larger particles of lower mobility, we have to consider deviations from simple random walk behavior (the ideal case of Brownian diffusion, respectively). Collisions with obstacles and unspecific binding to these objects result in a diffusion behavior that can be described by the phenomenological concept of anomalous diffusion. In contrast to the mean square displacement of Brownian diffusion which follows a linear time dependency $\left\langle r^2(t)\right\rangle \propto t$, the anomalous diffusion model is based on a *MSD* that follows a t^{α}-law and its diffusion coefficient depends on time:

$$\langle r^2(t) \rangle = 2dD(t)t \propto t^{\alpha} \quad \text{and} \quad D(t) \propto \Gamma t^{\alpha-1} \tag{2.12}$$

α depicts the anomaly parameter that gives a measure of environmentally obstructed movement (Fig. 2.6), i.e. the deviation from free diffusion. Normally α is smaller than one for obstructed, anomalous diffusion and larger than one (superdiffusion) for directed but also confined diffusion, $\alpha = 1$ signifies simple (free) diffusion (Wachsmuth et al., 2003). The value *d* again denotes dimensionality and Γ is called the transport coefficient.

As no conventional diffusion constant can be defined in this case, the MSD is characterized by a time dependent diffusion coefficient *D(t)* or the transport coefficient Γ (Schwille and Haustein, 2002; Wachsmuth and Weisshardt, 2007).

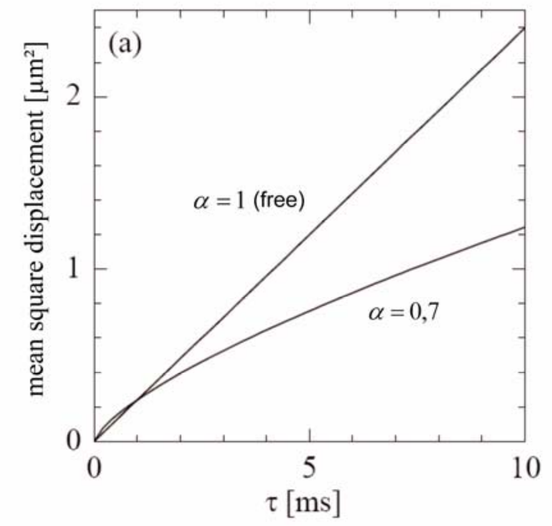

Figure 2.6: Time dependency of mean square displacement (*MSD)* for free and anomalous diffusion. Graph adapted from (Wachsmuth, 2001)

2.2.3. Confined diffusion due to specific binding

In living organisms the above mentioned structures are not simply immobile obstacles but can also provide binding sites for diffusing particles. Sometimes these structures are mobile themselves but on a different timescale and confined to a small area. The simplest way to model this confined diffusion due to binding onto these structures is to regard Brownian motion in a harmonic potential

$$U(\vec{r}) = \frac{1}{2}(\vec{r} - \vec{r}_c)\hat{K}(\vec{r} - \vec{r}_c) \tag{2.13}$$

with its minimum at $\vec{r}_c$. The corresponding equation of motion is:

$$m\frac{d^2\vec{r}(t)}{dt^2} = -\vec{\nabla}U(\vec{r}) - \hat{\Gamma}\frac{d\vec{r}(t)}{dt} - \vec{F}_{stoch}(t) \tag{2.14}$$

including statistical forces $\vec{F}_{stoch}(t)$ that effect stochastic fluctuations about $\vec{r}_c$. Simplifying Eq. 2.14 assuming isotropy (tensors of spring constants $\hat{K}$ and friction coefficients $\hat{\Gamma}$ reduce to constant values k and γ) and supercritical damping, we recognize an additional flux of particles $\vec{j} = c\vec{v} = -c/\gamma\vec{\nabla}U$ (Wachsmuth, 2001). Extension of Fick's second law (Eq. 2.11) with this additional term results in the Smoluchowski-equation:

$$\frac{\partial c(\vec{r},t)}{\partial t} = \frac{k}{\gamma}\vec{\nabla}\left[(\vec{r} - \vec{r}_c)c(\vec{r},t)\right] + D\vec{\nabla}^2 c(\vec{r},t) \tag{2.15}$$

k/γ describing the characteristic relaxation and $t_{relax} = \gamma/k$ the relaxation time, respectively.

2.3. Fluorescence recovery after photobleaching (FRAP)

The technique of fluorescence recovery after photobleaching, FRAP (or FPR, fluorescence photobleaching recovery), was developed in the 1970s by Axelrod and coworkers to study diffusion in membranes of living cells (Axelrod et al., 1976; Edidin et al., 1976). In the last ten to fifteen years FRAP became more and more popular because of two factors: First, the implementation of confocal fluorescence microscopy allowed to extend the research topics where FRAP can be applied, e.g. to the inside of cells and because measurements can be accomplished easily with standard CLSM equipped with the appropriate software (confocal setup for FRAP see Fig. 2.7). Second, the progress in GFP-technology allowed it to label proteins of interest easily and to perform FRAP on transiently or stably transfected cells without further disruption of the cell state (Houtsmuller and Vermeulen, 2001; Lippincott-Schwartz et al., 2001; Rabut and Ellenberg, 2005; Wachsmuth and Weisshardt, 2007).

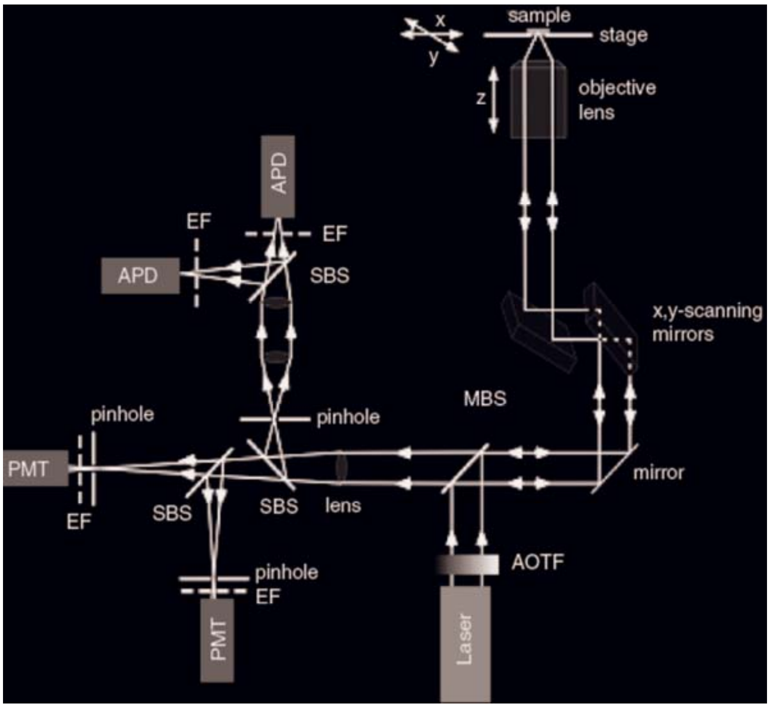

Figure 2.7: Confocal setup for FRAP and FCS. For FRAP the focus volume is scanned by the mirrors, for FCS it is fixed. Acusto optical tunable filters AOTF modulate the laser intensities. Beam splitters and emission filter led the emitted light to the suitable detectors, i.e. PMTs for FRAP and APDs for FCS. Image taken from (Wachsmuth and Weisshardt, 2007)

The underlying principle of FRAP experiments is simply explained: The kinetics of fluorescently tagged molecules can be discovered due to perturbation of the steady-state fluorescence distribution by bleaching the fluorescence in a previously masked region of interest (ROI). For bleaching a high intensity laser pulse at the excitation wavelength is applied. The subsequent spatial redistribution of irreversibly bleached and still fluorescent molecules is recorded at relatively low intensity. Characteristics of the signal-recovery within the ROI are analyzed qualitatively and quantitatively to reveal information on kinetic properties like diffusion constants, mobile or immobile fractions, binding constants etc.

It is important to keep in mind that just the fluorophore is photochemically altered and therefore non-fluorescent, the protein structure or functionality is not affected. Thus, the protein behavior can be observed in its natural environment.

2.3.1. Temporally resolved FRAP (iFRAP)

FRAP measurements are conducted in three steps: A series of images is taken before the bleach (prebleach images) to describe the equilibrium distribution of the fluorescently tagged protein. Then a small circular or rectangular ROI is marked, followed by a bleaching sequence at high laser intensity as fast and as efficient as possible. In order to record the redistribution of fluorescent molecules back to equilibrium, several postbleach images are recorded. These images are then analyzed by averaging the fluorescence intensity within the ROI and plotting these values against time. As analysis is based on intensity variations this method can be named intensity-FRAP (or iFRAP). First, descriptive parameters independent of actual redistribution processes can be gained from the FRAP curve. After correction for the background signal, the loss of fluorescence due to photobleaching of a subcellular region, the acquisition bleaching and normalization to prebleach level, the degree of incomplete bleaching, the fraction of immobile/mobile proteins and a time constant of recovery can be determined (Fig. 2.8).

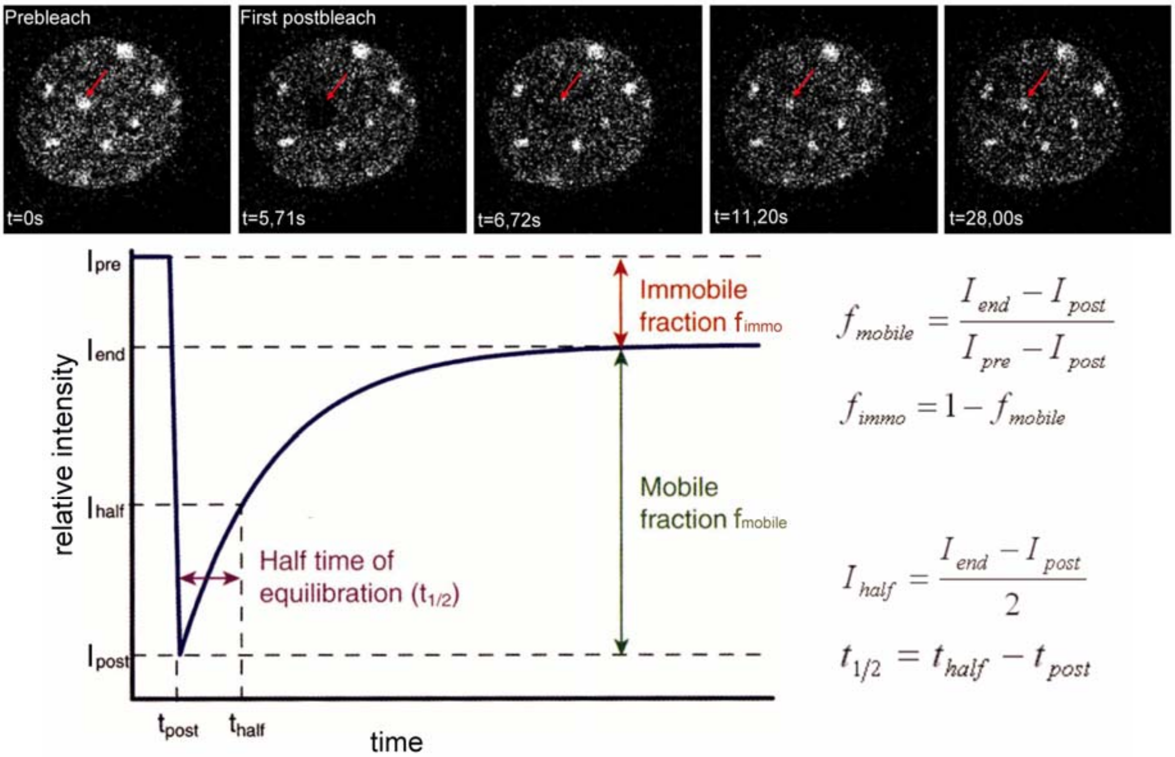

Figure 2.8: Time series of an iFRAP experiment and illustration of descriptive parameters. Graph adapted from (Rabut and Ellenberg, 2005).

For a more quantitative evaluation, mathematical models have to be applied for curve fitting, considering possible underlying processes like diffusion and binding. Comparison of the recovery curves of an inert, non-binding protein (e.g. GFP alone) and that of a binding protein of interest can provide a first impression if binding interactions are involved (Sprague and McNally, 2005). The next step is to evaluate to which degree diffusion or binding processes influence the recovery. Depending on their contributions the interpretation of the iFRAP curve is different. If protein diffusion through the ROI is significantly faster than the protein binding to its target, the main part of recovery is dominated by binding interactions. Brian Sprague and James G. McNally identified this case as 'diffusion-uncoupled' FRAP (schematically shown in Fig. 2.9, left). The mathematical model for the simplest case of 'diffusion-uncoupled', binding dominated FRAP is to assume a single binding state and to fit the data to an exponential recovery (Sprague and McNally, 2005; Wachsmuth and Weisshardt, 2007):

$$1 - \exp(-k_{off}\, t) \tag{2.16}$$

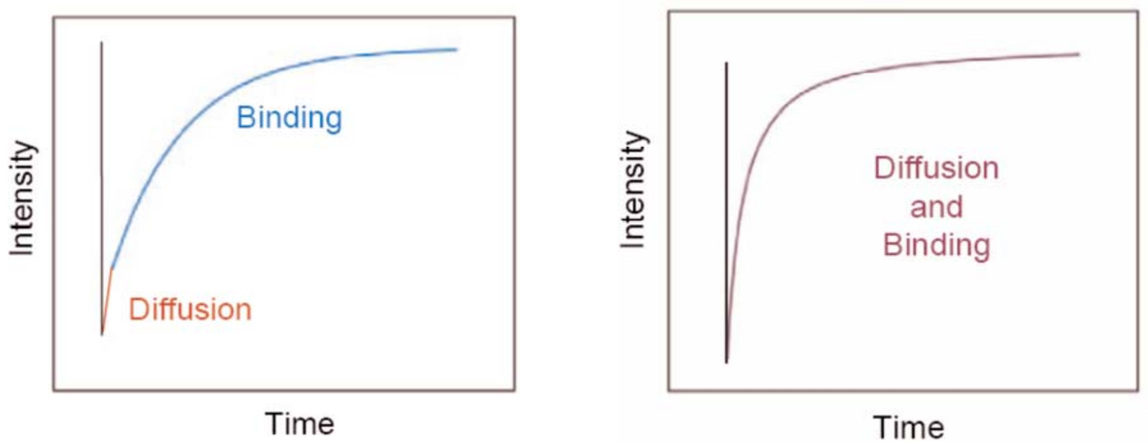

Figure 2.9: Schematic illustration of different iFRAP recovery curves. The diffusion-uncoupled FRAP recovery-curve (left) can be divided into two phases: Diffusion only contributes within the first second(s) followed by binding processes lasting seconds to minutes. When diffusion and binding processes are intermixed the curve of the diffusion-coupled case (right) cannot be separated into two phases. Schemes adapted from (Sprague and McNally, 2005).

Is the diffusion across the bleach-spot slower, or occurs at comparable timescales needed for binding reaction, diffusion cannot be neglected. In 'diffusion-coupled' FRAP experiments both diffusion and binding determine the recovery behavior and the corresponding time scales (Fig. 2.9), therefore the underlying system has to be described by the more complex diffusion-reaction-equations assuming homogeneous distributed binding sites.

A diffusion-dominant case appears when the association time to a binding site is much faster than diffusion across the bleach spot. Then the recovery curve can be fitted only with a solution of the diffusion equation. The solution of the diffusion equation (Fick's second law, Eq. 2.11) in two dimensions with the boundary conditions $x = x_0$ and $y = y_0$ at $t = 0$ (time of first postbleach) is given by the transition probability (Green's function):

$$P_D(x,y,t|x_0,y_0,0) = (4\pi Dt)^{-1}\exp\left[-\frac{(x-x_0)^2}{4Dt}-\frac{(y-y_0)^2}{4Dt}\right] \tag{2.17}$$

For bleaching a rectangular ROI the postbleach distribution as initial condition is given by

$$c(x_0,y_0,0) = 1 + p\left[\Theta(x_0-a)-\Theta(x_0+a)\right]\cdot\left[\Theta(y_0-b)-\Theta(y_0+b)\right] \tag{2.18}$$

with Θ being the unit step function and p corresponds to the bleach depth ($p = 0$ for non-bleached regions and $p = 1$ for a completely bleached ROI). Thus, the concentration distribution inside the ROI with edge length *2a* and *2b* respectively at later times can be calculated from

$$c(x,y,t) = \int_{-a}^{a}\int_{-b}^{b} c(x_0,y_0,0)P_D(x,y,t|x_0,y_0,t)\,dydx =$$

$$= 1-\frac{p}{4}\left[erf\left(\frac{a-x}{\sqrt{4Dt}}\right)+erf\left(\frac{a+x}{\sqrt{4Dt}}\right)\right]\cdot\left[erf\left(\frac{b-y}{\sqrt{4Dt}}\right)+erf\left(\frac{b+y}{\sqrt{4Dt}}\right)\right] \tag{2.19}$$

As only averaged values are plotted versus time in the iFRAP recovery curves, we have to integrate over the region and average this term:

$$\frac{1}{4ab}\int_{-a}^{a}\int_{-b}^{b} c(x,y,t)\,dydx =$$

$$= 1-p\left(\left[\sqrt{\frac{Dt}{\pi a^2}}\left(1-\exp\left(-\frac{a^2}{Dt}\right)\right)-erf\left(\sqrt{\frac{a^2}{Dt}}\right)\right]\cdot\left[\sqrt{\frac{Dt}{\pi b^2}}\left(1-\exp\left(-\frac{b^2}{Dt}\right)\right)-erf\left(\sqrt{\frac{b^2}{Dt}}\right)\right]\right) \tag{2.20}$$

With the assumption that fluorophore concentration is directly proportional to its intensity this equation is fitted to the iFRAP curves (derivation followed Dr. M. Wachsmuth, personal communication and (Görisch et al., 2004)). This solution results in an effective or apparent diffusion constant. In the more complex case, when neither diffusion nor binding can be neglected, the iFRAP recovery curve has to be fitted with both terms, the exponential term for binding events in addition to the diffusion term. Here, a linear superposition of both terms was chosen.

To be able to distinguish, which case is present, distinctions cannot be made on the basis of timescales for recovery because even diffusion-coupled FRAP can last as long or even longer than binding influenced recovery. There are different possibilities to test this more reliably: Since diffusion, but not reaction kinetics depend on spatial scales one possibility to test this is to vary spot sizes. Detectable changes depending on spot size are a sign of diffusion-coupled processes (Sprague and McNally, 2005). A second method is described in the next chapter, using a strip-bleach approach.

2.3.2. Spatio-temporally analyzed strip-bleach FRAP (sFRAP)

The evaluation of FRAP can incorporate also a spatial analysis of the recovery time course, rather than evaluating solely the time-dependent changes in the averaged intensities. On the one hand this can be an analysis of averaged intensities of a few non-bleached areas at different intervals from the bleached ROI. On the other hand - as done here - continuous one-dimensional profiles through bleached and non-bleached areas are evaluated (Wachsmuth and Weisshardt, 2007). To be able to do an evaluation considering only one dimension, the experiment has to be conducted appropriately: A rectangular ROI comprising the whole cell diameter is bleached into the equilibrium distribution of the molecule of interest. By bleaching a strip in x-direction through the whole cell we prevent diffusion in x. In z-direction (along the optical axis) the bleach permeates throughout the whole cellular compartment and thus, no diffusion in this direction is possible. In this case all recovery processes are, in first approximation, just one dimensional. As shown in Fig. 2.10, for the analysis the profiles are averaged, normalized to the prebleach distribution and plotted against distance for each image over time.

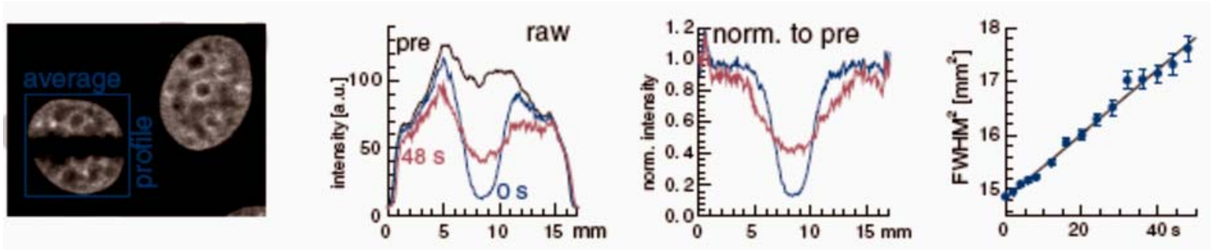

Figure 2.10: Spatial analysis of strip-bleach FRAP. Left image: Postbleach image illustrating the directions of average and profile. Middle: Profile of prebleach (black), the first postbleach (blue) and a later postbleach (pink); raw data and normalized data are shown. Right: Plot of the squared full width of half mean ($FWHM^2$) versus time; the slope is proportional to the diffusion coefficient D. Image taken from (Wachsmuth and Weisshardt, 2007).

In such an experiment one can decide if recovery is more likely due to diffusion processes or whether binding plays a decisive role. In the diffusion dominant case the time course depends on geometry and the initially rectangular bleach smoothens out (compare normalized graph in

Fig. 2.10). However, if mainly binding reactions are responsible for redistribution the rectangular shape does not change during recovery (compare also Fig. 2.11) (Beaudouin et al., 2006).

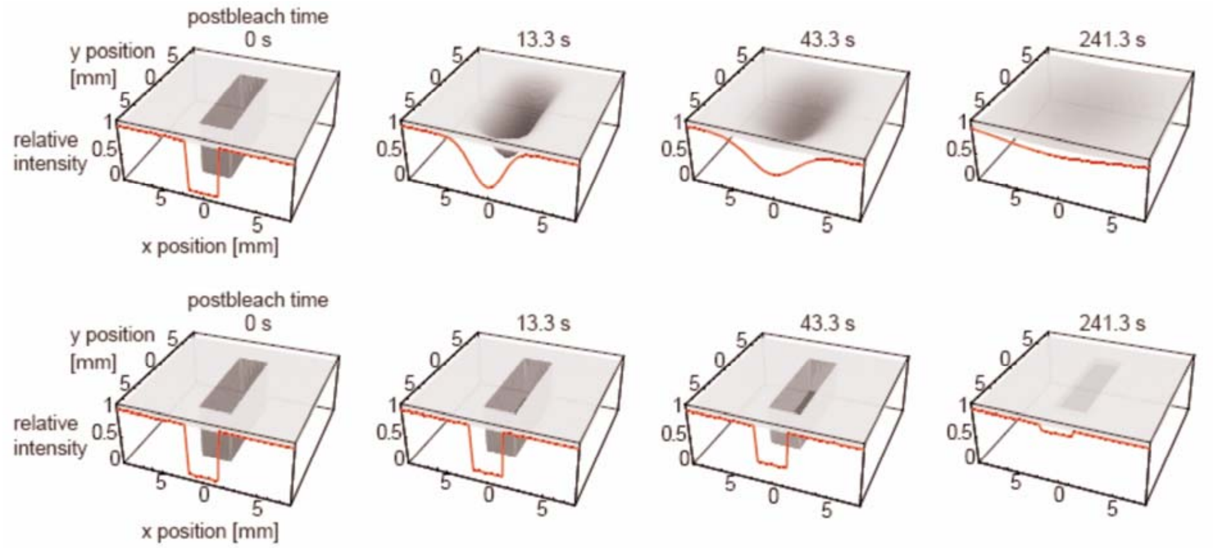

Figure 2.11: Diffusion- (above) or reaction-dominant recovery (below). Image taken from (Wachsmuth et al., 2008b).

The additional benefit of this experiment is to extract the apparent or effective diffusion coefficient. There are two possibilities to do so: First, the effective width has to be determined by fitting a Gaussian function to the profiles. Plotting the squared full width of half mean (*FWHM²*) versus time describes the diffusion process (see Fig. 2.10). Second, the smoothing of the intensity profile can be analyzed. For one-dimensional strip-bleaching the postbleach distribution as initial condition is theoretically given by

$$c(y_0,0) = 1 + p\left[\Theta(y_0 - a) - \Theta(y_0 + a)\right] \tag{2.21}$$

and then the concentration distribution of later times can be calculated analog to Eq. 2.19

$$c(y,t) = 1 - \frac{p}{2}\left[erf\left(\frac{a-y}{\sqrt{4Dt}}\right) + erf\left(\frac{a+y}{\sqrt{4Dt}}\right)\right] \tag{2.22}$$

with a strip width *2a*. Now plotting the squared denominator of the error functions, that is equivalent to the mean square displacement $\left\langle r^2(t)\right\rangle = 4Dt$, versus time the slope is proportional to the apparent diffusion coefficient. This solution assumes a free random walk within an infinite space. Regarding fast diffusive processes and bleaching a reasonably broad strip within a cell conflicts with the second proposal. This confinement can again be compared to an isotropic harmonic potential (compare Chapter 2.2.3.). Applying the correct Greens function the calculation of the fit-function results in a similar function as Eq. 2.22, but this time the mean square displacement is given by $\langle r^2(t)\rangle = r_c^{\,2}(1-\exp(-4Dt/r_c^{\,2}))$, with r_c being the long-term MSD in 2D (Görisch et al., 2004; Wachsmuth et al., 2008a). The particle experiences fast but confined diffusion with a diffusion coefficient D in a corral with radius r_c. The squared denominator has to be plotted versus time and by fitting the MSD-formula the diffusion coefficient of confined diffusion can be extracted.

2.4. Fluorescence correlation spectroscopy (FCS)

Fluorescence correlation spectroscopy (FCS) is a high temporal and spatial resolution method to measure local concentrations, mobility coefficients, and reaction kinetics of fluorescently labeled molecules in minuscule concentrations – suitable for both *in vitro* and *in vivo* measurements. As a “statistical-physics-based tool” FCS measures length and amplitude of local fluctuations of the fluorescence signal about the equilibrium in an open but optically well-defined observation volume (Fig. 2.12) (Maiti et al., 1997). This signal corresponds to the unavoidable noise emerging with small ensembles and is in fact disturbing for various experiments, e.g. FRAP.

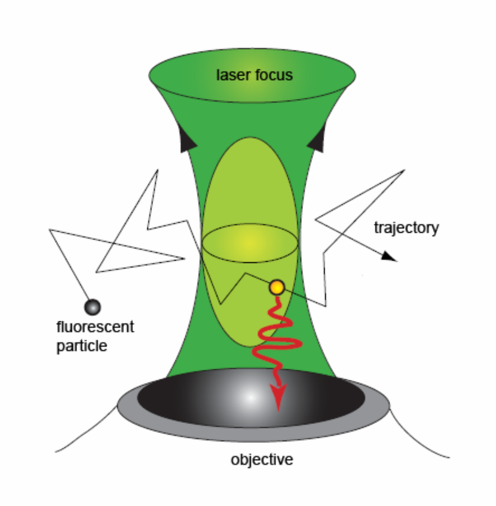

Figure 2.12: Statistical intensity fluctuations are detected from fluorescent molecules that get excited by a strong focused laser beam. Figure by (Weidemann, 2002).

Whereas the fluctuation amplitude depends on the number of molecules and the brightness of fluorophores in the focus, the frequency contains information about molecular dynamics due to Brownian motion, chemical reactions but also photophysical features of the fluorescent proteins (e.g. triplet states). For analysis the recorded intensity signal is subjected to a time correlation analysis (autocorrelation), a measure for self-similarity of the signal. This allows to extract quantitative parameters by fitting a theoretical model to the autocorrelation curve (Fig. 2.13).

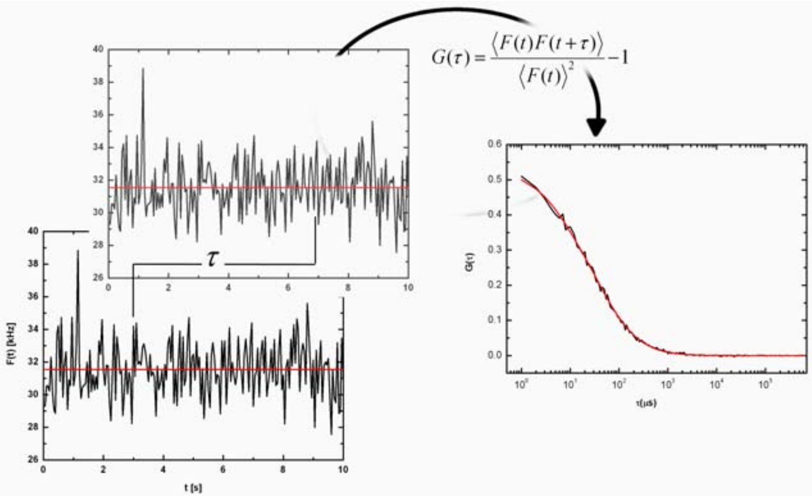

Figure 2.13: Autocorrelation-analysis. The intensity signal (left) fluctuating around the mean value (red line) is measured over time. Multiplication of the signal with itself, shifted for a lag time τ, and normalization results in the autocorrelation curve (right). To extract reasonable parameters the curve is fitted to a mathematical model (red curve).

First FCS experiments were performed in parallel to FRAP (in the 1970s) by D. Madge, E. Elson and W. Webb measuring the diffusion and reaction kinetics of ethidium bromide (EtBr) intercalating with DNA (Elson and Magde, 1974; Magde et al., 1974). The problem inherent to these first pioneering measurements was their poor signal-to-noise ratio due to insufficient detection sensitivity and background suppression, and also because of too large ensemble numbers in a still huge focus volume. A great improvement was achieved when R. Rigler and colleagues were able to incorporate strong focusing of the laser beam and a confocal detection scheme in the FCS-system (Eigen and Rigler, 1994; Rigler et al., 1993). Using an objective with high numerical aperture ($NA > 0.9$) (Schwille, 2001; Schwille and Haustein, 2002) the laser beam is focused down to resolution limit, resulting in a small illuminated volume and thus, fulfilling one important principle of FCS: Relative fluctuations become smaller the more particles contribute to it and therefore it is important to minimize the number of particles in the focal volume to register appropriate fluctuations. A better axial resolution was achieved by using a detection-pinhole in the image plane to block the scattered light. Using such a setup with modern avalanche photodiode photon-detectors, laser technique and high *NA*-objectives (Fig. 2.7) allows to detect hundreds of photons while only one fluorescent molecule traverses the focus volume in less than a millisecond (Maiti et al., 1997). Although the focal volume can be smaller than 1 fl. A concentration ranged between 1 nM and 1 µM is easily detectable. With FCS resolvable time scales range between microseconds and seconds, lower limitations are due to time resolution of the implemented measurement electronics and the upper limit is given by the dwell time of the particles and the stability of the fluorophore towards bleaching. For good statistics, measurements should last 1000-times longer than the slowest process of interest (Haustein and Schwille, 2003; Wachsmuth and Weisshardt, 2007).

In summary, FCS is a non-invasive method that works without significant disturbance of local equilibria, exhibits high detection-sensitivity in a very small volume and profits from the high selectivity of fluorescence signals. In combination with *in vivo* labeling of specific cellular proteins it provides the possibility to observe diffusion and transport processes of distinct molecules directly in living cells, even in individual cellular compartments (Wachsmuth et al., 2000).

2.4.1. Theoretical Concepts of FCS

As mentioned before, fluorescence fluctuations are quantified by temporal autocorrelation of the measured intensity signal and thus provide characteristic time constants of underlying processes. Derivation of theoretical concepts follows (Wachsmuth, 2001) and (Maiti et al., 1997).

Fluctuations in the fluorescence signal *F(t)* are defined as deviations from the mean value:

$$\delta F(t) = F(t) - \langle F(t) \rangle$$

$$\langle F(t) \rangle = \frac{1}{T}\int_0^T F(t)dt \tag{2.23}$$

The normalized autocorrelation function (ACF) $G(\tau)$ is calculated as time average of the product of fluctuations at times t and the fluctuations after a lag time τ normalized by the squared time average of fluorescence signal.

$$G(\tau) = \frac{\langle \delta F(t)\delta F(t+\tau) \rangle}{\langle F(t) \rangle^2} =$$

$$= \frac{\langle F(t)F(t+\tau) \rangle}{\langle F(t) \rangle^2} - 1 \tag{2.24}$$

As a first result from FCS measurements we get the ACFs. However, to extract the interesting parameters like concentration of molecules, diffusion coefficient etc. the data need to be fitted to an appropriate theoretical correlation function. For this, the relevant physical models are introduced in the following.

2.4.2. Free diffusion in FCS

Free Brownian motion of fluorescent particles in solution causes local concentration fluctuations and it can be supposed that this local intensity fluctuations obey Fick's second law (Eq. 2.11). Another assumption is made when we consider the illumination and detection profile to follow a three-dimensional Gaussian distribution. When using a confocal setup with a high numerical aperture this assumption can be fulfilled with high accuracy (Rigler et al., 1993). By solving all equations with appropriate initial and boundary conditions we get the analytical autocorrelation function:

$$G_{diff}(\tau) = \frac{1}{cV_{eff}}\left(1+\frac{\tau}{\tau_{diff}}\right)^{-1}\left(1+\frac{\tau}{\kappa^2\,\tau_{diff}}\right)^{-1/2} \tag{2.25}$$

with the lateral diffusion time or mean dwell time $\tau_{diff} = \omega_0^2/4D$, the average number of particles in the focus $N = cV_{eff}$ as well as the effective focal volume $V_{eff} = \pi^{3/2}\,\kappa\,\omega_0^3$. $\kappa = z_0/\omega_0$ is the so called structure parameter and characterizes the geometry of the focal volume, as illustrated in Fig. 2.14.

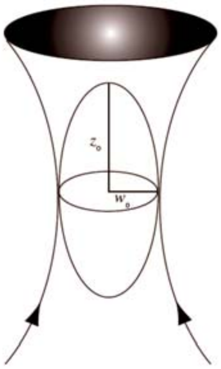

Figure 2.14: The focus volume of high NA objectives is described by Gaussian function. ω_0 and z_0 are the transversal and axial $1/e^2$ radii. Image adapted from (Weidemann, 2002).

Fig. 2.15 shows typical ACFs for different diffusion times and different structure parameters.

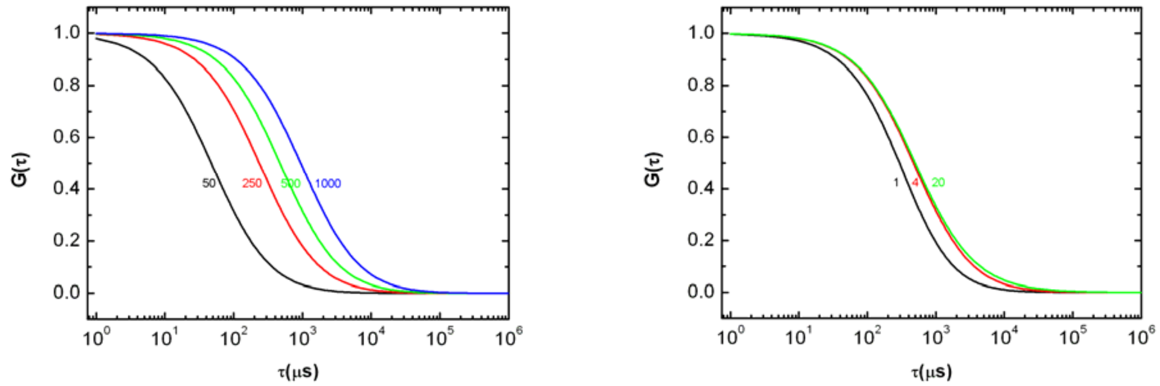

Figure 2.15: Autocorrelation functions – how τ_{diff} (left) and κ (right) exerts influence on ACFs. Graphs were calculated using a single diffusive species containing just one molecule within the focal volume ($N = 1$); to show how ACF depends on τ_{diff} the value for κ was fixed to 4 and τ_{diff} given as 50, 250, 500 and 100 µs respectively. Variation of κ between 1, 4, and 20 shows only little dependency on κ, here, the value for τ_{diff} was fixed to 500 µs.

This model is about the simplest case for an analytical ACF (Tewes, 1998); it is useful to determine local concentrations c and the diffusion coefficient of monodisperse particles, when the parameters ω_0, z_0 and V_{eff} are known. Theoretically these values are known from well-established beam geometry. However, in practice these values are not achievable because of aberrations of the system. More precise results can be obtained from calibration measurements with a solution of particles with known concentration and diffusion coefficient. Theoretical calculations result in structure parameters $\kappa = z_0/\omega_0$ of 2 – 3, but values for κ obtained from calibration measurements between 3 and 8 are more realistic (Kim et al., 2007; Wachsmuth and Weisshardt, 2007). For further evaluation, values should be fixed at the calibration results, even though in these regions a variation of $G_{diff}(\tau)$ with κ is really small (Fig. 2.15).

2.4.4. FCS analysis of multiple diffusive species

So far we postulated to examine only inert molecules which do not interact with each other or cellular structures, but this assumption is only valid in exceptional cases. Normally we should assume more than one distinct species. Considering a system of non reacting or very slowly reacting species, FCS seems to be a snap-shot of the system and products as well as educts can be seen again as non-reacting species (Wachsmuth, 2001). Both contribute to the fluorescence fluctuation signal, each with different diffusion times (Fig. 2.16), provided that their τ_{diff} differ more than 1.7 to 2-fold (Wachsmuth and Weisshardt, 2007):

$$F(t) = \sum_s F_s(t) \tag{2.26}$$

The resulting ACF for all species is a sum of all normalized ACFs of each single species s weighted with $\rho_s = c_s/c$, the relative concentrations, and the relative quantum yield of each species η_s:

$$G_{diff}(\tau) = \frac{1}{cV_{eff}} \sum_s \frac{\rho_s \eta_s^{\,2}}{\left(\sum_s \rho_s \eta_s\right)^2} \left[c_s V_{eff} G_{diff,s}(\tau)\right] \tag{2.27}$$

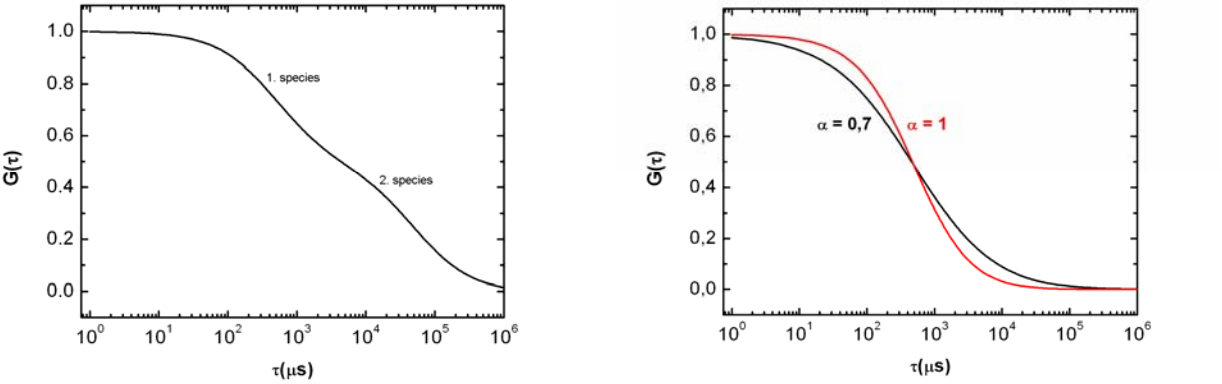

Figure 2.16: ACF for two freely diffusing species (left) and comparison of ACFs for free and anomalous diffusion (right). Left: Both species contribute each 50 % to the ACF, the second diffusion time is chosen 100-fold longer than that of the first species. Right: The ACFs for free (red curve) and anomalous diffusion respectively were calculated with Eqs. 2.25 and 2.28 using $N = 1$, $\tau_{diff} = 500$ μs and $\kappa = 4$.

2.4.5. Anomalous diffusion

Since FCS is a suitable method also for *in vivo* measurements, we have to consider a non-Brownian (anomalous) diffusion model for curve fitting. In cells with its compartments limited by membranes, containing polymers, e.g. filaments or chromatin, and large (diffusive) molecule-complexes, the movement of smaller diffusing molecules gets obstructed in space and by nonspecific interaction. The hindrance by this mobile or immobile obstacles can be regarded in an anomalous diffusion model. Anomalous diffusion is characterized due to a nonlinear time dependency of the *MSD* as described above in Eq. 2.12. To create the ACF of anomalous diffusion the expression τ/τ_{diff} in Eq. 2.25 is replaced by $(\tau/\tau_{diff})^{\alpha}$:

$$G_{diff,s}(\tau) = \frac{1}{cV_{eff}} \left(1 + \left(\frac{\tau}{\tau_{diff}}\right)^{\alpha}\right)^{-1} \left(1 + \frac{1}{\kappa^2}\left(\frac{\tau}{\tau_{diff}}\right)^{\alpha}\right)^{-1/2} \tag{2.28}$$

As can be seen in Fig. 2.16, the curves following anomalous diffusion ($\alpha < 1$) show a characteristic shape decaying more gradually than the curve of Brownian diffusion. Even the inert GFP protein shows a position dependent diffusion behavior in cells: In the cytoplasm its diffusion characteristics can be described by free diffusion with a smaller diffusion coefficient than in buffer solutions because of the higher viscosity in the cytoplasm. But diffusion behavior of GFP becomes anomalous in the nucleus. This could be regarded as endorsement of the assumption that cellular organelles and structures affect particle diffusion, even more in the nucleus than in the cytoplasm (Wachsmuth et al., 2000).

2.4.6. Confined diffusion due to specific binding

In living cells, most molecules bind to higher (immobilized) structures, at least transiently in order to perform their enzymatic or structural functions. But these, in a first approximation immobile structures, e.g. polymer networks as for example chromatin itself, can be mobile in a confined diffusion manner and fluorophores associated to these networks via a protein are also subject to this slow movement. Within FCS experiments this slow movement gets recorded as a fluorescence fluctuation signal as well. Analogous to the derivation of the free diffusion-ACF we can deduce the ACF for this binding case using the Smoluchowski-equation (Eq. 2.15) instead of Fick's second law. We get:

$$G_{bound}(\tau) = \frac{1}{cV_{eff}} \left[\left(1 + \frac{1-\exp\left(-\frac{k\tau}{\gamma}\right)}{\eta}\right)^{-1} \left(1 + \frac{1-\exp\left(-\frac{k\tau}{\gamma}\right)}{\kappa^2\eta}\right)^{-\frac{1}{2}} - \left(1+\frac{1}{\eta}\right)^{-1}\left(1+\frac{1}{\kappa^2\eta}\right)^{-\frac{1}{2}} \right] \tag{2.29}$$

where η means the ratio of τ_{diff}, the dwell time of free diffusion, to the relaxation time $\tau_{relax} = \gamma/k$ and is a measure for the magnitude of the potential:

$$\eta = \frac{\tau_{diff}}{\tau_{relax}} = \frac{\omega_0^{\ 2}}{4D}\frac{k}{\gamma} \tag{2.30}$$

Comparison with anomalous diffusion leads to an anomaly parameter $\alpha > 1$, because directed movement dominates the statistical movement (Wachsmuth, 2001). Obviously the anomalous parameter allows to distinguish between free diffusion ($\alpha = 1$), confined or anomalous diffusion ($\alpha < 1$) and directed movement confined due to binding ($\alpha > 1$).

3. Materials & Methods

3.1. Molecular biology

Molecular cloning

Molecular cloning refers to the introduction of a DNA-fragment in a specialized vector that allows obtaining multiple copies of this DNA and also to add special characteristics to the DNA (Muelhardt, 2003), e.g. tagging with a fluorescence gene.

First, some basic methods used to check each step of the cloning process or to perform preliminary calculations are presented; and second, a short report would be given about how cloning procedure was performed for this thesis.

For transient transfection of cell culture cells the following expression vector constructs were created and used (Table 3.1):

Expression vector	cDNA insert	Vector	Resistance**	Source
p-EGFP-mHP1β	mouse HP1β	pEGFP-C1* (Clonetech, Heidelberg, Germany)	Kan/Neo	This thesis
p-TagRFP-mHP1β	mouse HP1β	pTagRFP-C (Evrogen, Moscow, Russia)	Kan/Neo	This thesis
p-EGFP-hSuv39h1	human Suv39h1	pEGFP-C1* (Clonetech, Heidelberg, Germany)	Kan/Neo	This thesis
p-hLSD-EGFP	human LSD1	pEGFP-N1 (Clonetech, Heidelberg, Germany)	Kan/Neo	Dr. M. Caudron-Herger, DKFZ Heidelberg
pI-mLSD1-GFP	mouse LSD1 (Δ 50 amino acids, N-terminal)	---	Amp	Dr. M. Yonezawa, IMP Austria

Table 3.1: Plasmids used in this work.

* Originally pECFP-C1 but ECFP was replaced by EGFP

** The resistance describes the antibiotics that can be used for selection in the amplification process (Kan: Kanamycin, Neo: Neomycin, Amp: Ampicilin).

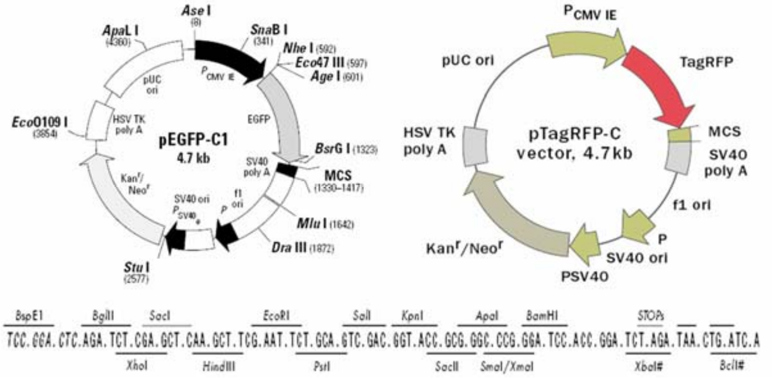

Figure 3.1: Expression vectors used in this work for marking HP1 and Suv39h1 with fluorophores. The multiple cloning site (MCS) was taken from pEGFP-C1, but is similar for both plasmids. Vector cards were taken from www.clontech.com and www.evrogen.com

Agarose gel electrophoresis

Agarose gel electrophoresis is a simple but efficient method to separate DNA fragments of different sizes, which carry negative charge, by applying an electric field. Because of the sieving structure of the agarose gel the velocity of the fragments is inversely proportional to their length. The required agarose concentration depends on the fragment sizes that are expected (compare (Muelhardt, 2003)).

Here, 1 % agarose gels (w/v) were used to observe fragments in the range of 0.5 to 2 kb. The appropriate amount of agarose (SeaKem Le, Chambrex Bioscience Rockland Inc., Rockland, Maine, USA) was melted by boiling in 1x TAE-buffer (Tris-acetate-EDTA buffer) and this solution was poured into a gel tray. After hardening, the gel was transferred to an electrophoresis chamber and was covered with TAE-buffer. DNA samples were mixed with DNA loading buffer and loaded along with a DNA size marker. Electrophoresis was run at 100 V for about one hour. To visualize the bands, DNA was stained either by soaking the gel in an ethidium bromide bath for 5 – 10 min after the run or by including the DNA intercalating dye SybrSafe (Invitrogen, Karlsruhe, Germany) directly into the agarose gel. Images were recorded using the Bio-Rad Gel Doc documentation system (Bio-Rad Laboratories GmbH, Munich, Germany).

Determination of DNA concentration

Using a spectrophotometer (Jasco GmbH, Gross-Umstadt, Germany), the DNA concentration was determined from absorption measurements. Nucleic acids absorb at a wavelength of λ = 260 nm and the absorbance unit of optical density OD_{260} = 1 corresponds to a DNA concentration of 50 µg/µl for double stranded (ds)DNA. By calculating the ratio of OD_{260}/OD_{280} contaminations with proteins can be detected, a protein-free solution showing a ratio between 1.8 and 2.

Polymerase chain reaction (PCR)

The cDNA of HP1β was inserted in an expression vector without fluorescence marker, namely pET-16b (Novagen; HP1 construct originally from Dr. N. Murzina, University of Cambridge, UK), that one of Suv39h1 was inserted in the plasmid pGEX2T-Suv39h1 obtained from Dr. K. Yamamoto (Kyushu University, Japan, (Yamamoto and Sonoda, 2003)). From these vectors the cDNA was amplified by PCR and the required restriction sites were included via the DNA primers. For HP1 a HindIII-restriction site was added at the N-terminus and for Suv39h1 a single amino acid was mutated to avoid a stop-codon.

The PCR reaction was conducted with a proofreading Pwo-polymerase (peqLab Biotechnologie GmbH, Erlangen, Germany and Genaxxon Bioscience GmbH, Biberach, Germany) according to the manufacturers protocol. PCR-mix was prepared on ice containing 25 ng of template DNA, 600 pmol total of each primer, 200 µM dNTPs (deoxy-nucleoside triphosphates), 1x Pwo-buffer and 2.5 units (u) Pwo-polymerase. Reaction volume was filled up to 50 µl with sterile water. The program (Table 3.2) was cycled about 30 times.

Phase	Temperature	Duration	Result
Initial denaturation	94 °C	4 min	Disjunction of DNA double strand
Denaturation	94 °C	1 min	Repetitive disjunction of DNA strands
Annealing	55 °C*	1 min	Attachment of primers to the single-strands
Extension	72 °C	1.5 min**	Completion of single- to double-stranded DNA
Final extension	72 °C	10 min	Completion to total length

Table 3.2: PCR cycling program.

* The annealing temperature depends on the melting temperature of the primer, here, an agreement for HP1 and Suv39h1 primer was found and worked very well.

** The extension time was estimated depending on the expected fragment length (1min per 1kb).

The length of PCR products was checked on analytical agarose gels. Before digestion and ligation the PCR products were separated from primers, vector fragments and redundant nucleotides by gel purification.

Gel purification

DNA fragments were extracted from agarose gels after gel electrophoresis. The band of interest was cut out with a sharp scalpel (handling time was kept short because UV-light can cause mutations within DNA strands). DNA was separated from the gel with QIAquick Gel Extraction Kit (QIAGEN GmbH, Hilden, Germany) following the manufacturers protocol.

Restriction digestion

Restriction enzymes (endonucleases) are bacterial enzymes that cut at specific DNA sequences. They recognize their targeting sequence composed of 4 to 8 bases with high accuracy, and within correct buffer conditions they cut only at these particular sites. Important for ligation, most enzymes create fragments with 5’-phosphate and 3’-OH ends, either ‘blunt’ ends or ‘sticky’ ends, i.e. with single stranded DNA overhangs. For cloning ‘sticky’ ends with different overhang-length are more advantageous because they prevent re-ligation and facilitate correct orientation of inserts.

For preparation of DNA fragments for further processing, e.g. ligation, up to 20 µg DNA was digested with an appropriate amount of enzymes (3 µl each). The buffer system was chosen, depending on the enzymes requirements, as recommended by the manufacturer; in this work double restriction digestion could be performed in the same buffer system. The total reaction volume was determined so that the amount of restriction enzyme did not exceed 10 % of the reaction volume to limit the fraction of glycerin. Incubation was usually 2 hours up to overnight. The following preparative digestions were carried out (Table 3.3).

Product		Restriction enzyme*	Buffer system*
HP1β	PCR-product	HindIII & BamHI	2x Tango
Suv391h	PCR-product	XhoI & EcoRI	2x Tango
pEGFP-C1	Empty vector	HindIII & BamHI	2x Tango
pTagRFP-C1	Empty vector	HindIII & BamHI	2x Tango
pEGFP-C1	Empty vector	XhoI & EcoRI	2x Tango

Table 3.3: Preparative digestions.
*All enzymes and buffers from Fermentas GmbH, St. Leon-Rot, Germany; concentration 10 u/µl

An analytical restriction digestion was used to test for correct length and orientation of the inserted DNA fragment. This time, the total reaction volume was limited to a maximum of 20 µl containing 0.5 – 1 µg DNA and 1 µl (according to 10 u) restriction enzyme each. Incubation was usually 1 hour at 37 °C. DNA fragments were subsequently analyzed by agarose gel electrophoresis.

PCR-Purification

After the digestion of PCR-products residual restriction enzymes and side products were removed in a PCR purification procedure using a PCR purification kit (QIAquick PCR Purification Kit, QIAGEN). Purified fragments were finally dissolved in 30 µl 10 mM of Tris-HCl (tris(hydroxymethyl)-aminomethan hydrochloride), pH = 7.5.

Removal of 5’-phosphate residues from vector fragments

After restriction enzyme digestion, the linearized vectors still carry reactive phosphate groups at the 5’-ends that are required for sugar-phosphate bonds of the DNA. Therefore vectors tend to re-ligate. In order to prevent self-ligation, the phosphate residues were removed by the phosphatase CIP (calf intestine phosphatase). Per 1 µg vector DNA 0.5 units CIP were added directly to the digested vector for 1 hour at 37 °C. Inactivation of CIP-enzyme at 65 °C for 10 min is absolutely essential, otherwise it would also dephosphorylate the insert and the ligation would be impossible. The fragment that should be inserted keeps its phosphate groups and thus is still able to ligate with the vector DNA. After this dephosphorylation process, the linearized vector is purified by gel purification as described before and finally dissolved in 30 µl 10 mM Tris-HCl, pH = 7.5.

Ligation

The insert was digested with the same restriction enzymes used to excise the vector. Thus, compatible ends were present. The ligation mix was prepared on ice to a volume of 20 µl containing 1 µl T4 DNA ligase (according to 5 units; Fermentas GmbH, St. Leon-Rot, Germany) and the appropriate ligase-buffer. The insert and vector-DNA were added in a molecular ratio insert : vector = 5 : 1. Ligation mix was incubated 1 hour at 25 °C and inactivation of ligase was done at 65 °C for 10 min.

Transformation of competent bacteria

To amplify plasmid DNA a strain of the bacterium *E. coli* was used. The uptake of plasmid DNA (‘transformation’) in competent bacteria was done by a heat shock method to make the cell membrane permeable for the plasmids. Competent *E. coli* DH5α cells (20 µl; Invitrogen GmbH, Karlsruhe, Germany) were thawed on ice and mixed carefully with the whole ligation mix. After incubation on ice for 30 min bacteria were heat shocked for plasmid uptake at 43 °C for 30 s and immediately cooled on ice for 5 – 10 min. Adding 350 µl growth medium, cells were incubated 1 hour at 37 °C with shaking (1100 rpm). Afterwards the cells were spun down (2 min, 7000 rpm) and part of the medium was removed. The bacteria pellet was resuspended in the medium. According to the antibiotic resistance of the transformed plasmid the bacteria suspension was plated onto LB (lysogeny broth)-agar plates containing the selection antibiotic. Thus, only bacteria containing the plasmid are able to synthesize enzymes that inactivate the antibiotic and only these bacteria will grow. Incubation over night at 37 °C resulted in small bacteria colonies.

For amplification of an already purified plasmid 0.5 – 1 µg DNA were added to the competent cells and treated as described for ligated DNA.

Colony PCR

A pre-selection of grown colonies regarding insert size and insert incorporation can be achieved by colony PCR. The same primers as for ‘amplification’ PCR were used. The same amount of primer, dNTPs and Pwo-polymerase and Pwo-buffer as described above were mixed in a final volume of 50 µl. Using an autoclaved toothpick, a minimal fraction of bacteria from one colony was added to the PCR mix. The residual colony was plated again on LB-agar at a labeled region of the plate. This procedure was followed for multiple colonies and PCR products were analyzed on agarose gels.

Isolation of plasmid DNA (Miniprep)

Only these bacteria containing the correct plasmid DNA were picked from the plate and 6 ml LB-medium supplemented with the appropriate selection antibiotics was inoculated. Bacterial growth was supported in a shaking incubator (120 – 190 rpm) at 37 °C over night. With utilization of NucleoSpin Plasmid Kit (Macherei-Nagel GmbH & Co KG, Düren, Germany) the plasmid DNA was isolated following the manufacturers protocol. The highly pure DNA was eluted in 30 µl 10 mM Tris-HCl, pH = 7.5. A last check of correctness was done by analytical restriction digestion in combination with gel electrophoresis. Finally all cloned expression plasmids were sent to a sequence laboratory (Seqlab GmbH, Göttingen, Germany) to check correctness of the DNA sequence.

RNase for microinjection

For microinjection a mix was prepared containing RNase in different concentrations (given as units per 10 µl mix), propidium iodide (PI) as injection marker filled up to 10 µl with sodium phosphate (NaP)-buffer and sterile H_2O. All components, except RNase, were boiled 5 min at 95 °C in order to destroy proteases and germs. For each sample also a control solution was prepared containing all buffers and markers except the RNases (the same amount RNase-storage buffer was added instead) to be sure that results are not influenced by other components of the mix. Different types of RNase, listed in Table 3.4, were studied.

RNase	Substrate	Activity of 1u at 37°C
A*	ssRNA	Cleaves 40 µg/min
III**	RNA-DNA hybride	0,5 µg in 20 min
H**	ribosomal RNA	0,5 µg in 30 min
Orn***	oligonucleotides	n.d.

Table 3.4: RNases for microinjection.
* Distributor: Roche Diagnostics, Indianapolis, USA
** Epicentre Biotechnologies, Madison, WI, USA
*** The oligoribonuclease ORN was kindly provided from Dr. Undine Mechold, Institute Pasteur, Paris, France

3.2. Cell biology

The cells used for this work were embryonic Swiss mouse fibroblasts (NIH-3T3 cells). Because of their euchromatin and heterochromatin distribution (see Figs. 4.1 and 4.2 in Chapter 4.1.) they are ideally suited for questions dealing with characteristics of and differences between the two regions and chromatin organization levels. In order to study the dynamics of proteins that affect organization levels, either NIH-3T3 cells were transiently transfected with these proteins or 3T3 cells stably expressing one of these proteins were used:

- NIH-3T3 transfected with expression vectors summarized in Table 3.1
- 3T3 stably expressing EGFP-HP1α (kindly provided by Dr. B. Fodor, IMP, Vienna, Austria)
- 3T3 stably expressing EGFP-Suv39h1 (cells from Dr. M. Yonezawa, IMP, Vienna, Austria)

Cell culture

The 3T3 cells were grown in tissue culture flasks (T75) at 37 °C in a water saturated 5 % CO_2 atmosphere, using Dulbecco modified eagle medium (DMEM) (Gibco, Invitrogen, Karlsruhe, Germany) supplemented with 10 % fetal calf serum (fcs; PAA Laboratories GmbH, Pasching, Germany), 2 mM L-glutamine (PAA Laboratories GmbH), the antibiotics penicillin and streptomycin (100 µg/ml, PAA Laboratories GmbH) and 0.35 g/ml glucose (Merck, Darmstadt, Germany). Medium was renewed every second day.

The 3T3 cell line stably expressing the EGFP tagged protein Suv39h1 features a doxycycline dependent ‘Tet-off’ system to inhibit the additional expression of exogenous protein. Therefore 400 ng doxycycline (Sigma-Aldrich, Steinheim, Germany) per µl was added to the culture medium whenever the medium was renewed. At a minimum of 24 hours before fixation or *in vivo* imaging (see below) doxycycline was removed and thus, the expression of green fluorescently labeled protein was activated.

Cells were split every 3rd or 4th day to keep them in a logarithmic growth phase. For detaching the adherent growing cells from the flask surface they were washed with 1x PBS (phosphate-buffered saline) and incubated in trypsin (PAA Laboratories GmbH) diluted with PBS for a maximum of 5 min at 37 °C. The enzyme was inactivated by the addition of fresh medium. The cells were pelleted by centrifugation (5 min, 1200 rpm) and resuspended in fresh medium.

Cells were stored at –150 °C. For freezing, the cells they were treated with trypsin and centrifuged as described above, but the cell pellet was resuspended in ice cooled freezing solution consisting of 80 % DMEM, 10 % fcs and 10 % dimethyl sulfoxide (DMSO). Typically 1 ml of this cell suspension was transferred to each 1.8 ml cryo-tube and directly frozen to –80 °C (altogether 3 tubes from one T75 flask). After one week the frozen cells were transferred to a –150 °C freezer for storage.

Transient transfection

Transfection stands for the introduction of foreign DNA into eukaryotic cells. Cells were transfected with Effectene Transfection Reagent from QIAGEN, Hilden.

For subsequent fixation, cells were seeded out on purified and autoclaved cover slips within 12-well-plates one day before transfection in order to get them 60 – 80 % confluent. Transfection protocol was applied according to the suppliers protocol using between 0.5 – 0.8 µg plasmid DNA.

Microinjection of cells

For microinjection a bright field microscope with AIS 2 control system, which integrates a FemtoJet (Eppendorf AG, Hamburg, Germany) pressure system, was used. Injection pressure varied from 100 – 400 hPa depending on the cells and the needle, compensation pressure was kept constant at 75 hPa and injection time was chosen to 0.5 s. With these settings the injected volume was estimated to be 10 – 20 % of the cell volume, i.e. in the range of 50 – 100 fl of the RNase mix.

Injection needles were prepared before each injection session using a micropipette puller (P-97 Flaming Brown). Borosilicate glass capillaries with a diameter of 0.94 – 1.2 mm (Harvard Apparatus, Holliston, Massachusetts, USA) were used as blanks and thus, needles with a tip-aperture of about 3 µm in diameter were produced.

The day before injection cells were seeded out on cover slips to give them the possibility to adhere properly. The solutes for injection were prepared as described above and were kept on ice until usage. In order to avoid blocking the needles with debris, the mixes were centrifuged for 10 min with 13000 rmp at 4 °C. Up to 300 cells were injected either in cytoplasm or directly in the nucleus. Instantaneously after microinjection procedure cells were returned into the incubator at normal growth conditions to let them recreate – or the RNase to react – for a minimum of 30 min before they undergo fixation (see below).

Cell preparation for *in vivo* imaging

For *in vivo* imaging cells were grown and eventually transiently transfected in chambered cover glasses, so called Lab-Tek chambers (1.0 Borosilicate cover glass, Nunc, Wiesbaden, Germany). The DMEM growth medium was replaced with Leibovitz's L15-medium (Gibco, Invitrogen, Karlsruhe, Germany) supplemented with 10 % fcs and penicillin as well as streptomycin. L15-medium is able to support cell growth in not CO_2-equilibrated environments and keeps the pH stable during imaging.

Fixation of the cells

Normally, transfected or injected cells were mounted on microscope slides after paraformaldehyde (PFA) fixation. Therefore cells were washed twice with PBS and then fixed with 4 % PFA in PBS for at least 7 min at room temperature. After removal of PFA, the cells were washed again using PBS and chromatin counterstaining was done with DAPI for about 5 min. To remove the excess of DAPI, cells were again washed with PBS and sterile water. Afterwards they were mounted on the slides with mowiol (Carl Roth GmbH, Karlsruhe, Germany). For drying and hardening samples were stored one night at room temperature at a dark place. Slides were stored at 4 °C.

3.3. Fluorescence confocal laser scanning microscopy

For taking high resolution images of protein localization sites a Leica TCS SP5 microscope (Leica Microsystems CMS GmbH, Mannheim, Germany; Fig. 3.2) was used.

Figure 3.2: Confocal laser scanning microscope Leica TCS SP5. Image adapted from Leica TCS SP5 brochure – technical data, Leica Microsystems CMS GmbH, Mannheim (www.leica-microsystems.com).

For imaging DAPI staining, the diode laser (nominal power 50 mW) and for the other fluorophores the argon laser (100 mW) was used. The used fluorophores were excited by the appropriate laser in combination with the filter of desired wavelength (Table 3.5).

Fluorophore	Laser	Excitation wavelength	Detection range
DAPI	diode laser	405 nm	410 – 465 nm
GFP	argon laser	488 nm	495 – 530 nm
TagRFP	argon laser	514 nm	535 – 650 nm
PI	argon laser	514 nm	569 – 685 nm

Table 3.5: Excitation wavelength and detection ranges of used fluorophores.

Laser intensity was kept as low as possible in order to avoid acquisition photobleaching. Fluorescence signal was detected by PMTs within detection ranges given in Table 3.5. For imaging, normally values about 800 – 1000 V PMT-voltage were chosen.

For all measurements a HCX PL APO lambda blue 63x, oil immersion objective with *NA* of 1.4 was used. The pinhole was kept at 1 Airy. Images were taken 512 x 512 pixels with a scanning speed of 400 Hz. The resulting voxel size depending on the magnification (3 – 5-

fold) ranged from 51 – 150 nm. To increase the signal-to-noise ratio an 8-fold line average was used for the fixed samples.

If more than one fluorophore was incorporated into the cell, a sequential scan mode was applied. The detection ranges were adjusted to avoid overlap (see Table 3.5), and DAPI images were taken at the end in order not to bleach other fluorochromes. Confocal images were analyzed and processed using Image J (1.38 r, National Institute of Health, USA) and Adobe Photoshop CS (8.0, Adobe Systems, USA).

3.4. Fluorescence recovery after photobleaching

FRAP instrumentation

Fluorescence recovery after photobleaching experiments were also carried out with a Leica TCS SP5. For photobleaching experiments the LAS AF Leica application suite, Advanced fluorescence software (Leica Microsystems CMS, Mannheim, Germany) was used.

To image and to bleach GFP the argon-ion laser (rating max. 100 mW) was chosen. Rapid switching between low-intensity illumination for pre- and postbleach images and high-intensity illumination mode for bleaching was accomplished with an acusto-optical tunable filters (AOTFs), which allows transmission to be varied over a wide range within microseconds (Rabut and Ellenberg, 2005).

The selection of the objectives for photobleaching experiments depends strongly on the *NA*. High *NA* means that the laser beam is focused best along the optical axis but out-of-focus regions are not bleached efficiently, low *NA* objectives bleach the sample more uniformly along optical axis and therefore the transport processes are effectively limited to two dimensions, but a drawback of low *NA* objectives is that the bleach is less efficiently and resolution is worse.

Cells

Measurements were carried out at room temperature within a maximum of 2 – 3 hours. Although diffusion is a temperature dependent process, an effective difference of ~15 °C between cell culture temperature and room temperature results in a decrease of diffusion rate that is too small to be resolved in a FRAP measurement (Carrero et al., 2003). With these precautions one should be able to exclude measuring artifacts traced back to this temporary conditions of growth.

Establishing photobleaching conditions

Photobleaching conditions were established using fixed GFP-stained samples. To avoid disturbance due to scattered light a high *NA* objective, namely the 63x oil immersion objective with *NA* = 1.4 was chosen for further experiments. Bleaching through the cell along the optical axis was complete (Fig. 3.3), so that for the analysis a 2 dimensional transport can be assumed.

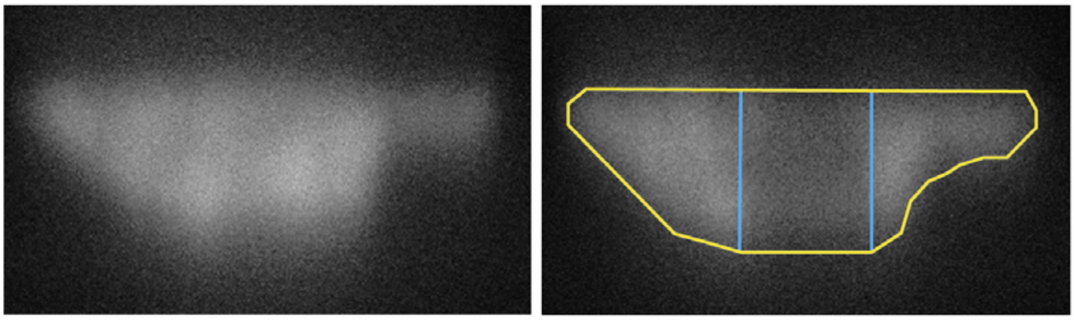

Figure 3.3: Bleach-profile throughout the cell nucleus applying a high NA objective (63x oil immersion, NA = 1.4). The left image shows the prebleach image of a GFP stained nucleus (imaged in xz-mode), on the right the bleached channel is marked in blue and in fact permeates the whole nucleus (yellow).

Measurement

Cells stably expressing GFP-HP1α as well as transiently transfected cells expressing GFP-HP1β were measured. Only cells showing a natural expression level were evaluated after a standardized measurement procedure (Table 3.6) was applied:

	Pre- and postbleach imaging	Bleaching process
Image	whole nucleus	region of interest, zoom-in
Number of images	50 pre-, 500 postbleach	2
Activated laser-lines (nm)	(argon) 488 at 7-10 %	(UV) 405, (argon) 458, 476, 488, 496 and 514 simultaneously at 100 %
Scan speed (Hz)	1400	1400
Line average	No	No
Gain (V)	1250	1250

Table 3.6: Standard protocol for FRAP.

A total of 50 prebleach pictures was taken to be able to do a good averaging. How many postbleaches have to be taken depends on recovery time and was set according to experience to 500 images, according to 56 s.

Both FRAP methods, strip-bleach FRAP (sFRAP) and intensity FRAP (iFRAP), do not differ in this bleach and acquisition protocol. The only difference in performance of the experiments is the varying shape of the ROI. Whereas in iFRAP experiments a quadratic ROI of 2 x 2 µm was chosen and bleached, the ROI for sFRAP was chosen rectangular, 3 µm in height and completely through the whole cell in horizontal direction. Both times the attempt was made to mark the ROI preferably in the middle of the cell – far away from membrane restrictions.

Bleaching a relatively broad strip throughout the cell no distinction of different regions can be made in sFRAP and experimental results give values according to more global characteristics. But being able to choose relatively small regions of interest in iFRAP measurements, a comparison of dynamic properties of different regions as for example euchromatin and heterochromatin was made. Minimum ten measurements were carried out with each method and for each region.

Data analysis

Image analysis and experimental evaluation by application of mathematical models differed for temporally resolved iFRAP and spatial-temporally resolved sFRAP as described in Chapters 2.3.1. and 2.3.2.

After bleaching a strip-shaped ROI the intensity became averaged in parallel to the strip and an intensity profile was analyzed perpendicular to it for each picture of the time series. The profile normalized to the averaged prebleach values was evaluated. Because in this case only the broadening and shape variation of the profile was analyzed over time, further correction steps were not necessary (compare Fig. 4.7).

Assuming the intensity to be proportional to the dye concentration and therefore to the protein concentration, Eq. 2.22 was fitted to the profiles applying a Levenberg-Marquardt non-linear least-square fitting procedure:

$$c(y,t) = 1 - \frac{p}{2}\left[erf\left(\frac{a-y}{\sigma(t)} \right) + erf\left(\frac{a+y}{\sigma(t)} \right) \right] \qquad (3.1)$$

with $\sigma(t) = \sqrt{4Dt}$. The half strip width a was known to be ~1.5 µm. Nevertheless, a was included as a fit parameter within the first 10 curves because of inaccuracy of bleaching. Even in the first postbleach image the profile was not rectangular as assumed in the ideal case, but smeared out due to fast diffusion. An averaged value was fixed for further fitting. The bleaching depth parameter p was also fitted for the first 10 curves, averaged and fixed for subsequent fitting. After fitting all profiles for the first 5.6 seconds (the first 50 images), $\sigma(t)^2$ was plotted versus time. This graph reveals the global diffusion coefficient within the nucleus either for linear or for confined diffusion (compare Chapter 2.3.2).

The step to establish the profile-plot was done using a plug-in for Image J (written by Dr. M. Wachsmuth). Further calculations and fitting procedures were completed using Microsoft Excel 2000 and Microcal Origin (Microcal Origin, Northampton, USA).

In iFRAP-evaluation just the spatial intensity variations due to re-equilibration over time within the marked ROI are evaluated. But this time, as illustrated in Fig. 3.4, the intensity must be quantitated and therefore some correction steps have to be applied.

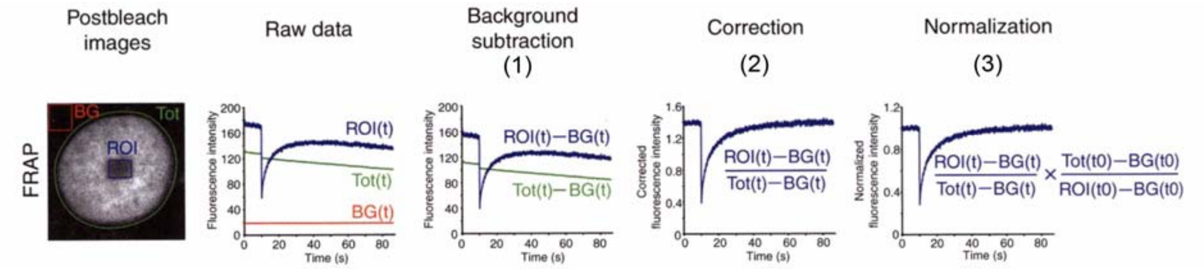

Figure 3.4: iFRAP correction steps. In the microscopy image the different regions are defined, further on the correction steps are illustrated. Graphic taken from (Rabut and Ellenberg, 2005).

Before image analysis it has to be checked if the cells moved within the imaging time and images have to be aligned if necessary. Here, cell movement did not exceed one pixel and could be neglected.

The average pixel value always contains background fluorescence e.g. from the medium, the cover slip, the objective etc., so do pixel values of the ROI. Therefore the averaged intensity of the ROI and all other average intensity values have to be background subtracted, this is illustrated in (1) of Fig. 3.4. The average background value was calculated for a non-stained area outside the cell. Because of photobleaching a large amount of fluorophores within the ROI as well as acquisition photobleaching and laser intensity-fluctuations can cause intensity changes that are not relevant for redistribution due to kinetic processes. These influences have to be considered and corrected. This can be done by normalizing to the total amount of fluorophores available in the image plane, as dividing the background subtracted ROI-intensity values by total cell intensity (also background subtracted) at each time point (2). Finally to be able to compare different measurements the corrected intensity curve must be normalized to the respective averaged prebleach values (3). The resulting curves were analyzed with the mathematical models discussed in section 2.3.1.

A first guess which mathematical model should be applied, can be made analyzing the shape of the strip-profile: The flattening of the slopes shows the tendency to a diffusion dominated case. Nevertheless all three cases were tested which fits best to the recovery curves.

For the diffusion dominated case data were fitted to Eq. 2.20. The fit-formula for recovery due to binding reactions was set proportional to exponential recovery as shown in Eq. 2.16, but was supplemented to calculate also values for the fraction of incomplete bleaching $f_{unbleached} = I_{post}$ (when containing also the fraction of fast diffusive species, $f_{highly\ mobile}$, respectively) and the value of total recovery I_{end}. Thus, an analysis for immobile and mobile fraction was done by fitting to Eq. 3.2:

$$I(t) = I_{post}(0) + [I_{end}(\infty) - I_{post}(0)] \cdot [1 - \exp(-k_{off}\, t)] \tag{3.2}$$

unbleached fraction: $f_{unbleached} = I_{post}$

immobile fraction: $f_{immo} = 1 - I_{end}$

mobile fraction: $f_{mobile} = 1 - I_{end} - I_{post}$ (3.3)

For aligning data to a diffusion-reaction model a linear superposition of both diffusion and reaction equations, was fitted, each multiplied with a weighting factor *f*:

$$\begin{aligned} I(t) &= I_{post}(0) + \\ &+ f_{diff}\left\{1 - p\left(\left[\sqrt{\frac{Dt}{\pi a^2}}\left(1 - \exp\left(-\frac{a^2}{Dt}\right)\right) - erf\left(\sqrt{\frac{a^2}{Dt}}\right)\right]\cdot\left[\sqrt{\frac{Dt}{\pi b^2}}\left(1 - \exp\left(-\frac{b^2}{Dt}\right)\right) - erf\left(\sqrt{\frac{b^2}{Dt}}\right)\right]\right)\right\} + \\ &+ f_{bind}\{1 - \exp(-k_{off} t)\} \end{aligned} \tag{3.4}$$

Software used for this evaluation was Image J for calculation of the averaged intensities of all regions and Microsoft Excel to do the correction-calculations. To be able to do these evaluation steps less time-consuming, the averaging and correction was automated applying a homemade program, the FrapImageAnalyser, written in Matlab (MathWorks, USA) by Gerrit Heuvelman. Curve fitting was done again with Microcal Origin.

3.5. Fluorescence correlation spectroscopy

FCS instrumentation

All FCS measurements were carried out on a commercial available system Leica TCS SP2 AOBS FCS2 based on a Leica Confocal Microscope TCS SP2 AOBS (Leica Microsystems CMS GmbH, Mannheim) equipped with high sensitivity single photon counting avalanche photodiodes APDs (SPC-AQR-14, Perkin Elmer Optoelectronics, Fremont, CA, USA). The scanning mirrors were fixed at the chosen measurement positions. Excitation of GFP or Alexa 488 was done with the argon-laser line 488 nm. For intracellular measurements a HCX UPlanApo 63x/1.2 NA water immersion objective (Leica Microsystems CMS GmbH, Wetzlar, Germany) with correction collar was used. Water as immersion liquid is more suitable for live cell imaging as its refraction index is closer to the refraction index of the cell. Fluctuation data were recorded with the software Vista 3.6.22 LE (ISS Inc., Champaign, IL, USA). The autocorrelation data were computed with the program Fluctuation Analyzer (version 1.1, 2007, by M. Wachsmuth).

Cells and Alexa 488 solution

Cells were prepared as described above: Grown in Lab-Tek chambers and transfected the day before measurement. Also this time measurements were carried out at room temperature within about 2 hours and again L15 medium was used.

For measurements in cells transiently transfected with EGFP-mLSD1 or -hLSD1 Hoechst (Hoechst 33342, Invitrogen, Molecular Probes, Eugene, Oregon, USA) was needed as an additive to identify heterochromatin regions. Hoechst intercalates with the DNA double strand and marks the chromatic regions. Therefore 1 µg/ml Hoechst was added to the medium about 20 min before the FCS measurement.

As a calibration standard Alexa 488 C5 maleimide (Invitrogen, Molecular probes) dilution was used. Therefore a stock solution of Alexa 488 in water was prepared, whose concentration was measured with a Nanodrop (Spectrophotometer ND-1000, peqLab, Erlangen, Germany) to 12.3 µM. For FCS measurement this solution was diluted 1000-fold to reach a concentration of about 12.3 nM. The diffusion coefficient $D_{Alexa488} = (2.1 \pm 0.21) \cdot 10^{-6}$ cm²/s for Alexa 488 in water at room temperature was adapted from (Wachsmuth, 2001).

Instrument calibration

Each series of measurement started with (hardware-) alignment and calibration steps. Because interesting biological information from living cells are strongly position dependent, an exact position localization of the diffraction-limited excitation volume is essentially to account for a possible offset or hysteresis effects of beam scanner and motorized stage (Wachsmuth and Weisshardt, 2007). This necessitates a position calibration before each series of measurement within living cells.

This kind of calibration was done using a chromaslide instead of a cell sample. The chromaslide provides a homogeneous fluorescent layer and is ideally suited for calibration. After choosing a position in the pre-recorded image and bleaching for about one or two seconds with 100 % laser power the theoretical bleaching position can be compared to the effectively bleached position in the subsequently recorded image. If necessary the position of the selection marker must be readjusted.

To check the alignment, five points distributed over the whole image were bleached and the location of the bleaching position was evaluated (Fig. 3.5). The accuracy of the correlation was found to be dependent on the position in the image.

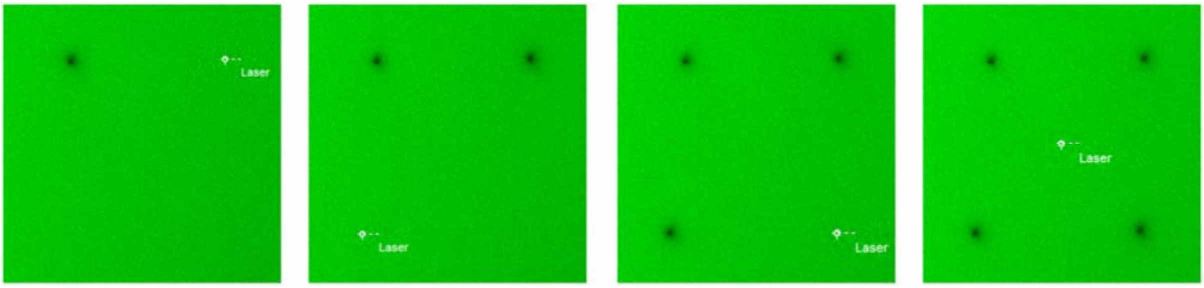

Figure 3.5: Illustration of alignment check.

To obtain an aberration-free focus with a high-*NA* water-immersion objective one has to account for varying cover glass height. This was done by adjusting the correction collar of the objective (objectives with high *NA* are sensitive to variances in cover glass height (Tewes, 1998)). This parameter was adjusted by scanning vertically (xz-plane) in reflection mode. While imaging the reflection of the upper rim with high amplification, the correction ring was carefully set to show the image as sharp as possible. FCS measurements in a fluorescent dye solution were made with a fixed focus about 20 µm above the cover glass.

Measurement

First fluctuation data of a reference standard, namely Alexa 488 C5 maleimide solved in water were recorded. As a solution with only one freely diffusing component and known diffusion coefficient it is ideally suited to determine the device-specific parameters, like κ, z_0 and ω_0. At least three (up to ten) measurements, 60 seconds each, were performed and evaluated with the program Vista 3.6.22 LE to check if κ was in the correct range. These measurements were also used to determine the effective volume of the focus volume, local concentrations of proteins and diffusion coefficients.

In vivo-measurements were carried out with transfected cells and with cells stably expressing the proteins of interest. In both cases cells showing not too bright fluorescence signal were chosen for FCS, i.e. cells not overexpressing the fluorescence tagged protein.

For FCS measurements in living cells the combination of a confocal microscope and the FCS measuring unit is favorable, because a high quality image of the cell was taken and a region of interest was chosen before measuring the fluctuations (Fig. 3.6). Within cells expressing subtypes of EGFP-HP1 and EGFP-LSD1 three different regions are of special interest: Measurements in cytoplasm revealed the freely diffusing species, and from data in euchromatin and heterochromatin information of differences between their function in chromatin dynamics were obtained.

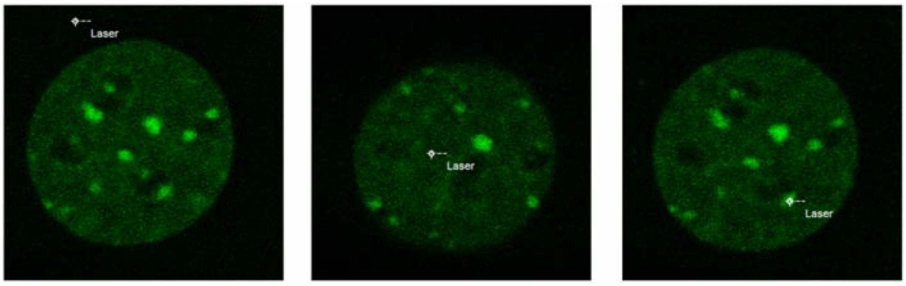

Figure 3.6: Confocal images with the different measurement positions indicated for FCS. Here, a 3T3 cell expressing GFP-HP1α is shown.

In each cell one or two measurements in each of these three regions were conducted for 60 s. Laser power was kept at a low level with a count-rate in between 40 and 200 kHz. The acquisition frequency was set to be 24 MHz.

For measurements over longer time spans cell movement and hardware drift are a serious problem. To check for a translocation of the cell, images were taken before and promptly after FCS-measurement under identical conditions.

Data analysis

As mentioned above, the calculation of autocorrelation function was done with the program Fluctuation Analyzer. The photocount signal was imported as raw data and the fluorescence signal over the whole measurement time was displayed. For the analysis a 15 – 35 s interval of the intensity trace was selected, in which cells did not move and no photobleaching or other disturbances were apparent (Fig. 3.7).

To compute normalized autocorrelation functions the base frequency, i.e. the minimum lag time has to be selected. To reduce noise in ACF curves a minimum lag time τ of 10 µs (equivalent to a base frequency of 100 kHz) was chosen.

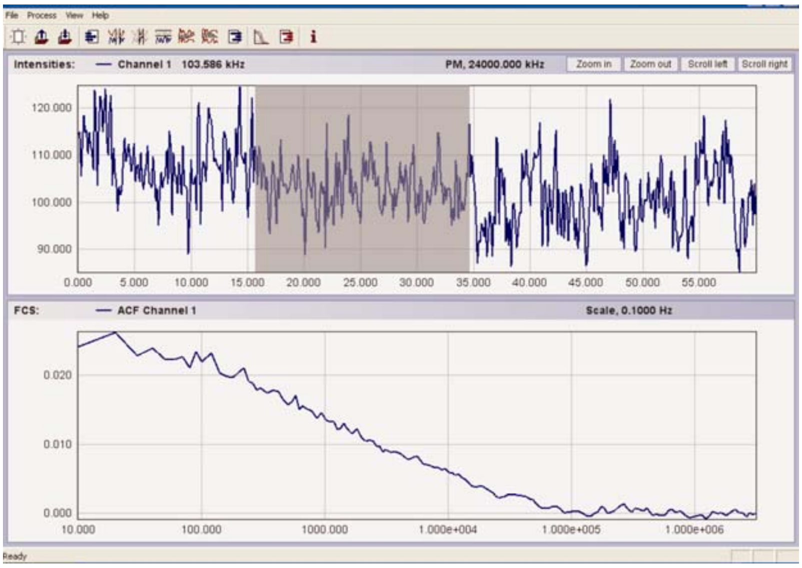

Figure 3.7: Calculation of the ACF from raw data from a HP1α–measurement in euchromatin using the program Fluctuation Analyzer. Raw data are shown in the upper part of the program window. The selected region is marked and the resulting ACF curve is shown beneath (linear scales).

An additional contribution to the fluorescence fluctuation signal is the shift of some chromophores to an irreversible non-fluorescent state. This photobleaching can be significant within a small (solution-)volume like that of a cell, where fluorescent molecules cross more than once the focal volume, might diffuse slowly through the illuminated space or become immobilized. Bleaching leads to an apparently shorter diffusion time τ_{diff}. Laser intensity was chosen to have good signal intensity while minimizing the bleaching effect at the same time.

A possibility to account for this undesired influence to the fluctuation signals is implemented in the Fluctuation Analyzer-software: The application of the trend correction mode allowed it to remove slower large-scale fluctuations on a favored timescale. Here, a correction frequency of 0.1 Hz was applied, i.e. fluctuations slower than 10 s were averaged out to correct for a photobleaching related intensity decrease. Trend corrected autocorrelation data were exported from Fluctuation Analyzer and fitted to the mathematical models described in Chapter 2.4.

So far it was assumed that only particle movement contributes to intensity fluctuations but fluorescent dyes introduce their own dynamics into the system: As mentioned in Chapter 2.1.2. continuous photon emission can be disrupted when molecules occupy the quantum mechanical forbidden triplet state. This state is photoinducable and its occupancy Θ_l depends on excitation intensity. The life span of the triplet states is about µs and therefore is resolved in FCS measurements. The ACF shows an additional shoulder in the measurement curve as illustrated in Fig. 3.8. To correct for the increased ACF-amplitude, which decays at short times with a typical time constant τ_{trip}, we have to multiply by an approximated correction factor (Wachsmuth, 2001; Wachsmuth et al., 2000):

$$G_{corr}(\tau) = \left(1 - \Theta_1 + \Theta_1 \exp(-\tau/\tau_{trip})\right) \cdot G_{diff}(\tau) \tag{3.5}$$

Accordingly, curve fitting was always accomplished with a model function supplemented for triplet correction. The value of τ_{trip} was fixed to 100 µs for GFP blinking – as an average between fastest blinking events of GFP (about 30 µs) and slowest of about 300 µs, for Alexa 488 τ_{trip} was in the range of 5 µs.

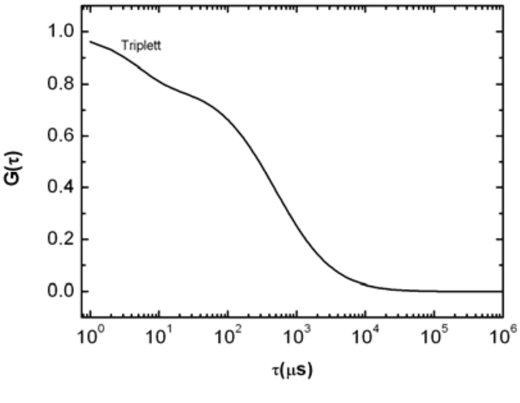

Figure 3.8: Fluorescence dynamics in ACF curves. The phosphorescence from the triplet state (Θ_l = 0.2 and τ_{trip} = 5 µs) leads to an additional shoulder in the ACF curve at early times. Other parameters are given to: N = 1, τ_{diff} = 500 µs and κ = 4.

For instrument calibration Alexa 488 was measured in water and the $G_{diff}(\tau)$ of free diffusion model for a single component (Eq. 2.25) was inserted in Eq. 3.5. The diffusion coefficient of Alexa 488 in water was used to calculate the lateral and axial beam dimension as well as the effective focus volume:

$$\omega_0 = \sqrt{4D\tau_{diff}}$$

$$z_0 = \kappa \cdot \omega_0$$

$$V_{eff} = \pi^{3/2} \cdot r_0^{\ 2} \cdot \omega_0 \qquad (3.6)$$

The averaged structure parameter κ was taken as a device-specific parameter and was fixed for subsequent curve fitting of the data.

For measurements in cytoplasm a one-component, anomalous diffusion model (Eq. 2.28) was chosen to fit the ACFs. In euchromatin as well as in heterochromatin at least two species were detected. Therefore a two-component anomalous diffusion model was fitted to the autocorrelation functions (combining Eq. 2.27 and Eq. 2.28):

$$G(\tau) = \frac{1}{N}\left(1-\Theta_1+\Theta_1\exp(-\tau/\tau_{trip})\right)\cdot$$

$$\left[f_1\left(1+\left(\frac{\tau}{\tau_{diff,1}}\right)^{\alpha_1}\right)^{-1}\left(1+\frac{1}{\kappa^2}\left(\frac{\tau}{\tau_{diff,1}}\right)^{\alpha_1}\right)^{-1/2}+(1-f_1)\left(1+\left(\frac{\tau}{\tau_{diff,2}}\right)^{\alpha_2}\right)^{-1}\left(1+\frac{1}{\kappa^2}\left(\frac{\tau}{\tau_{diff,2}}\right)^{\alpha_2}\right)^{-1/2}\right] \qquad (3.7)$$

Resulting in a fraction f_1 of species 1 that traverses the focus within $\tau_{diff,1}$ and the fraction $f_2 = 1-f_1$ according to species 2 with $\tau_{diff,2}$. The values of α reveal the type of diffusion (simple/free, anomalous, superdiffusive).

Assuming that the second species in euchromatin and/or heterochromatin is bound to immobile or slowly moving structures the second fraction can be fitted by the confined diffusion model (Eq. 2.29). The second part $(1-f_1)\cdot\ldots$ was displaced by $(1-f_1)\cdot G_{bound}(\tau)\cdot N$.

The diffusion time τ_{diff} is related to the diffusion coefficient according to $\tau_{diff} = \omega_0^2/4D$. Because ω_0^2 is known from the Alexa 488-calibration as $\omega_0^2 = 4D_{Alexa488}\tau_{diff,Alexa488}$, the diffusion coefficients of the proteins of interest can be calculated according to Eq. 3.8:

$$D_{protein} = \frac{D_{Alexa488}\tau_{diff,Alexa488}}{\tau_{diff,protein}} \tag{3.8}$$

In addition, the local concentration of the protein was computed:

$$c = \frac{V_{eff}}{N} \quad \text{or} \quad c_{protein} = \frac{c_{Alexa488}N_{protein}}{N_{Alexa488}} \tag{3.9}$$

3.6. Computation of hydrodynamic parameters

VMD, Amber and HYDROPRO

To compare some theoretical values of diffusion coefficients with the measured data, computer based simulations were conducted. The molecular visualization program VMD (visual molecular dynamics, www.ks.uiuc.edu/Research/vmd, (Humphrey et al., 1996)) was used to built structures of HP1-dimers tagged with GFP. Hydrodynamic simulations of its behavior in aqueous solutions were carried out using HYDROPRO (version 7c, 2005; (Garcia De La Torre et al., 2000)). The pdb (protein data bank)-coordinates of the HP1-dimer were provided by Sabine Kaltofen. This HP1-dimer structure was extended with one or two GFP-molecules, one at each protein monomer, illustrating the possible homo- or heterodimeric structures that can result depending on expression levels of endogenous and fusion proteins. The used GFP structure 1ema was published by M. Ormo (Ormo et al., 1996). Between HP1 and GFP exists a linker of 14 amino acids, which was included using VMD. Energy minimizing procedure and short molecular dynamics simulations were carried out with Amber 9 (http://ambermd.org/, (Case et al., 2006; Pearlman et al., 1995)) (done by Dr. N. Kepper).

For hydrodynamic simulations HYDROPRO-software was used. HYDROPRO computes the hydrodynamic characteristics of globular proteins, approximated as rigid macromolecules, from their atomic-level structure. The software uses a sphere model, which replaces atomic structure by spheres of user defined size. Here, a sphere radius of 3.1 Å was used. Further input parameters for hydrodynamic simulation, like molecular weight and the partial specific volume $\bar{v}$, were calculated using the program Sednterp (Sedimentation interpretation program, version 1.09, Hayes D.B. et al, University of New Hampshire, 1995).

The hydrodynamic parameters of HP1-monomer, HP1-dimer and of the dimer carrying one or two EGFPs were calculated. The diffusion and friction coefficient were of particular interest (the latter calculated from sedimentation coefficients: $f = M(1-\bar{v}\rho)/N_A s$ with M being the molar mass, ρ the solution density and N_A the Avogadro number).

Based on the knowledge of the molecular weight m and the partial specific volume the diffusion coefficient of a sphere with the same volume was calculated. Assuming HP1 as a globular protein, *D* was computed approximately in this way: The spherical volume of the protein was calculated due to the partial volume and the molar mass M:

$$V_m = \frac{\bar{v}M}{N_A} = \bar{v}m \tag{3.10}$$

with $M = N_A \cdot m$. From the spherical volume the radius R_m was computed and inserted into Stokes law to obtain the friction coefficient.

$$f = 6\pi\eta R_m \tag{3.11}$$

with η = 1.002 mP·*s* as the viscosity of water, *T* = 293 °K and Boltzmann constant k_B = $1.3807 \cdot 10^{-23}$ J/K, *D* is given by the Stokes-Einstein formula:

$$D = \frac{k_B T}{f} = \frac{k_B T}{6\pi\eta R_m} \tag{3.12}$$

Adaptation of theoretical diffusion coefficients to cellular environment

The theoretical diffusion coefficients calculated above reflect diffusion behavior in aqueous media at room temperature that exhibits a viscosity of about 1 mP·s. The viscosity within the cell is apparently higher: Various research groups investigated cytosolic viscosity using different methods and found values of 2.6 to 10-fold higher viscosity in different cell lines (Luby-Phelps et al., 1993; Seksek et al., 1997; Swaminathan et al., 1997; Wachsmuth et al., 2000). Less experiments were carried out directly in the nucleus, but it seems that diffusive behavior is similar in cytosol and nuclei. According to Eq. 3.12 a higher viscosity leads to a lower diffusion coefficient. For measurements in cells the Eq. 3.13 was applied:

$$D_{cell} = 0.32 \cdot D_{water} \tag{3.13}$$

This value is valid for cytoplasm as well as for the nucleus (Beaudouin et al., 2006; Pack et al., 2006). As all simulations and calculations were done for 20 °C, a correction was necessary to adapt diffusion values to 25 °C.

$$D_{25^\circ} = D_{20^\circ} \frac{297^\circ K}{293^\circ K} \cdot \frac{\eta(T = 293K)}{\eta(T = 295K)} \tag{3.14}$$

4. Results

4.1. Localization of HP1 and its interaction partners

The chromatin modifying proteins HP1, Suv39h1 and LSD1 were visualized in living cells by CLSM. 3T3 cells, transiently transfected with GFP-/TagRFP-HP1β, GFP-Suv39h1 or GFP-LSD1 and cells constitutively expressing GFP-HP1α or GFP-Suv39h1 were studied. To be able to compare protein localization and DNA density within the nucleus, chromatin was stained with DAPI.

GFP-HP1α and -HP1β fusion proteins localized predominantly in intensely labeled nuclear heterochromatin domains (Fig. 4.1 A, C and D). However, both isoforms also showed a relatively constant distribution throughout the nucleus (Fig. 4.1 A, B). The same distribution was observed when cells were transfected with TagRFP-HP1β.

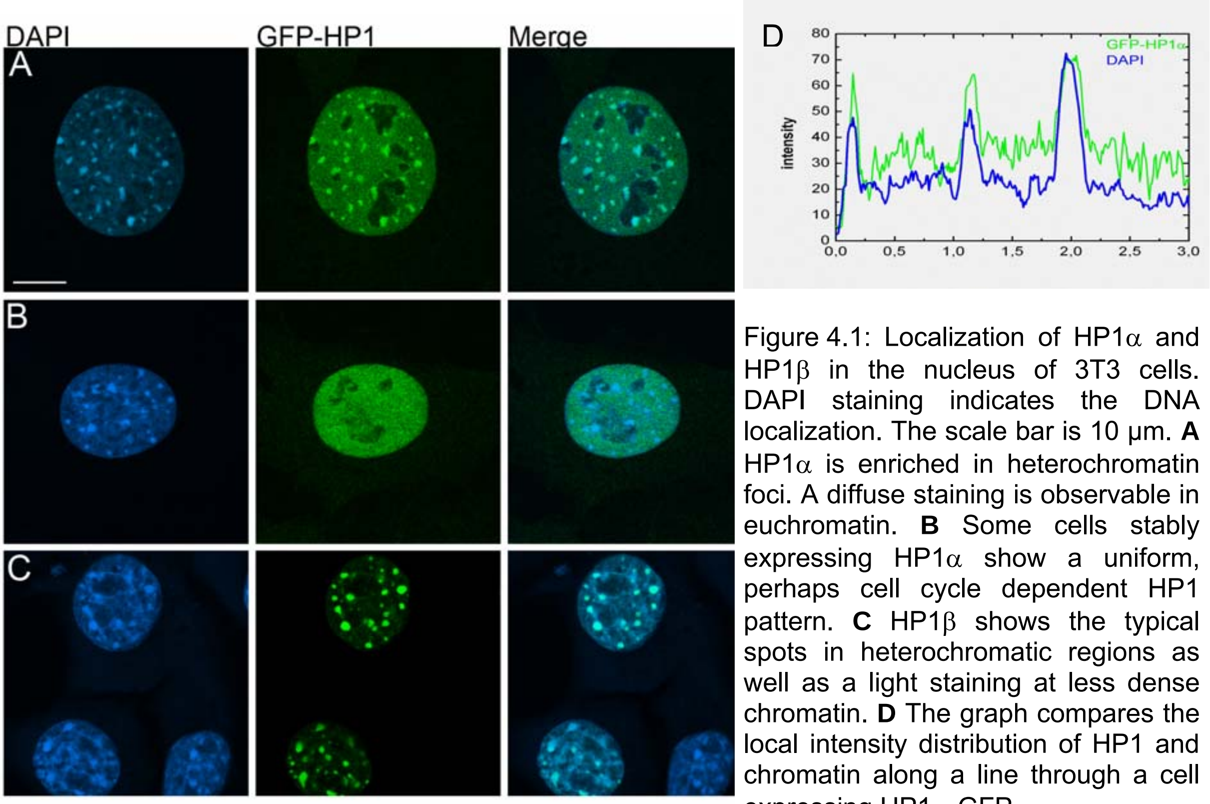

Figure 4.1: Localization of HP1α and HP1β in the nucleus of 3T3 cells. DAPI staining indicates the DNA localization. The scale bar is 10 µm. **A** HP1α is enriched in heterochromatin foci. A diffuse staining is observable in euchromatin. **B** Some cells stably expressing HP1α show a uniform, perhaps cell cycle dependent HP1 pattern. **C** HP1β shows the typical spots in heterochromatic regions as well as a light staining at less dense chromatin. **D** The graph compares the local intensity distribution of HP1 and chromatin along a line through a cell expressing HP1α-GFP.

In the stable HP1α-3T3 cell line a relatively large fraction of cells was observed that showed no distinct heterochromatin localization of HP1 (Fig. 4.1 B). In these cells HP1 was equally distributed throughout the nucleus. A correlation with the cell cycle could not be confirmed or assigned to a distinct step in the cell cycle via cotransfection with PCNA (Proliferating Cell Nuclear Antigen) as a marker of the S-phase of the cell cycle.

In addition to HP1, the localization of Suv39h1 and LSD1 was investigated (Fig. 4.2).

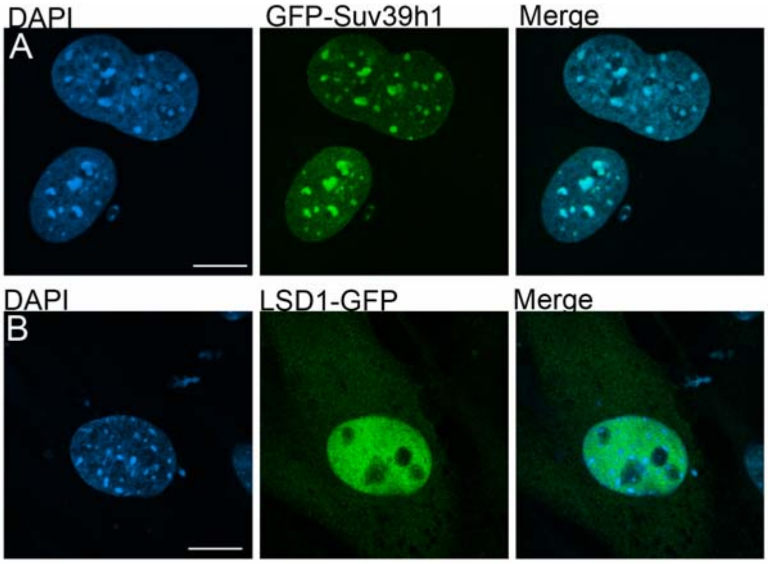

Figure 4.2: Distribution pattern of Suv39h1 and LSD1. Scale bars indicate 10 µm. **A** The GFP-Suv39h1 pattern was comparable to that of chromatin, i.e. intensified staining according to higher accumulation of Suv39h1 within heterochromatin and faint staining in euchromatin. **B** LSD1 operates mainly in euchromatin and therefore showed bright staining in euchromatin regions, foci of heterochromatin seem to be omitted.

As could be expected because of their cooperation in heterochromatin formation and maintenance, the localization pattern of Suv39h1 was identically to that of HP1. This colocalization pattern was confirmed by cotransfection of 3T3 fibroblasts with GFP-Suv39h1 and TagRFP-HP1β (Fig. 4.3). A totally different localization pattern was observed for LSD1-GFP. This histone demethylating protein can be found mainly in euchromatic regions where heterochromatin foci are absent (Fig. 4.2 B).

The HP1 distribution and chromatin density was compared by evaluating six spots on the microscope images of at least 10 cells. The mean intensity values of DAPI staining showed that chromatin is twice as dense in heterochromatin as in euchromatin (2.0 ± 0.3 : 1). HP1α showed a ~2-fold higher intensity in heterochromatin as compared to euchromatin (1.9 ± 0.5 : 1). For HP1β a 4.4-fold (± 1.3) intensity in heterochromatin as compared to euchromatin was determined. Therefore it appears likely that the HP1 localization is proportional to the local concentration of its binding sites.

Furthermore, measurements of 3T3 nuclei yielded a mean width of 13.4 ± 2.1 µm and a height of 5.7 ± 0.8 µm corresponding to a cellular volume of about 0.5 ± 0.002 pl.

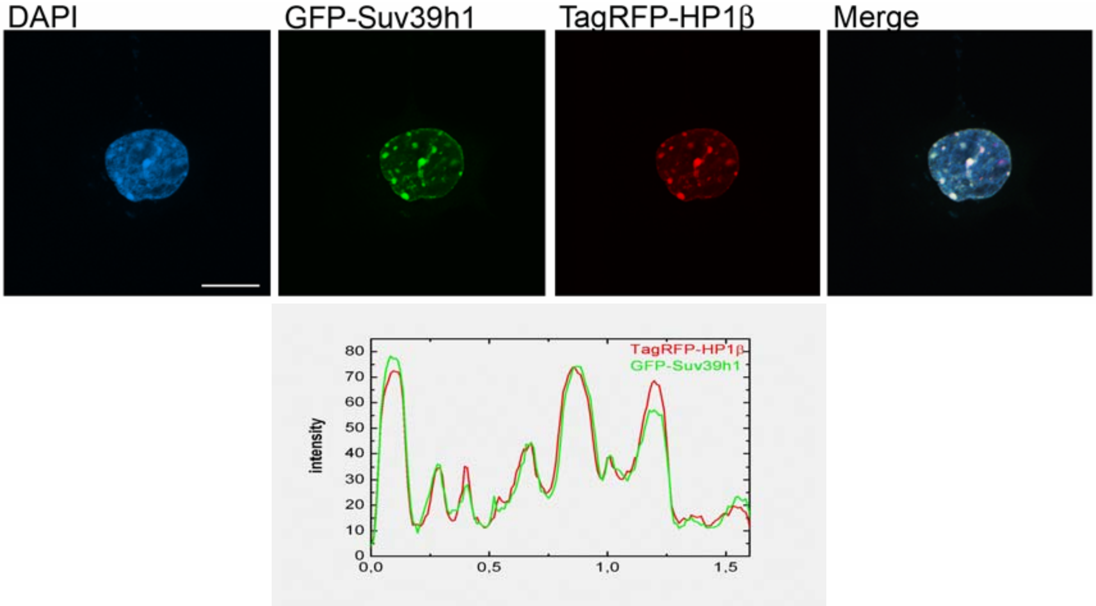

Figure 4.3: Colocalization of Suv39h1 and HP1β. Cotransfection of Suv39h1 (green) and HP1 (red) reveals that both chromatin modifying proteins localize exactly at the same sites. Plotting the intensity distribution of both proteins along a line through the imaged cell confirms the uniform localization of both.

RNase microinjection experiments

To asses the role of noncoding (nc) RNA in HP1 binding to chromatin some types of RNase were microinjected in 3T3 cells stably expressing HP1α. Injection of RNases III, H and Orn showed no effects as compared to the control cells (data not shown). RNase A effected both HP1 localization and chromatin structure even at low dosage (0.7 to 1 u per 10 µl mix). The chromatin structure was slightly perforated. At higher dosage of RNase the DNA seems to aggregate around heterochromatic foci (compare Fig. 4.4 C or D). As can be seen at the control cells (Fig. 4.4 A) the buffers contained in the reaction mix did not influence the cellular system. Cells stayed healthy for at least 24 hours after injection (data not shown).

To estimate how HP1 responds to RNase A treatment, e.g. in which regions the detachment starts, different RNase dilutions were prepared and injected. Furthermore, an evaluation after different incubation times was implemented. The time course of incubation times did not reveal intermediates of the detachment processes itself. Even when fixation was made directly after injection (the injection process itself lasted about 15 min), HP1 was already detached and chromatin structure was distorted.

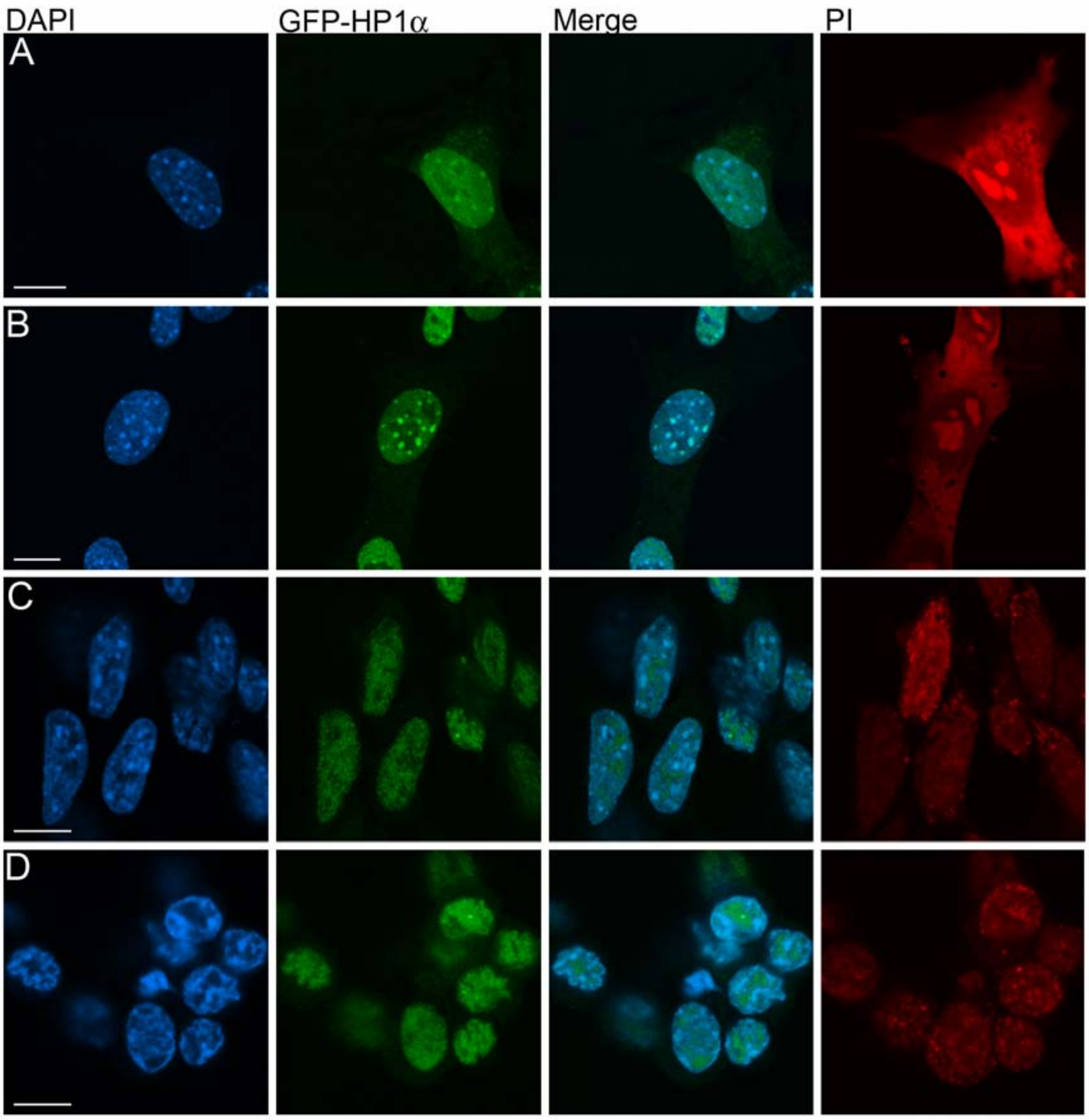

Figure 4.4: Cellular structures after injection with different RNase A concentrations in 3T3 cells. DAPI marks the chromatin strands, GFP-HP1α is stably expressed by this cell line and PI staining, in the last row, indicates which cells were injected. Regeneration time for all of these samples was 30 min after injection procedure. Scale bars are 10 µm. **A** Control cell that was injected with a buffer mix not containing RNase; cells stayed healthy. **B** Injection of low dosed RNase mix containing only 0.1 u per 10 µl. No deformation was observed. **C** First signs of the influence of RNase A (0.7 u per 10 µl mix) on HP1 binding as well as on chromatin structure. HP1 detached from heterochromatin and dispersed throughout the whole nucleus; the chromatin itself became holey. **D** High dosage of RNase A (7 u per 10 µl) destroyed euchromatin structure completely and caused the expulsion of HP1 out of chromatin agglomeration.

The so-called dilution experiments started with injection mixes in which the RNase concentration was raised stepwise. Cells that were treated with the lowest dosage of 0.1 u RNase A per 10 µl did not show evidence of RNase treatment (Fig. 4.4 B). In contrast, cells that obtained a dose of 0.7 u RNase A per 10 µl showed a relatively strong response in terms of HP1. The injected cells itself seemed to stay flat and attached to the coverslip, and even the chromatin structure showed only slight changes (small holes) in euchromatin. The heterochromatin foci remained unaltered. But no correlation between heterochromatin foci and HP1 concentration was noticed any more in these cells, HP1 seemed to be totally detached (Fig. 4.4 C). Applying much higher doses of RNase A (about 7 u per 10 µl) chromatin aggregated in distinct regions, probably around former heterochromatin regions, and seemed to displace HP1 from these highly condensed structures (Fig. 4.4 D). Furthermore, cells became rounder: in this case that behavior can be interpreted as a sign of indisposition.

Because HP1 dissociated only when RNase A, which cuts single stranded RNA, was applied, the ncRNA that is part of HP1 binding must be single stranded. RNase H cleavage had no effect on HP1 binding, indicating that this structural RNA was not directly attached to DNA strands.

4.2. HP1-dimer structure and hydrodynamic properties

HP1 forms dimers via its chromoshadow domains (Kaltofen & Rippe, unpublished). To get insight into the spatial arrangement of HP1 proteins forming the dimer and to be able to estimate its hydrodynamic behavior within the cell, a structural model of HP1$_2$-GFP was constructed.

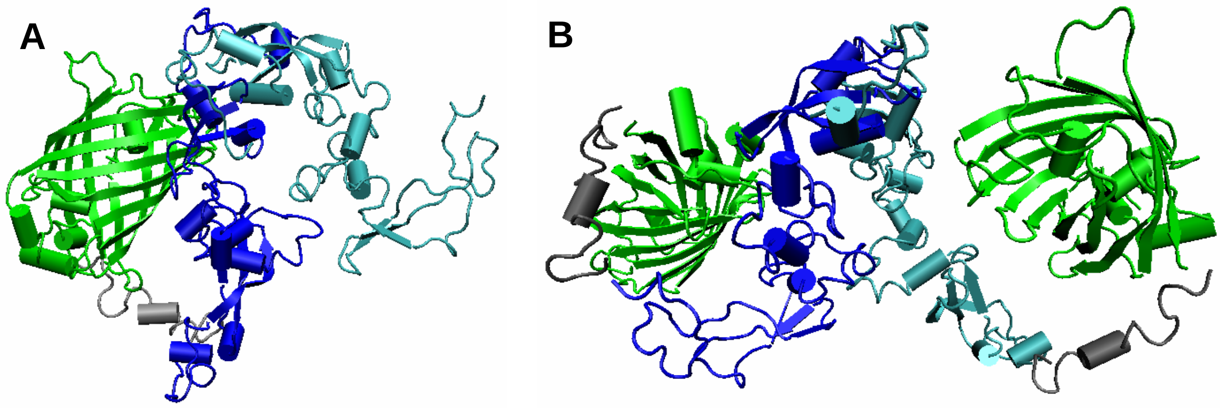

Figure 4.5: Structural model of fluorescently labeled HP1-dimers. GFP barrels are shown in green. HP1-monomers are colorized in blue and cyan, the linker between HP1 and GFP is marked in grey. Both possibilities of fluorescent markers are illustrated: **A** Only one HP1-monomer was fused to GFP and connected via its chromoshadow-domain to an endogenous, unlabeled HP1. **B** Two fusion proteins dimerized and therefore both HP1 proteins carry a GFP at their N-terminus.

The HP1-dimer showed a clamp like structure. Since fluorescently labeled HP1-GFP can form homodimers or bind to an endogenous HP1, both structures were modeled. Figure 4.5 shows the heterodimer as well as the homodimer of HP1-GFP.

The structure model of HP1-dimers was based on the amino acid sequence of HP1β. HP1α and HP1β exhibit a high sequence homology and therefore a similar structure for both variants is expected.

From these structure models the theoretical diffusion coefficients were calculated using HYDROPRO. In addition, also the theoretical values of the HP1-monomer and the unlabeled dimer are shown (Table 4.1).

	HP1	HP1-HP1	GFP-HP1-HP1	GFP-HP1-HP1-GFP
MW [kDa]	21.4	42.8	71.3	99.8
$\bar{v}$ [cm³/g]	0.726	0.726	0.730	0.730
f [kg/s]	$6.1\cdot10^{-11}$	$7.5\cdot10^{-11}$	$7.6\cdot10^{-11}$	$8.5\cdot10^{-11}$
$D_{H2O,20°C}$ [µm²/s]	66.4	53.4	53.5	47.6
$D_{cell,25°C}$ [µm²/s]	24.3	19.5	19.6	17.4

Table 4.1: Hydrodynamic calculations for HP1 and GFP-tagged HP1-dimers.

In contrast to the computations based on molecular modeling the idealized case of $HP1_2$-GFP as a completely globular protein, i.e. as a sphere, was also considered (Table 4.2).

	HP1	HP1-HP1	GFP-HP1-HP1	GFP-HP1-HP1-GFP
f [kg/s]	$3.5\cdot10^{-11}$	$4.4\cdot10^{-11}$	$5.2\cdot10^{-11}$	$5.8\cdot10^{-11}$
$D_{H2O,20°C}$ [µm²/s]	116.9	92.8	78.1	69.8
$D_{cell,25°C}$ [µm²/s]	42.7	33.9	28.6	25.5

Table 4.2: Spherical model – calculations for HP1 and GFP-tagged HP1-dimers.

4.3. Fluorescence recovery after photobleaching

The diffusion and reaction kinetics of HP1 were analyzed by fluorescence recovery after photobleaching. First FRAP experiments with living cells were carried out to check if reversible photobleaching occurs. Therefore HeLa cells were transfected with GFP and the complete cellular region was bleached and observed. Reversible photobleaching can occur due to triplet-state excitation, but this process happens on the µs- to ms-timescale and is not resolved by FRAP. Alternatively fluctuations between bright and dark states on a ms- to s-timescale can occur (Chapter 2.1.2.). The latter phenomenon would be observable with FRAP.

When bleaching GFP, expressed in HeLa cells, we were not able to switch off fluorescence completely. In the analysis of GFP-recovery curves, just a very small amount of recovery due to GFP-dynamics was observed in the first (milli-)seconds (compare Fig. 4.6). With respect to a strong and fast recovery expected in experiments with small bleaching areas this small contribution can be neglected.

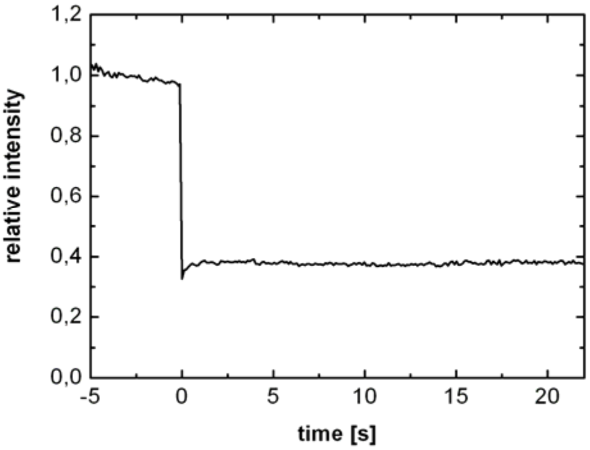

Figure 4.6: Contribution of GFP-dynamics to fluorescence recovery. The green fluorescent protein, GFP, was transfected into HeLa cells and the complete cellular region was bleached. Recovery was observed under the same conditions as described for GFP tagged proteins. Values are background subtracted and normalized to prebleach values (measurement by F. Erdel).

Further introductory FRAP experiments with living cells were applied to estimate the best experimental conditions and to establish a standard protocol for FRAP. These tests resulted in a 2-fold bleaching with UV-laser and all argon-laser lines activated to 100 %, using the zoom-in function of the Leica-software. Zoom-in had the effect to bleach more efficiently as photobleaching efficiency increases proportional to the squared zoom-factor (Rabut and Ellenberg, 2005). To determine the possible time intervals between single imaging frames and to find out the maximum necessary time for full recovery, further tests were carried out. As proteins of interest in this work seemed to diffuse very fast within the cell, tradeoffs had to be made for a better time resolution, i.e. acceleration of imaging. The scan speed was set to the maximum value of 1400 Hz and no averaging was applied. Also the reduction of the number of pixels to 128 x 128 allowed to increase acquisition frequency, to image 1 frame within 112 ms.

4.3.1. Spatially resolved fluorescence recovery after photobleaching

In sFRAP a strip-shaped ROI over the whole cell nucleus with GFP-labeled HP1 was bleached and a one dimensional diffusion analysis was conducted. Taking the profile perpendicular to the strip (Fig. 4.7 A) and analyzing the difference in width of the profile by applying the fit function (Eq. 3.1) reveals $\sigma^2(t)$, which is proportional to the diffusion coefficient (Fig. 4.7 C).

A linear relationship between $\sigma^2(t)$ and the diffusion coefficient D (compare Eq. 2.21) was observed for the first ten images (~1 s). But the $\sigma^2(t)$-values increased fast and the broadening reaches the dimensions of the nucleus. In this case the linear dependence is no longer valid. Consequently the more complex confined diffusion model (Chapter 2.3.2) was used to fit the $\sigma^2(t)$-curve and to determine D. For the confined diffusion model, only profiles of the first 50 images (corresponding to 5.6 s) were evaluated because later profiles were too noisy to extract reliable values. The results of both methods of evaluation are presented in Figure 4.7 D and E.

For ten cells expressing GFP-HP1α and ten cells transfected with GFP-HP1β a strip-shaped ROI was bleached and profiles were evaluated as described above. The linear fit of the first ten values of $\sigma^2(t)$ or fitting all 50 values with a confined diffusion model yielded the same diffusion coefficients (Table 4.3).

D [µm²/s]	Linear fit	Confined fit
HP1α	1.37 ± 0.27	1.41 ± 0.30
HP1β	0.90 ± 0.19	0.92 ± 0.20

Table 4.3: Diffusion coefficients and standard deviation (SD) determined by spatially resolved (s)FRAP

These values for diffusion coefficients are so-called effective or apparent diffusion coefficients. Since the rectangular ROI over the whole cell includes euchromatic as well as heterochromatic regions a possible different diffusion behavior was averaged out. In addition, factors that retard diffusion processes, like binding events or collisions with obstacles are not resolved and contribute to a reduction of the apparent diffusion coefficient.

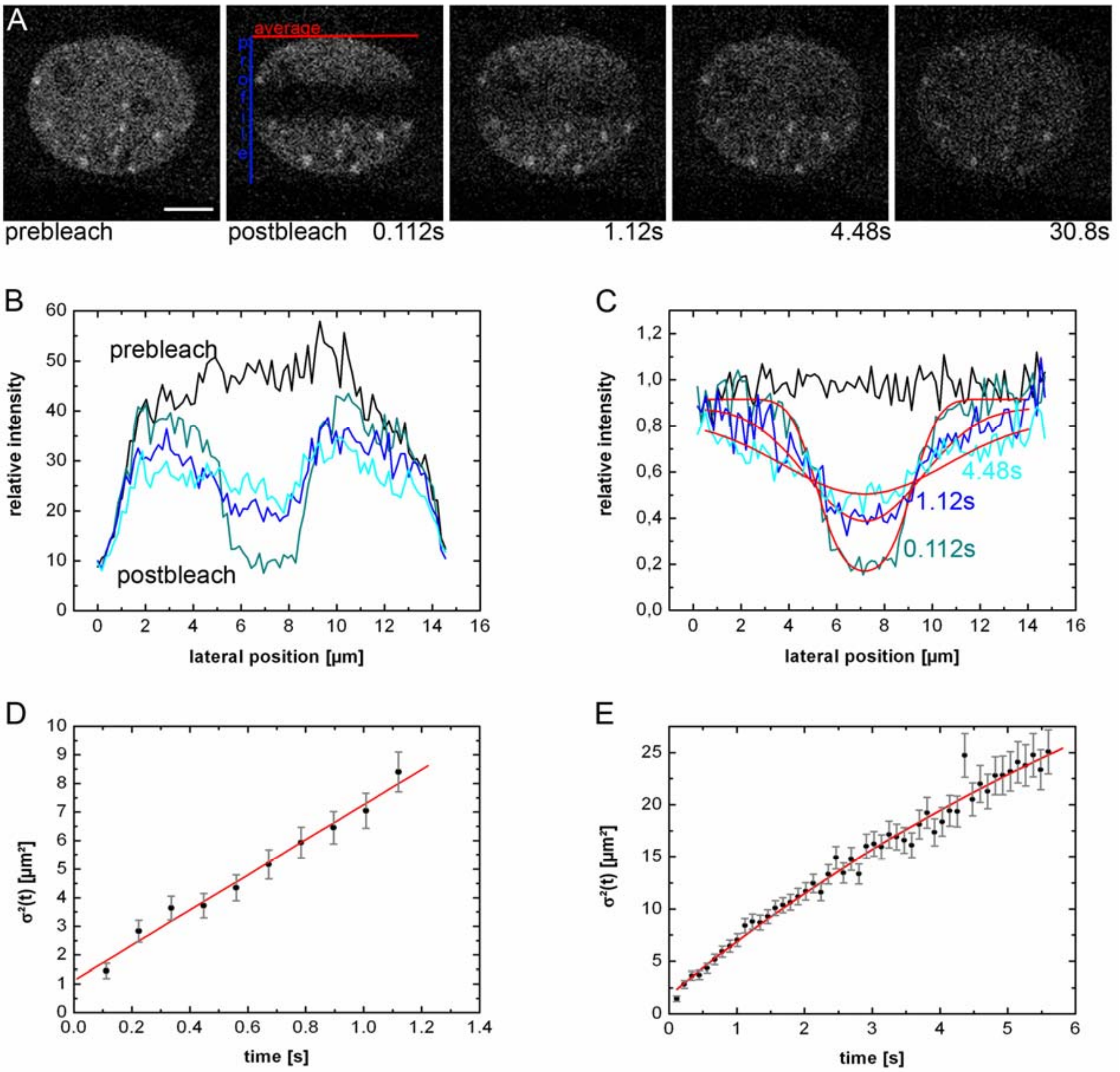

Figure 4.7: Data analysis of FRAP experiments bleaching a strip-shaped ROI (sFRAP). **A** sFRAP time series. Scale bar: 5 µm. **B** Averaged intensity profiles for prebleach, first and later postbleach. **C** The postbleach profiles were normalized to prebleach values. The fitting curves are shown in red. **D** Calculation of the diffusion coefficient assuming a linear dependency of time. **E** The confined diffusion model allowed it to evaluate the profiles of 50 postbleach curves. Error bars in images **D** and **E** are standard errors.

4.3.2. Temporally resolved fluorescence recovery after photobleaching

Although determining the effective diffusion coefficient by sFRAP provides insight into the diffusion kinetics, the possible effect of binding cannot be evaluated. In iFRAP an evaluation with respect to biological conclusions is possible.

Additionally, the discrimination between euchromatin and heterochromatin regions is not feasible, if a big ROI as described above is bleached. Therefore iFRAP experiments with a small quadratic bleach region were conducted in distinct regions of the nucleus. Heterochromatin was identified on the basis of previous localization studies and morphological criteria as regions with a ~2-fold higher GFP intensity.

Fluorescence recovery of HP1α and HP1β was recorded in sequential imaging scans. Exemplary images of an iFRAP measurement are shown in Fig. 4.8 to illustrate the recovery process.

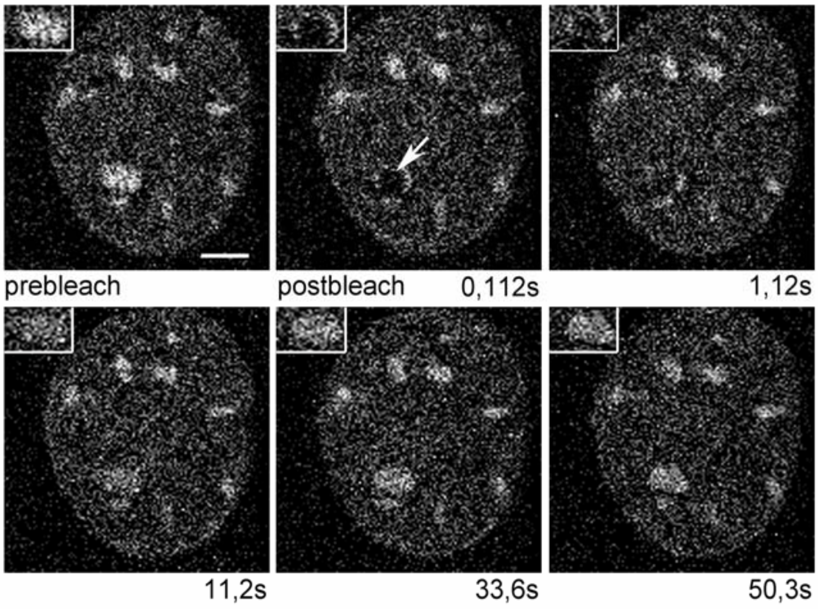

Figure 4.8: iFRAP in living cells expressing GFP-HP1α. A quadratic region (2 µm x 2 µm, indicated by an arrow) was bleached and selected images of a time series are shown. In this case bleaching was done within heterochromatin, insets show a zoomed image of the bleached area. The scale bar is 5 µm.

Initial characterization of iFRAP

Intensity based evaluation of the iFRAP measurements (Fig. 4.9) revealed that the largest fraction of HP1 protein is mobile within the nucleoplasm, in euchromatin as well as in heterochromatin regions. The mobile fraction of stably expressed HP1α comprises 88 % in heterochromatin and 90 % in euchromatin, whereas HP1β, transiently transfected to 3T3 cells, was somewhat less mobile with 77 % in euchromatin and 84 % in heterochromatin. The unbleached fraction contains also a highly mobile part, which diffuses into the ROI already during the bleach process. A higher value for $f_{unbleached}$ in euchromatin than in heterochromatin is due to this highly mobile fraction that can be found especially in euchromatin (Table 4.4). In euchromatin as well as in heterochromatin an immobile or bound fraction was found (at least on timescales of 60 seconds in these measurements). For both isoforms euchromatin contains 5 to 6 % of the protein bound to chromatin structures, whereas heterochromatin has a higher immobilized fraction ranging from 10 % in HP1α to 14 % in HP1β. As evident from the curves, the dynamic of HP1 is faster in euchromatin than in heterochromatin (Fig. 4.9). This behavior is reflected in the half times of recovery, $t_{½}$, being 1.75-fold faster in euchromatin than in heterochromatin for HP1α and 1.6-fold faster for HP1β (Table 4.4).

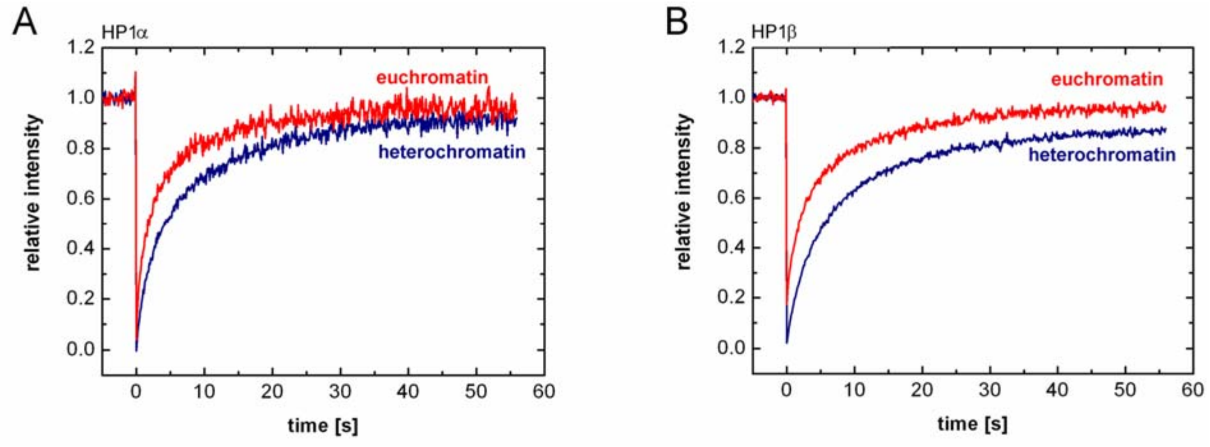

Figure 4.9: iFRAP analysis of GFP-HP1 proteins in euchromatin and heterochromatin of 3T3 cells. Quantitative iFRAP analysis was performed in euchromatin and heterochromatin of cells stably expressing GFP-HP1α (**A**) and cells transiently transfected with GFP-HP1β (**B**). The curves represent average values from at least 10 cells.

	HP1α		HP1β	
	euchromatin	heterochromatin	euchromatin	heterochromatin
f_{immo}	0.05 ± 0.03	0.10 ± 0.09	0.06 ± 0.04	0.14 ± 0.10
f_{mobile}	0.90 ± 0.05	0.88 ± 0.10	0.77 ± 0.11	0.84 ± 0.10
$f_{unbleached}$	0.05 ± 0.03	0.2 ± 0.3	0.17 ± 0.11	0.02 ± 0.02
$t_{½}$ [s]	1.92 ± 0.51	3.36 ± 2.43	2.92 ± 0.98	4.67 ± 1.19

Table 4.4: iFRAP analysis: percentage of all fractions and recovery half times of HP1α and HP1β measured in this study. Although values are average values from 10 to 13 cells, single curves were very noisy and therefore high standard deviation occurs.

The iFRAP measurements demonstrate that HP1 was highly mobile within the nucleoplasm outside heterochromatin domains and a bit less mobile in heterochromatin itself. Throughout the nucleus a small fraction of HP1 was bound. As could be expected, more HP1 was bound within heterochromatin than in euchromatin, but the difference is surprisingly small.

Data analysis

To gain some quantitative information about the distribution of the mobile, diffusive or bound fractions a kinetic modeling of the iFRAP data was performed.

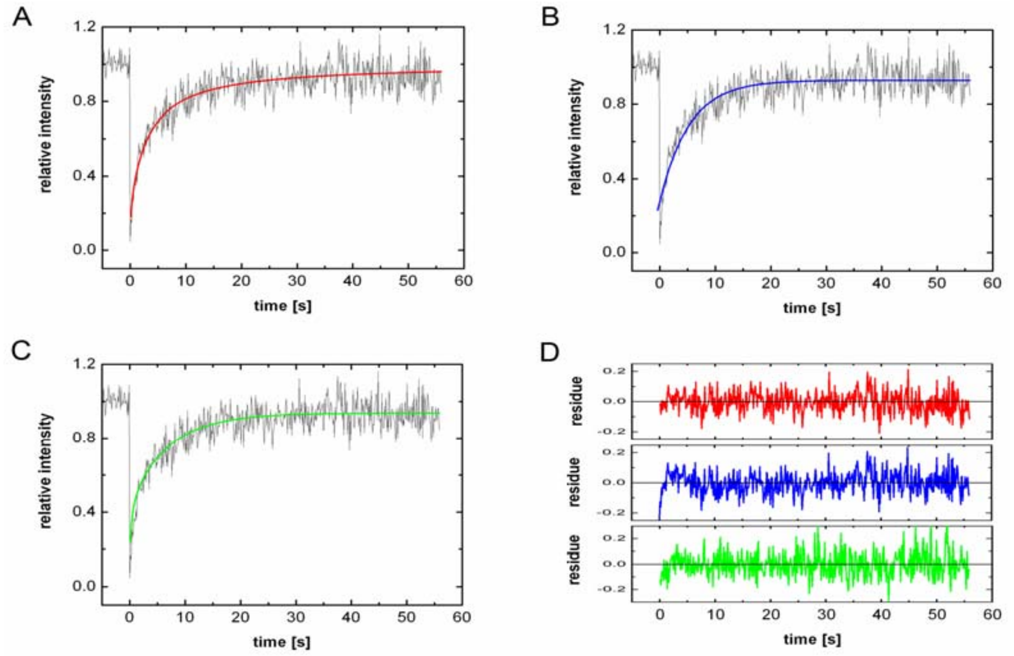

Figure 4.10: Kinetic modeling of the iFRAP data recorded in euchromatin measurements. The different mathematical models used for curve fitting are illustrated for HP1α: **A** Diffusion dominated model (Eq. 2.20). **B** Binding dominated, diffusion-uncoupled model (Eq. 3.2). **C** Combined diffusion-reaction model (Eq. 3.4). **D** Fit residues.

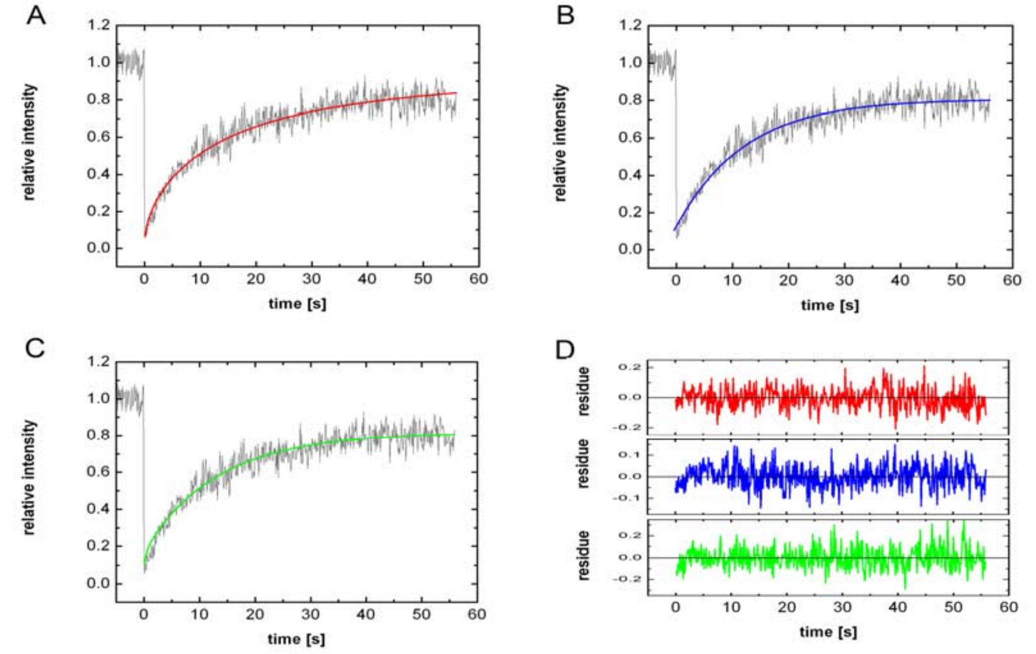

Figure 4.11: Kinetic modeling of the iFRAP data recorded in heterochromatin. Here, the redistribution of HP1α in heterochromatin foci was measured. **A** Diffusion dominated model (Eq. 2.20). **B** Binding dominated, diffusion uncoupled model (Eq. 3.2). **C** Combined diffusion-reaction model (Eq. 3.4). **D** Fit residues.

Diffusion dominated model

Reckoning the shape variation of the profile-plot in sFRAP, a smoothening effect of the slopes over time was observed. Therefore diffusion must be highly involved in the redistribution process. And as illustrated in Figs. 4.10 A and 4.11 A, the relative intensity curve fits exactly to the mathematical model for a diffusion dominated case (Eq. 2.20). However, the resulting diffusion coefficients are too small (Table 4.5). A diffusion coefficient even smaller than the effective diffusion coefficient obtained from the recovery experiments after bleaching a strip-shaped ROI can be excluded. Most likely, binding influences the recovery process more strongly on a longer timescale like that in iFRAP experiments.

D [$\mu m^2/s$]	euchromatin	heterochromatin
HP1α	0.18 ± 0.12	0.11 ± 0.08
HP1β	0.11 ± 0.05	0.06 ± 0.03

Table 4.5: iFRAP analysis: Diffusion coefficients extracted from the diffusion dominated model.

Binding dominated (diffusion-uncoupled) model

To obtain information about the binding processes that are involved in the recovery process a mathematical approach was used that just describes binding processes (Eq. 3.2). From this, kinetic rate constants or residence times ($t_{res} = 1/k_{off}$), mobile and immobile fraction as well as unbleached fraction were extracted.

As anticipated for a $(1-exp(-k_{off} t))$-model, it fails to fit the first sharp increase, that is mainly caused by fast diffusion processes. However, the rest of the curve was aligned appropriately. Particularly in euchromatin this difference between measured values and fitting curve is clearly recognizable (Figs. 4.10 and 4.11 B). For that reason even the resulting values of $f_{unbleached}$ dissent from just being unbleached, this time even the fast diffusive species is enclosed in this fraction. Therefore $f_{unbleached}$ will be renamed to $f_{highly\ mobile}$.

	HP1α		HP1β	
	euchromatin	heterochromatin	euchromatin	heterochromatin
f_{immo}	0.06 ± 0.03	0.09 ± 0.09	0.06 ± 0.05	0.15 ± 0.09
f_{mobile}	0.68 ± 0.07	0.75 ± 0.10	0.61 ± 0.09	0.73 ± 0.09
$f_{highly\ mobile}$	0.26 ± 0.09	0.15 ± 0.11	0.33 ± 0.10	0.12 ± 0.05
k_{off} [s^{-1}]	0.20 ± 0.08	0.15 ± 0.11	0.16 ± 0.05	0.12 ± 0.03
t_{res} [s]	5.4 ± 1.6	8.4 ± 2.7	7.0 ± 2.4	8.6 ± 1.8

Table 4.6: iFRAP analysis: Kinetic modeling of HP1α recovery by a binding dominated model. Dissociation constant k_{off} and residence time characterize the binding process. Values ± SD.

Values of the immobile fraction, f_{immo}, were similar to that obtained in the initial characterization (compare Table 4.6 to Table 4.4), in contrast to f_{mobile} and $f_{highly\ mobile}$ that are shifted because of fitting insufficiency. Dissociation constants of HP1α ranged from 0.2 s^{-1} in euchromatin to 0.15 s^{-1} in heterochromatin and correspond to residence times of 5.4 s to 8.4 s. Nearly the same was observed for HP1β (Table 4.6).

Combined diffusion-reaction model

In order to improve the fits obtained with one-sided, unbalanced models, a combination of both models was also used (Eq. 3.4). First a complete free diffusion-reaction model was fitted, i.e. all parameters were free to vary during fitting procedure. This results in fitting curves that aligned very well with the measured values (Figs. 4.10 and 4.11 C). The diffusion coefficients calculated with this combined model were of the same range as coefficients determined in pure diffusion calculations. Also the dissociation constants were similar to that obtained from the reaction dominated case (Table 4.7). Recovery due to diffusion dominated over the binding reactions. In euchromatin the diffusive fraction was nearly 2 – 3 times higher than the reactive fraction. In heterochromatin the ratio of the diffusion to the binding fraction was 1.7 : 1 for HP1α and 1 : 1 for HP1β. However, the diffusion coefficients were unrealistically small.

Because a lot of variable fitting parameters were implemented in the free fit model, another approach was pursued: In principle, the combined model was assumed to consist of a freely diffusive fraction and a binding fraction, therefore the diffusion coefficient was fixed to a value that was extracted from FCS experiments (see Chapter 4.4.2.). Free diffusion within cells was measured by FCS in the cytoplasm. Accordingly, D = 23 µm²/s for HP1α and D = 24 µm²/s for HP1β was fixed during fitting. This time, the measurement curves fitted badly to the combined model. The first slopes of measured values and fitted curves diverged; exemplary results are given in Table 4.8. The relatively high value of the diffusion coefficients strongly increased the binding fractions, in both chromatin regions and for both HP1 forms.

	HP1α		HP1β	
	euchromatin	heterochromatin	euchromatin	heterochromatin
$f_{unbleached}$	0.03 ± 0.03	0.04 ± 0.04	0.14 ± 0.10	0.03 ± 0.03
f_{diff}	0.71 ± 0.16	0.60 ± 0.27	0.58 ± 0.23	0.45 ± 0.23
D [$\mu m^2/s$]	0.24 ± 0.22	0.12 ± 0.09	0.19 ± 0.33	0.10 ± 0.11
f_{bind}	0.25 ± 0.16	0.36 ± 0.19	0.34 ± 0.16	0.46 ± 0.18
k_{off} [s^{-1}]	0.30 ± 0.15	0.12 ± 0.14	0.20 ± 0.09	0.12 ± 0.06
t_{res} [s]	4.2 ± 2.3	16.9 ± 13.7	6.2 ± 3.3	16.9 ± 21.6

Table 4.7: iFRAP analysis: Kinetic modeling of HP1 recovery applying the combined diffusion-reaction model. Just five exemplary curves were evaluated leaving all parameters variable. Noisy curves and low number of experiments resulted in high SD-values.

	HP1α		HP1β	
	euchromatin	heterochromatin	euchromatin	heterochromatin
$f_{unbleached}$	0.03 ± 0.04	0.03 ± 0.04	0.14 ± 0.10	0.03 ± 0.03
f_{diff}	0.23 ± 0.07	0.15 ± 0.12	0.16 ± 0.03	0.09 ± 0.06
D [$\mu m^2/s$]	23	23	24	24
f_{bind}	0.69 ± 0.09	0.69 ± 0.08	0.66 ± 0.04	0.72 ± 0.10
k_{off} [s^{-1}]	0.25 ± 0.10	0.13 ± 0.04	0.11 ± 0.02	0.11 ± 0.01
t_{res} [s]	4.3 ± 1.4	8.3 ± 2.6	9.5 ± 1.7	8.8 ± 1.0

Table 4.8: iFRAP analysis: Applying the combined diffusion-reaction model to HP1α and HP1β recovery curves with diffusion coefficients fixed to *D* of free diffusion within a cell determined by FCS. Interpretation of five intensity curves, values ± SD.

	HP1α		HP1β	
	euchromatin	heterochromatin	euchromatin	heterochromatin
$f_{unbleached}$	0.06 ± 0.06	0.02 ± 0.03	0.17 ± 0.11	0.02 ± 0.02
f_{diff}	0.44 ± 0.07	0.26 ± 0.16	0.34 ± 0.11	0.21 ± 0.08
D [$\mu m^2/s$]	1.37	1.37	0.92	0.92
f_{bind}	0.46 ± 0.08	0.63 ± 0.14	0.44 ± 0.12	0.62 ± 0.10
k_{off} [s^{-1}]	0.12 ± 0.06	0.11 ± 0.04	0.11 ± 0.02	0.10 ± 0.02
t_{res} [s]	7.8 ± 2.5	10.3 ± 2.8	9.9 ± 3.2	10.2 ± 2.3

Table 4.9: iFRAP analysis: Recovery of HP1 fitted to the combined diffusion-reaction model with the diffusion coefficient fixed to *D* estimated in sFRAP. This time all experiments were analyzed. Values ± SD.

However, a good fit was obtained when the effective diffusion coefficient, determined independently in sFRAP experiments ($D = 1.37\ \mu m^2/s$ for HP1α and $D = 0.92\ \mu m^2/s$ for HP1β), was used as a fixed parameter for curve fitting. Dissociation constants k_{off} ranging from 0.10 to 0.12 s^{-1} in euchromatin and heterochromatin were obtained. These values were of a comparable magnitude as those recovered from the binding dominated model. The diffusive and reactive fractions were of comparable sizes in euchromatin, in heterochromatin a 2.4 – 3-fold higher binding fraction was obtained. All data are listed in Table 4.9.

4.4. Fluorescence correlation spectroscopy

To further probe the dynamics and to resolve the full spectrum of GFP-HP1 mobility and interactions, fluorescence correlation spectroscopy was applied. As compared to FRAP, the measurements were done with higher sensitivity on a different spatial and temporal scale.

4.4.1. Calibration measurements and characterization of focal volume

A fluctuation analysis of the freely diffusing low molecular weight fluorophore Alexa 488 in solution (Fig. 4.12) was carried out regularly before each measurement session to be able to characterize the focal volume and to calculate absolute diffusion coefficients. As mentioned previously the calculated ACFs were fitted to a triplet state corrected, free diffusion model. From these fits, values of the number of molecules within the focus, *N*, the diffusion time τ_{diff} and the structural parameter κ were extracted (Table 4.10).

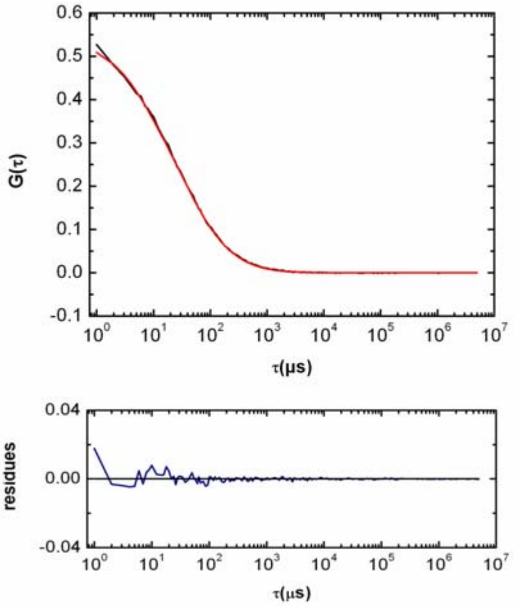

Figure 4.12: Autocorrelation function of Alexa 488 (black line) with fit curve (red line). Residuals are plotted below.

exp	N	τ_{diff} [µs]	κ
1	1.85 ± 0.003	33.0 ± 0.3	4.93 ± 0.17
2	2.18 ± 0.01	36.3 ± 1.3	4.78 ± 0.66
3	1.50 ± 0.004	30.6 ± 0.5	4.77 ± 0.27
4	1.86 ± 0.02	38.6 ± 0.6	3.96 ± 0.25

Table 4.10: Analysis of calibration measurements with Alexa 488 carried out at each day of the experiments. *N*, τ_{diff} and κ are averaged values of three up to ten single experiments. Errors are given as standard errors.

	averaged values
ω_0 [µm]	0.170 ± 0.009
z_0 [µm]	0.783 ± 0.056
V_{eff} [fl]	0.126 ± 0.013

Table 4.11: Parameters that characterize the focal volume of the CLSM used for FCS measurements. Errors correspond to SD.

These κ values were used for curve fitting of all experiments conducted on the corresponding day. By inserting the diffusion coefficient of Alexa 488, $D_{Alexa488} = (2{,}1 \pm 0{,}21)\cdot 10^{-6}$ cm²/s, and the measured diffusion times in Eq. 3.6, the lateral beam dimension ω_0 was determined.

With the structure parameter κ, extracted from the fits, also the axial beam dimension and the effective volume V_{eff} were computed. The values averaged over all sessions are shown in Table 4.11.

4.4.2. Mobility of HP1 in 3T3 cells

HP1 mobility and local concentrations were investigated in three distinct regions of the cell (Fig. 4.13). In the cytoplasm the ACF declined fastest. Thus, HP1 diffused fastest in cytoplasm and displayed a reduced mobility in chromatin regions. The inverse proportionality between the ACF amplitude and the protein concentration reveals that the lowest concentration of $1.7 \cdot 10^{-7}$ M was observed in the cytoplasm. Euchromatin and heterochromatin displayed 5 – 10-fold higher HP1 concentrations (Table 4.12). Theoretically a linear relationship exists between the ACF amplitudes and the concentration, but practically aberrations from this ideal behavior occur for very high or very low concentrations (Tewes, 1998). Therefore, protein concentrations were not calculated in reference to the known Alexa 488 standard concentrations, but according to Eq. 3.9 based on the effective volume.

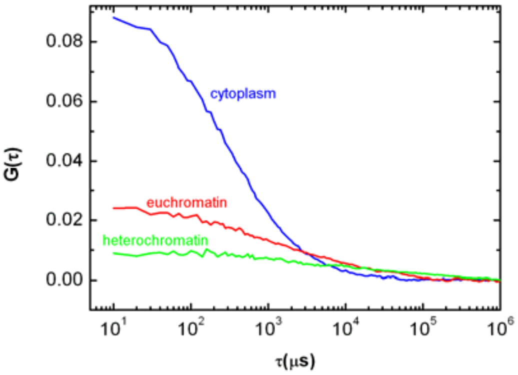

Figure 4.13: Comparison of ACFs measured in different cellular regions of HP1-GFP transfected cells.

HP1α	concentration [mol/l]
cytoplasm	$(1.7 \pm 0.5) \cdot 10^{-7}$
euchromatin	$(8.7 \pm 1.9) \cdot 10^{-7}$
heterochromatin	$(16.9 \pm 5.3) \cdot 10^{-7}$

HP1β	concentration [mol/l]
cytoplasm	$(4.8 \pm 3.2) \cdot 10^{-7}$
euchromatin	$(20.0 \pm 17.0) \cdot 10^{-7}$
heterochromatin	$(30.1 \pm 28.8) \cdot 10^{-7}$

Table 4.12: Local concentrations of HP1α (above) and HP1β (below). Values are calculated as an average of all analyzed curves in each region (± SD).

In *in vivo* measurements the effects of dark-states were not considered. At short correlations times the curves were too noisy to get reliable values for the triplet correction terms. Therefore the fraction of dark states was set to zero, which does not affect results significantly (Weidemann et al., 2003).

Measurements in cytoplasm

In the cytoplasm it was not possible to fit autocorrelation curves to a model describing free diffusion of one species. Therefore an anomalous diffusion model (Eq. 3.7, $f_1 = 1$) for a single species was applied (Fig. 4.14). Results showed an anomaly parameter α smaller than one that indicates obstructed (anomalous) diffusion. Diffusion times τ_{diff} through the focus were 315 and 335 µs for HP1α and HP1β, respectively. This corresponds to similar diffusion coefficients of 23 to 24 µm²/s for both HP1 isoforms (Table 4.13).

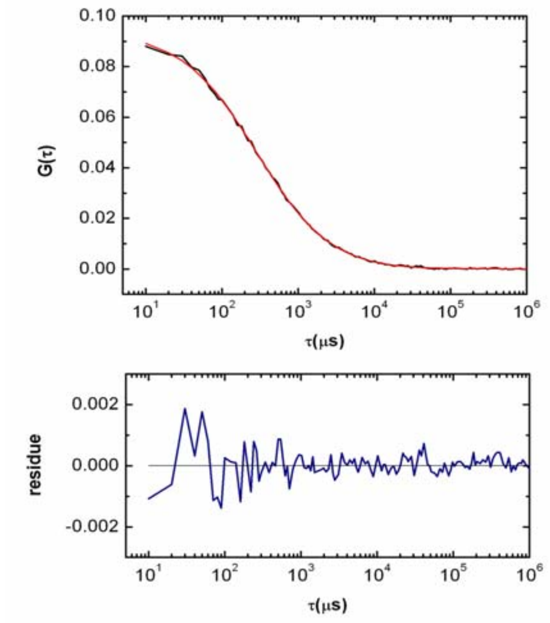

	HP1α	HP1β
N	14.2 ± 5.0	36.4± 24.6
τ_{diff} [µs]	315 ± 56	335 ± 118
α	0.83 ± 0.08	0.73 ± 0.09
D [µm²/s]	23 ± 4	24 ± 9

Table 4.13: Analysis of FCS measurements in cytoplasm. For HP1α altogether 11 measurements were analyzed, 10 curves were fitted for analysis of HP1β measurements (± SD).

Figure 4.14: Correlation curves of FCS conducted in cytoplasm of GFP-HP1α expressing 3T3 cells. Measured values were fitted to an anomalous diffusion model (red curve). Below the residue curve is shown. For HP1β analogous measurements were conducted.

Measurements in euchromatin

For the euchromatin measurements an anomalous diffusion model with two different species was applied (Fig. 4.15). Initially all fit parameters in Eq. 3.7 of both fractions were kept variable (‘fit 1’). In order to reduce fit-artifacts due to the high noise at short correlation times, the fit was repeated with fixation of $\tau_{diff,1}$ and α_1 to their averaged values obtained from the first fitting process (‘fit 2’). The results stayed in the same range, but the errors were reduced (compare Table 4.14).

For HP1α the first component consisted of 77 % of total HP1 amount and diffused in an anomalous way (α_1 = 0.81) through the focus within 973 µs. The second fraction moved significantly slower with a diffusion time of 45 ms. With an anomaly parameter $\alpha > 1$ the type of diffusion can be assumed as confined diffusion due to specific binding (Wachsmuth et al., 2003).

Therefore a third fitting approach was applied for ten exemplary curves, when all values for the first diffusive species were fixed (based on ‘fit 2’) and the second species was modeled with Eq. 2.29. This resulted in a bound fraction that moved directed due to chromatin diffusion with $\tau_{diff,2}$ = 41 ms through the focus (Table 4.14).

The diffusion coefficients were calculated from diffusion times based on calibration measurements (Eq. 3.8). The diffusion coefficient of the fast component of HP1α in euchromatin is $D_1 = 7.37 \pm 0.35$ µm²/s and the slower diffusive or bound fraction yielded $D_2 = 0.19 \pm 0.07$ µm²/s (Table 4.14).

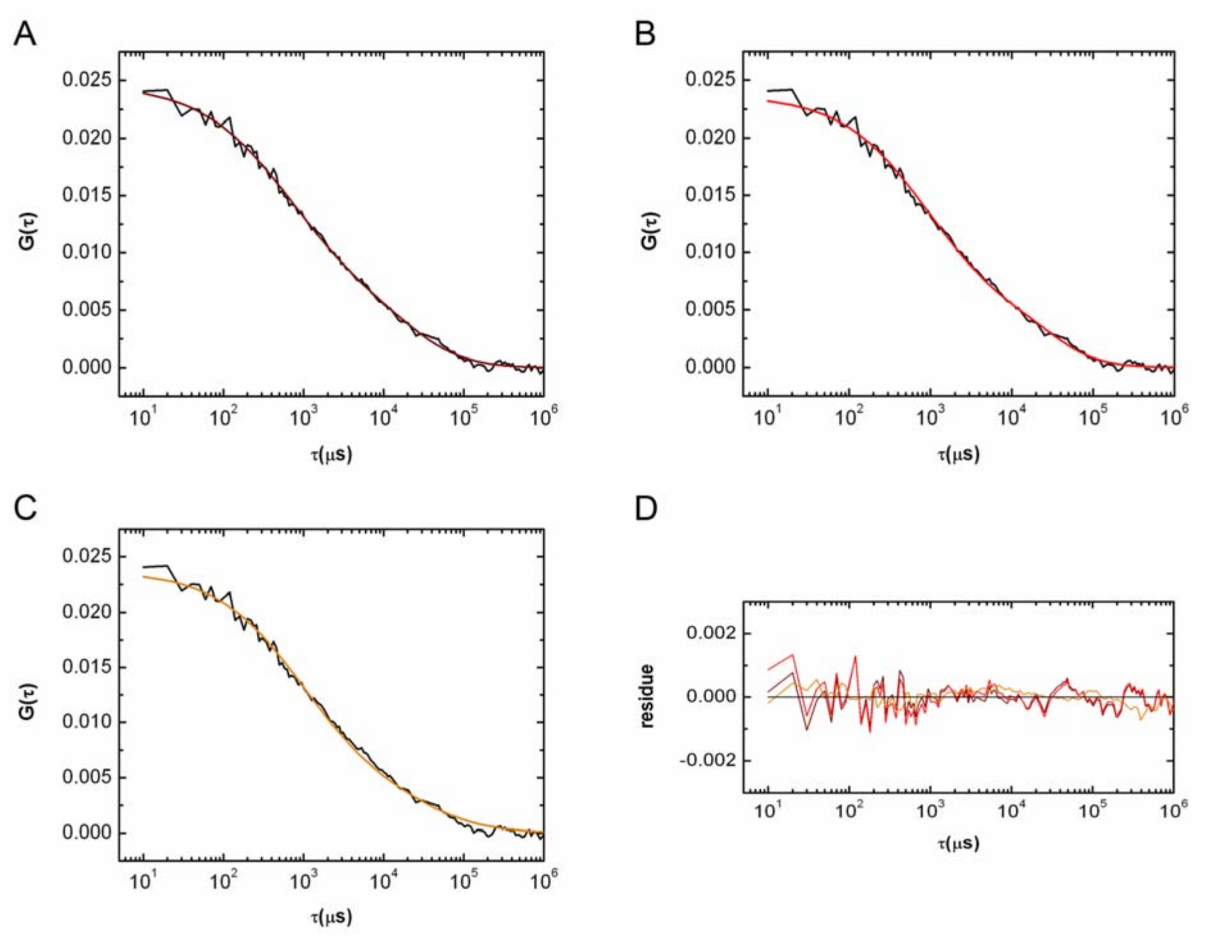

Figure 4.15: Autocorrelation curves of HP1α measured in euchromatin. The different fitting models are illustrated: **A** An anomalous diffusion model of two different species was applied first (‘fit 1’). **B** Later the first component was fixed to the mean values of ‘fit 1’, the second component was fitted freely. **C** Fitting the second component to a confined diffusion model was applied to test the possibility of HP1 movement bound to chromatin. **D** The residuals of all fits are shown, colors correspond to fit curves. HP1β analog.

	N	f1	$\tau_{diff,1}$ [ms]	α_1	$\tau_{diff,2}$ [ms]	α_2
Fit 1	65 ± 12	0.77 ± 0.07	0.97 ± 0.20	0.81 ± 0.08	45 ± 34	1.24 ± 0.23
Fit 2	69± 13	0.79 ± 0.06	0.97	0.81	43 ± 17	1.24 ± 0.23
	N	f1	$\tau_{diff,1}$	α_1	$\tau_{diff,2}$	η
Fit 3	69	0.79	0.97	0.81	41 ± 22	0.006 ± 0.010

	D_1 [µm²/s]	D_2 [µm²/s]
Fit 1	7.7 ± 1.6	0.21 ± 0.09
Fit 2	7.4 ± 0.4	0.19 ± 0.07
Fit 3	7.1 ± 0	0.20 ± 0.09

Table 4.14: Analysis of FCS measurements of HP1α in euchromatin. The number of molecules, *N*, the fractions *f* of each species together with its diffusion time τ and anomaly parameter α are listed. For 'fit 1' and 'fit 2' 19 measurements were analyzed, 'fit 3' was obtained from 10 data sets. Values without SD were fixed. The diffusion coefficients calculated from diffusion times are shown below. Although $\tau_{diff,1}$ was fixed in 'fit 2' and 'fit 3' *D* varies slightly because calculations based on daily calibration measurements.

	N	f1	$\tau_{diff,1}$ [ms]	α_1	$\tau_{diff,2}$ [ms]	α_2
Fit 1	152 ± 131	0.68 ± 0.11	3.4 ± 2.3	0.79 ± 0.14	142 ± 97	1.38 ± 0.31
Fit 2	156 ± 134	0.70 ± 0.13	3.4	0.79	142 ± 66	1.53 ± 0.41
	N	f1	$\tau_{diff,1}$	α_1	$\tau_{diff,2}$	η
Fit 3	152	0.68	3.4	0.79	125 ± 107	$(5.32 \pm 0.11)\ 10^{-6}$

	D_1 [µm²/s]	D_2 [µm²/s]
Fit 1	3.2 ± 1.9	0.08 ± 0.05
Fit 2	2.2 ± 0.2	0.06 ± 0.03
Fit 3	4.5 ± 1.8	0.10 ± 0.07

Table 4.15: Analysis of FCS measurements in euchromatin of HP1β. All values extracted from the different fits were listed. Again in 'fits 1 and 2' 19 curves were analyzed, in 'fit 3' just 10 curves were evaluated.

The same type of data analysis was conducted for HP1β in euchromatin (Table 4.15). A totally free fit revealed a fast component of about 68 % with an average diffusion time of 3.4 ms. This component showed anomalous diffusion with an anomaly parameter of α_1 = 0.79. The second fraction displayed a diffusion time of 142 ms. Again an $\alpha_2 > 1$ was obtained and therefore the third fitting procedure was applied. 'Fit 2' brought no improvement with respect to the totally free fit ('fit 1'). Therefore in 'fit 3' values of the first component were fixed to values obtained in 'fit 1'. Diffusion coefficients of HP1β were somewhat smaller than that of HP1α. The faster component had D_1 = 3.2 ± 1.9 µm²/s and the second fraction D_2 = 0.08 ± 0.05 µm²/s.

Measurements in heterochromatin

For measurements in heterochromatin initially a free fit with all parameters of both species varying was applied (Fig. 4.16 A). For HP1α a relatively fast species, comprising 55 % of the protein and a diffusion coefficient of $D_1 = 3.9 \pm 1.4$ µm²/s was observed. In contrast to that, the second species diffuses very slowly with $\tau_{diff,2}$ = 223 ms and $D_2 = 0.05 \pm 0.04$ µm²/s (Table 4.16).

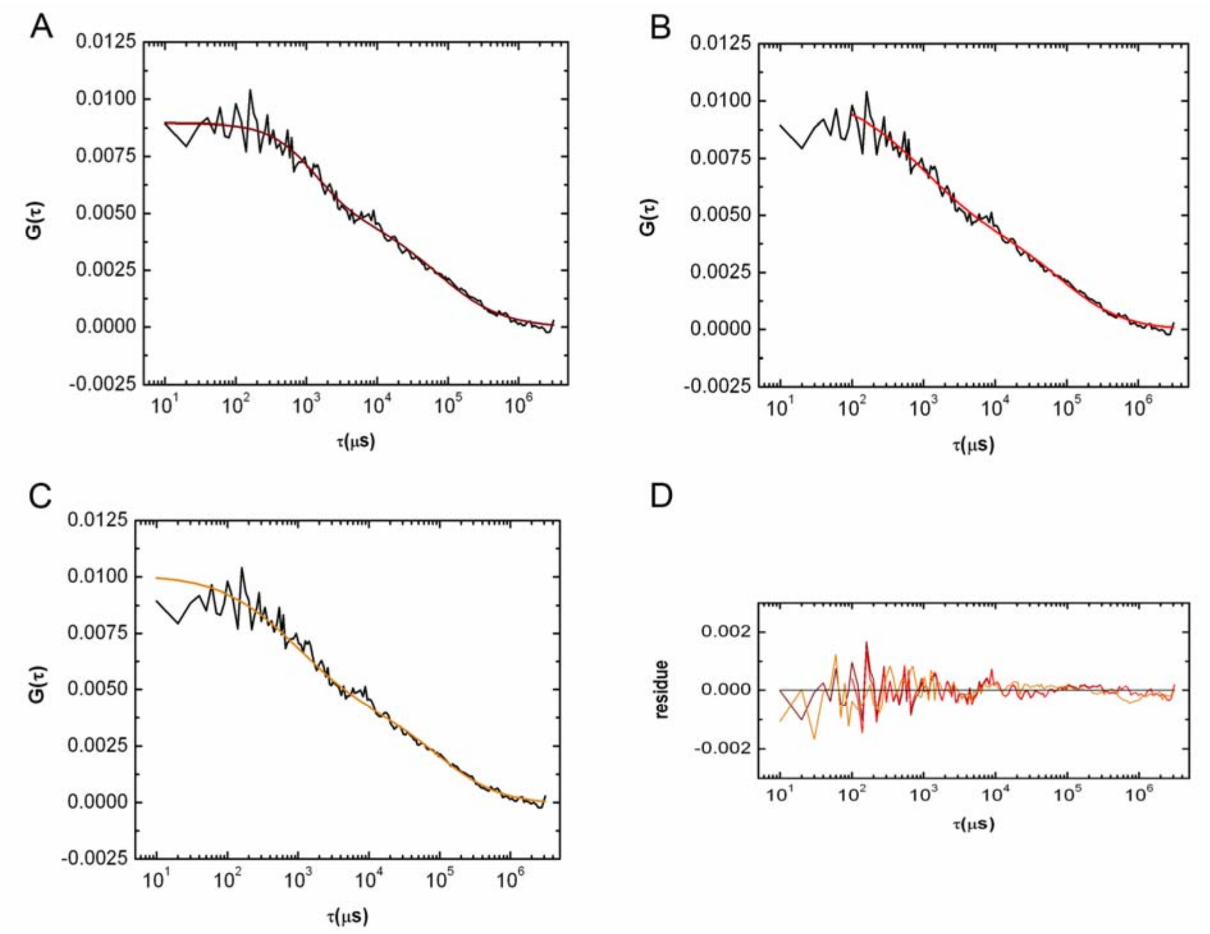

Figure 4.16: Autocorrelation curves of HP1α mobility in heterochromatin. **A** Anomalous diffusion model of two species. **B** Two-component, anomalous diffusion fit assuming a uniform fast species in all nuclear regions, i.e. parameters of the first component were fixed to euchromatic values. **C** Fit with one component matched to an unitary fast component within the nucleus and a second component moving bound to chromatin. **D** Residuals of all fits.

The significant noise at the first milliseconds of the ACF curves could introduce errors to the fit, also for larger diffusion times. Therefore, based on the assumption that the nucleus hosts one mobile species that follows the same kinetics in all chromatic regions - in euchromatin as well as in heterochromatin - in 'fit 2' all parameters for the first species were fixed to the diffusion time and anomaly parameter value obtained for the fast species in euchromatin. With this conditions for HP1α reliable fits were obtained (Fig. 4.16 B) and diffusion times of the second species were lowered (Table 4.16). The diffusion coefficient of the second species increased to $D_2 = 0.07 \pm 0.05$ µm²/s.

Even in heterochromatin the third approach used a model in which the second species was chromatin bound (Fig. 4.16 C). Again the first component was fixed to euchromatin values. Following this model the bound fraction would move with a diffusion coefficient of $D_2 = 0.04 \pm 0.02$ µm²/s.

	N	f1	$\tau_{diff,1}$ [ms]	α_1	$\tau_{diff,2}$ [ms]	α_2
Fit 1	144 ± 37	0.55 ± 0.06	2.1 ± 0.9	0.88 ± 0.12	223 ± 111	1.56 ± 0.26
Fit 2	126 ± 41	0.58 ± 0.08	0.97	0.81	163 ± 106	1.33 ± 0.26
	N	f1	$\tau_{diff,1}$ [ms]	α_1	$\tau_{diff,2}$ [ms]	η
Fit 3	145 ± 38	0.56 ± 0.05	0.97	0.81	221 ± 164	0.12 ± 0.34

	D_1 [µm²/s]	D_2 [µm²/s]
Fit 1	3.9 ± 1.4	0.05 ± 0.04
Fit 2	7.5 ± 0.4	0.07 ± 0.05
Fit 3	7.2 ± 0.2	0.04 ± 0.02

Table 4.16: Analysis of FCS measurements of HP1α in heterochromatin. Molecule number, N, fractions f of fast and slow species, diffusion times, τ_{diff}, and anomaly parameters, α, of HP1α were gained from different kinetic models. Applying 'fit 1' ten curves gave reliable values, in 'fit 2' totally 18 curves were fitted and 'fit 3' was analyzed exemplarily, i.e. 10 curves were evaluated. Diffusion coefficients vary largely depending on the applied model.

	N	f1	$\tau_{diff,1}$ [ms]	α_1	$\tau_{diff,2}$ [ms]	α_2
Fit 1	214 ± 187	0.59 ± 0.09	2.2 ± 0.8	0.83 ± 0.14	205 ± 76	1.66 ± 0.29
Fit 2	230 ± 188	0.63 ± 0.08	3.4	0.79	234 ± 74	1.85 ± 0.29
	N	f1	$\tau_{diff,1}$ [ms]	α_1	$\tau_{diff,2}$ [ms]	η
Fit 3	146 ± 67	0.59 ± 0.09	2.1 ± 0.5	0.85 ± 0.14	200 ± 78	0.0001 ± 0.0004

	D_1 [µm²/s]	D_2 [µm²/s]
Fit 1	3.7 ± 1.1	0.04 ± 0.02
Fit 2	2.2 ± 0.2	0.03 ± 0.01
Fit 3	3.7 ± 0.9	0.04 ± 0.02

Table 4.17: Analysis of FCS measurements of HP1β in heterochromatin. In all three fitting models at least 10 to maximum 12 curves were analyzed. All fitting models revealed similar diffusion coefficients.

For HP1β the same approach was used. However, this time the free fit revealed a 60 % fast component that seemed to diffuse even faster in heterochromatin than in euchromatin. The possibility of observing a fit artifact was again tested in 'fit 2', therefore, the values of species 1 were fixed to values measured for the fast species in euchromatic. But this time no

improvement was achieved for the fits and diffusion time as well as anomaly parameter of species two were even enlarged.
In testing the binding option ('fit 3'), applying the first species' values of 'fit 2' failed. For this reason, data were extracted from 'fit 1' and inserted in the mathematical model of 'fit 3'. This confirmed the results obtained from the free fit and resulted in the same diffusion coefficients even for the second, bound fraction (Table 4.17).

For HP1α the diffusion coefficients of the fast species could be assumed to be equal in all nuclear regions, *D* of the slower species differed between euchromatin and heterochromatin (Tables 4.14, 4.16). The fraction of fast proteins was reduced from 77 % in euchromatin to 55 % in heterochromatin. HP1β seemed to be more continuous in its diffusion behavior, in euchromatin and heterochromatin the diffusion coefficients of both species were in the same range (Tables 4.15, 4.17). Here, the fast fraction was reduced in heterochromatin only by 10 %.

4.4.3. Mobility behavior of LSD1 in 3T3 cells

FCS measurements of another putative heterochromatin component, the histone demethylase LSD1, were carried out in mouse fibroblasts transfected with either full length human LSD1 (hLSD1) protein or murine LSD1 lacking the first 50 amino acids (mLSD1). Again autocorrelation curves were evaluated to determine diffusion times and local concentrations of LSD1 distribution within the cell.

	concentration [mol/l]
cytoplasm	$(2.6 \pm 2.2)\cdot10^{-7}$
euchromatin	$(23.1 \pm 10.9)\cdot10^{-7}$
heterochromatin	$(20.6 \pm 11.2)\cdot10^{-7}$

Table 4.18: Concentrations of hLSD1 calculated from the amplitude of the ACF. Local concentrations of all cellular regions were determined from exemplary measurements (3 to a maximum of 8 measurements).

	concentration [mol/l]
cytoplasm	$1.6\cdot10^{-7}$
euchromatin	$(8.6 \pm 1.1)\cdot10^{-7}$
heterochromatin	$(7.7 \pm 2.1)\cdot10^{-7}$

Table 4.19: Concentrations of the murine protein LSD1 calculated from the ACF amplitudes. In cytoplasm only one successful measurement was obtained, therefore no SD could be estimated; three curves were analyzed for the other regions.

Concentrations in the cytoplasm were low as expected for a nuclear protein. In euchromatin and heterochromatin ~10-fold (hLSD1) and ~5-fold (mLSD1) concentrations were measured (Tables 4.18 and 4.19).

FCS measurements of hLSD1

The ACF curves measured in cytoplasm were fitted with an anomalous diffusion model for a single species (Eq. 3.7, $f_1 = 1$). From three measurements α was calculated as 0.73 ± 0.03 for hLSD1 and the diffusion coefficient was calculated using the Alexa 488 measurements to $D = 9.8 \pm 3.4$ µm²/s, (Table 4.20).

In euchromatin the measured values were fitted to a two-component anomalous diffusion model (Eq. 3.7). A freely diffusive species and a second bound species – or at least transiently binding component – of the demethylase were expected. However, fitting procedure revealed just one component with 1.2 ms and a diffusion coefficient of $D = 6.63 \pm 1.74$ µm²/s with the anomalous diffusion parameter $\alpha = 0.75 \pm 0.07$.

Also for heterochromatin measurements most data were consistent with a one-component anomalous diffusion model. In heterochromatin a diffusion coefficient of $D = 4.5 \pm 2.6$ µm²/s was determined. Except two measurements out of ten showed the existence of a second component (40 %) with strongly reduced diffusion ($D = 0.13 \pm 0.02$ µm²/s) (Table 4.20).

	N	$\tau_{diff,1}$ [ms]	α_1	D [µm²/s]
cytoplasm	20 ± 17	0.8 ± 0.2	0.73 ± 0.03	9.8 ± 3.4
euchromatin	176 ± 83	1.2 ± 0.3	0.75 ± 0.07	6.6 ± 1.7
heterochromatin	156 ± 85	2.7 ± 2.4	0.66 ± 0.06	4.5 ± 2.6

Table 4.20: Analysis of FCS measurements in 3T3 cells transiently transfected with human (GFP-)LSD1. All regions revealed one component that diffused anomalously and decelerated in dense chromatin regions. One-fifth of correlation curves, gained in heterochromatin, showed the existence of a second species, comprising 40 % of all LSD1-protein with a diffusion coefficient of $D = 0.13 \pm 0.02$ µm²/s.

FCS measurements of mLSD1

The murine sequence of LSD1 was transferred to 3T3 cells, and measurements in all three cellular regions were conducted. In cytoplasm and euchromatin just one diffusive species was identified following an anomalous diffusion model in both regions. Diffusion coefficients were very similar: In the cytoplasm $D = 7.0$ µm²/s and for euchromatin $D = 7.2 \pm 1.07$ µm²/s were determined. Thus, it seems that a fast species can be found everywhere in the cell. This prediction was affirmed when the diffusion coefficient of the fast component in heterochromatin was calculated to be $D = 6.8 \pm 1.4$ µm²/s, yet two species were found in heterochromatin domains. The second slowly moving species (about 20 %) had a diffusion coefficient of $D = 0.2 \pm 0.02$ µm²/s. Measured and averaged values are listed in Table 4.21.

	N	f_1	$\tau_{diff,1}$ [ms]	α_1	$\tau_{diff,2}$ [µs]	α_2
cytoplasm	12	1	1.2	0.74	-	-
euchromatin	65 ± 8	1	1.2 ± 0.2	0.85 ± 0.11	-	-
heterochromatin	58 ± 16	0.79 ± 0.19	1.2 ± 0.3	0.72 ± 0.01	33 ± 29	1.54 ± 0.47

	D_1 [µm²/s]	D_2 [µm²/s]
cytoplasm	7.0	-
euchromatin	7.2 ± 1.1	-
heterochromatin	6.8 ± 1.4	0.2 ± 0.02

Table 4.21: FCS analysis of mLSD1 in cytoplasm, euchromatin and heterochromatin. A single component was discovered in cytoplasm and euchromatin, heterochromatin seemed to house two species. The diffusion coefficients of the fast species were similar within different regions, this indicates the theory of an unitary fast component even in the whole cell. The second species was extremely decelerated.

5. Discussion

Fluorescence microscopy as a non-invasive method is an excellent approach to study the structure and dynamics of cellular processes. During the last years large advancements have been made in this field: Microscopy techniques emerged that overcome the diffraction limit. Also in fluorescence microscopy nanoscale resolution can be obtained applying different physical concepts and further research was done to adopt this high resolution methods to living organisms (Bornfleth et al., 1998; Hell, 2007; Hell, 2003; Reymann et al., 2008). Furthermore, the possibilities of high resolution microscopy were extended from imaging to analytical, temporally resolved measurements (Day, 2005). In this way, the dynamics of living cells can be studied. The implementation of diverse methods for mobility measurements and the theoretical description are active fields of current research in physics and biology. But often one method is not sufficient to cover the complete spectrum of mobility of a molecule within a complex environment like in a cell or the cell nucleus. Therefore different methods need to be combined in order to validate and to complement each other for a quantitative description of biological systems.

The intention of this work was to develop an approach based on FRAP and FCS mobility measurements and to figure out the best methods of data analysis for both methods, to be able to receive a complete model of cellular dynamics. The elaborated measurement and analysis methods were applied on the multifunctional heterochromatin protein 1. HP1 has been described as a heterochromatin protein that binds statically to chromatin and works as a ‘glue’ of the highly condensed structure. But recent research opens up new perspectives on HP1 as it is also involved in processes in euchromatin and seems to be highly mobile in the cell nucleus. Recently, the model of HP1 as a static component of chromatin was refuted manifoldly, but an exact analysis of HP1 kinetics – as it was applied in this work – was neglected so far.

5.1. Optimization of data analysis for FRAP and FCS

The original evaluation of fluorescence recovery after photobleaching measurements consists only in extracting the fractions of immobile or mobile protein molecules and the half-time of recovery by direct readout from the recovery curve (Rabut and Ellenberg, 2005). The problem with this kind of analysis is, that especially $t_{½}$ is highly dependent on measurement conditions, like the size of the ROI, and therefore measurements carried out under different conditions are not comparable. In addition, the contribution of binding could be estimated only in comparison to an inert freely diffusing molecule. Within the last years mathematical models were developed that considered both diffusion and binding, but some assumptions had to be made (e.g. ignoring either diffusion or binding as a limiting case, neglecting the finite cell volume, boundary effects and assuming simple diffusion etc.). Currently, more refined FRAP models are being developed to overcome these limitations.

Even in this work at first the limiting cases, i.e. pure diffusion or diffusion-uncoupled, binding models, were evaluated. However, they either resulted in unrealistic diffusion coefficients or in large deviation of fit and experimental data. Accordingly, a linear superposition of diffusion and binding-reaction equations was applied. This implies that both processes happen on different time scales, i.e. either diffusion is much faster than binding reaction or vice versa. If this assumption cannot be made, more complex descriptions have to be used (McNally, 2008; Sprague et al., 2004). These are directly derived from reaction-diffusion differential equations. No analytical expression for FRAP can be calculated, but applying a Laplace transform an equation that can be fitted to the recovery curves can be obtained. Retransformation reveals the parameters for reaction and diffusion (k_{on}, k_{off}, D) from this ‘full model’. However, this method is computationally elaborate. The model developed by Beaudouin and colleagues is based on a different analysis approach (Beaudouin et al., 2006). However, it seems not to be suitable for the analysis of small measurement regions as required in the present study.

The analysis of FRAP after bleaching a strip-ROI – as described in literature – is done mainly by analyzing again the averaged intensity of the whole strip as explained for iFRAP, e.g. by (Schmiedeberg et al., 2004). In contrast, the analysis of the spatial information after bleaching a strip-shaped ROI, like it was done in this work, was rarely applied.

A similar development of mathematical models for the analysis of fluorescence correlation spectroscopy and application of different models in fitting the ACF-curves can be observed. The interpretation of measurements must be done in consideration of the different models: Intracellular data are normally fit to either a multiple diffusion coefficient model based on simple (free) diffusion or to an anomalous diffusion model (Kim et al., 2007). Here, the fitting of measurements to the anomalous diffusion model of one or two species was applied, where smaller values of the anomaly parameter α correspond to either increased ‘stickiness’ or higher concentrations of adhesive obstacles. Whereas the first species always followed anomalous diffusion with $\alpha < 1$, the model was improved for the second species that showed an $\alpha > 1$. The primary interpretation of $\alpha > 1$ as directed movement is inappropriately in the system studied. Alternatively, it can be explained by binding to big molecules or polymers that move slowly and spatially restricted and in fits with anomalous diffusion model this behavior results in an α larger than one (Wachsmuth, 2001). Therefore the fit formula was adjusted for a bound fraction. Results obtained with this model were in good agreement with the experimental data.

5.2. Combination of the complementary methods

For measurements of mobility and binding-interactions various techniques were developed and are currently further advanced. Photobleaching experiments can be designed depending on what information is of interest by varying the size of the bleached region or the number of bleaches and even on how fluorescence relaxation or redistribution is analyzed. Repetitive bleaching and imaging simultaneously is done in FLIP (fluorescence loss in photobleaching) or CP (continuous photobleaching) experiments. FLIP measurements can be done at the same optical setup as FRAP, but with a different data analysis. In contrast, CP is carried out with a laser beam parked at one position, similar to FCS.

Here, two techniques for mobility measurements, FRAP and FCS, were combined in order to take the advantages of both methods. Measurement of intensity fluctuations can yield properties of molecular systems that are inaccessible to photobleaching methods and vice versa. FRAP requires a systems with relatively high dye concentrations, and therefore struggles less with autofluorescence and background. Thus, it is applicable within cells/nuclei with normal to high protein expression levels. In opposite, FCS requires low concentrations (1 nM – 1 μM) to obtain good results. This increased sensitivity is favorable for measurements in regions with low signal. This fact was used to do measurements in cytoplasm, where nuclear proteins are synthesized and diffuse freely but in such low concentrations that they are not detectable for FRAP. Furthermore, the high temporal resolution in FCS allows to analyze processes in μs – s time range and is therefore ideally suited to observe fast diffusion processes. However, a disadvantage of FCS is, that the method cannot be used with immobilized molecules, i.e. bound or hindered molecules with a diffusion coefficient smaller than 0.01 µm²/s. In this case the fluorophores of the immobilized molecules simply get bleached and do not contribute to the fluctuations measured by FCS. This gap can be filled by FRAP, that allows the distinction of mobile and immobile fractions with a temporal resolution currently limited to the 0.1 – 1 s range. Thus, FRAP is much more suited for slow diffusion processes. Depending on the cellular regions in which mobility is measured, FCS can be precisely located to very small compartments, whereas FRAP needs a larger area to get recovery curves with an acceptable noise level. As demonstrated in this thesis, both methods complement each other perfectly.

Apart from the fact that FRAP and FCS cover distinct cellular regions and different fast or slow processes, one has to consider that FRAP and FCS as well as the different FRAP methods (iFRAP and sFRAP) are based on differently sized measurement ranges and different time scales (Fig. 5.1). This diversity influences the results for the diffusion behavior, e.g. when obstacles decelerate the diffusion in a large observation volume but become irrelevant for diffusion on smaller observation scales. Furthermore, the conditions within the cell require a detailed consideration with anomalous diffusion model as was seen by FCS, nevertheless FRAP analysis based on simple diffusion. In this case diffusion coefficients, that are proportional to the slope in a *MSD* vs. time plot, can vary in a small range (illustrated in Fig. 5.1).

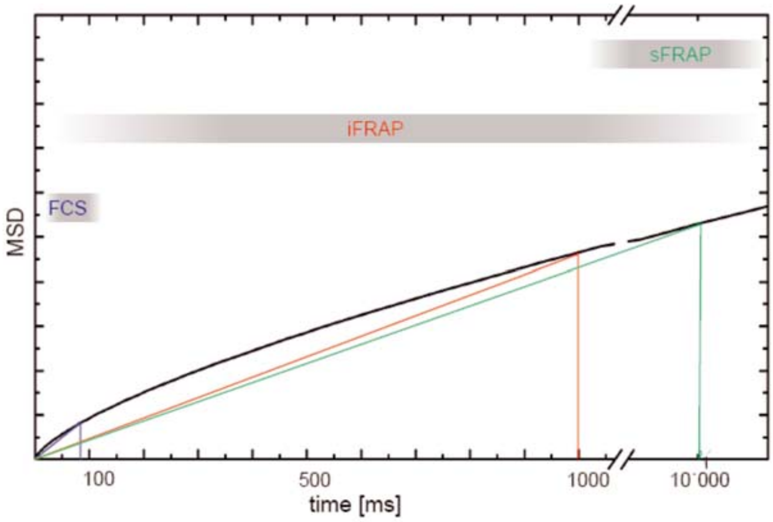

Figure 5.1: Time scales of FCS and FRAP and comparison of anomalous and simple (free) diffusion. FCS measurements resolve mobility in a µs to 100 ms time scale, photobleaching methods cover the ms to s range. In the case of anomalous diffusion the dependency of MSD from time follows a t^{α}-law (black curve). When FRAP measurements are evaluated applying only simple diffusion model, which postulates a linear MSD-time dependency (blue, red and green lines), a difference in calculated apparent diffusion coefficients can occur.

5.3. FRAP and FCS fluctuation studies on heterochromatin protein 1

FRAP and FCS were implemented on the prominent heterochromatin protein 1 (HP1). Heterochromatin is densely packed, thus, the accessibility for enzymes, transcription machinery and gene activators, etc. is stably repressed. Therefore, it was assumed that interaction of chromatin and its stabilizer HP1 is highly static. However, the first photobleaching experiments with HP1 showed that HP1 is highly mobile and its involvement in heterochromatin must follow a different mechanism (Cheutin et al., 2003; Festenstein et al., 2003; Schmiedeberg et al., 2004).

The two different isoforms, HP1α and HP1β, that are localized in heterochromatin, were investigated in this work. Both behave similar and colocalize within murine cells during interphase. It was proposed that the distribution of both isoforms together reflects the species-specific heterochromatin organization (Minc et al., 1999). A difference in functionality is not known and results obtained here for the dynamics of these proteins support this similarity, since results of both HP1 isoforms did not show significant differences. FRAP resulted in slightly decreased diffusion coefficients and somewhat higher immobile fraction of HP1β as compared to HP1α. FCS results for both types were similar in the cytoplasm and heterochromatin. Only in euchromatin the diffusion of HP1β was threefold decelerated and the slower fraction was slightly larger than that of HP1α.

5.3.1. Translating FRAP data into macromolecule dynamics

First the diffusion coefficient of HP1α in the nucleus was determined globally by sFRAP to a value of $D = 1.4 \pm 0.3\ \mu m^2/s$. The magnitude of the diffusion coefficient is very small compared to freely diffusing HP1-dimers within cells, either calculated with HYDROPRO (19.6 – 17.4 $\mu m^2/s$, depending on GFP-labels), measured in vitro by S. Kaltofen using ultra centrifugation (22.6 $\mu m^2/s$) or based on the D-value measured with FCS in cytoplasm (23 $\mu m^2/s$). A smaller diffusion coefficient can be caused by complexation, but even for a large complex this value is too small. Calculating the molecular weight of a hypothetic complex that diffuses freely within the nucleoplasm with $D = 1.4 \pm 0.3\ \mu m^2/s$ yields the mass of 1400 MDa. But, on the one hand eu- and heterochromatin behavior is mixed up within such a big ROI, on the other hand transient binding interactions of HP1 to chromatin, formation of complexes that can interact with DNA or chromatin and collisions with other molecules are included in the apparent *D*-value obtained in sFRAP evaluation.

In iFRAP a first simple analysis was applied analogous to other groups who already measured FRAP of GFP-tagged HP1 (Cheutin et al., 2003; Festenstein et al., 2003; Schmiedeberg et al., 2004). Consistent with their results, iFRAP revealed that HP1 proteins are highly dynamic within the nucleoplasm, even in heterochromatin. In euchromatin the recovery was 1.6 – 1.7-times faster than in heterochromatin (derived from the half time of recovery). This value is at the lower limit as compared to previous results. Consistent with former publications in both euchromatin and heterochromatin an immobile fraction of HP1 was found, that remained stably attached to chromatin, at least for 60 seconds, i.e. the duration of the experiment (compare also (Dialynas et al., 2007)). These immobile fractions, 5 % in euchromatin and 10 – 14 % in heterochromatin, must exhibit a dissociation rate constant smaller than k_{off} = 0.02 s^{-1}.

A further analysis by fitting the data to a mathematical model was done only by L. Schmiedeberg and colleagues, who applied a (exponential) model with two different fractions (Schmiedeberg et al., 2004). For both euchromatin and heterochromatin they found two different mobility states, a highly mobile one (euchr. 80 %, heterochr. 50 %) and a second low mobility fraction that was assumed to belong to a multi-protein-complex (euchr. 20 %, heterochr. 40 %). However, recent findings show that a double exponential model, like that one applied by them, fits virtually any iFRAP curve (McNally, 2008).

As mentioned in Chapter 4.3. the approach used here to fit the data to a pure diffusion model was discarded because the resulting diffusion coefficients were only consistent with complexes of $(2.4 – 65.4)\cdot 10^5$ MDa. The simple binding model was excluded also because of poor fits. Therefore a two component model was developed, namely a combination of diffusion and binding-reaction. Applying the diffusion coefficient obtained from sFRAP in the fitting procedure, 34 – 44 % of HP1 molecules belonged to the diffusive fraction in euchromatin and in heterochromatin only 21 – 26 %. The percentage of molecules experiencing transient binding raised from about 46 % in euchromatin to 63 % in heterochromatin. Although binding fractions were higher in heterochromatin, the dissociation constants in eu- and heterochromatin were similar with values of $0.12 \pm 0.06\ s^{-1}$ and $0.11 \pm 0.04\ s^{-1}$ respectively, corresponding to residence times of 7.8 ± 2.5 s and 10.3 ± 2.8 s.

In summary, fluorescence recovery after photobleaching revealed that HP1 is subdivided into three fractions. The amount of immobile and transiently bound fractions increased with the chromatin condensation level. This can be linked to an at least twofold higher density of binding sites in heterochromatin, as was shown by the image analysis of chromatin density and a higher methylation level in heterochromatin. However, the binding stability for heterochromatin and euchromatin in terms of the residence time ($1/k_{off}$) was very similar.

5.3.2. Completion of the kinetic model by FCS data

To estimate the whole range of dynamics the mobility of HP1 was also measured in the cytoplasm, where the protein is synthesized. A diffusion coefficient of 23 ± 4 µm²/s was measured and is in good agreement with published data (D = 26 ± 2 µm²/s, (Schmiedeberg et al., 2004)) and calculated values of 19.6 µm²/s for a GFP-tagged HP1-dimer.

In euchromatin FCS measurements revealed at least two populations of HP1α with different mobility. The major fraction, i.e. about 80 %, was still highly mobile with $D = 7.4 \pm 0.4$ µm²/s, whereas the residual 20 % moved much slower with a diffusion coefficient of $D = 0.2 \pm 0.1$ µm²/s. Normally, for a freely diffusive species within the nucleoplasm a diffusion coefficient similar to that observed in cytoplasm should be expected, because both compartments exhibit the same viscosity (Pack et al., 2006). Therefore in euchromatin the fast component must be regarded as a diffusive species that gets retarded either by complexation or by transient binding due to ‘stickiness’. The ‘stickiness’ describes the unspecific and low affinity binding to DNA, chromatin or protein-complexes, or to different other obstacles.

The second species diffuses that slow, that only the movement of a very large complex of HP1s, also comprising other proteins, that bind specifically to chromatin can explain this slow diffusion. This model was proposed by (Schmiedeberg et al., 2004). Alternatively, the HP1 molecules that also fulfill functions in euchromatin, can be bound to chromatin structures that show spatially confined and very slow movement. Such a chromatin structure could be a ~100 kb chromatin loop as described in the MLS model (Cremer and Cremer, 2001) carrying some HP1s and associated proteins (Fig. 5.2). No bright events were observed in the FCS raw data, that can give a hint on clustering of several HP1s, and again such a complex must be inconceivable large. Therefore the second interpretation – HP1 bound to large chromatin structures – is preferred and confirmed by fitting the confined 'chromatin bound diffusion'-model.

The only diffusion coefficient of HP1 obtained by FCS, as published by Schmiedeberg and colleagues ($D = 0.6 \pm 0.03$ µm²/s), was calculated as a single species coefficient in euchromatin. A second species was just observed in the raw data as 'bright events' but was not further analyzed. Therefore the estimated diffusion coefficient must be regarded as an apparent or effective diffusion coefficient.

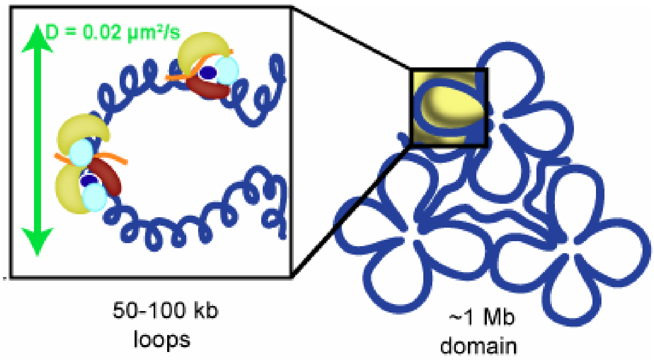

Figure 5.2.: Schematic illustration of the confined mobility of bound HP1s (yellow half moon). The second species of HP1 found in FCS measurements was assumed to bind to a 100 kb chromatin loop and its movement is connected to the motion of the whole loop.

Diffusion coefficients estimated for HP1β in euchromatin are just half times that of HP1α given above, here, 70 % belong to the fast species and 30 % to the bound fraction. Perhaps this can be a hint that this isoform is higher involved in euchromatic processes.

Also the FCS measurements in heterochromatin yielded two species. The fast species observed in heterochromatin is assumed to behave like the fast species in euchromatin, moving with the same diffusion coefficient of $D = 7.4$ µm²/s. The second, slower species of heterochromatic HP1 is also assumed to be bound to chromatin-loops. However, in comparison to euchromatin the diffusion of the bound species in heterochromatin is a factor ten slower than the bound species in euchromatin. This was assumed to depend on the higher packed structure and more confined movement as well as possibly more complex structures that are formed in heterochromatin, involved in heterochromatin spreading and maintenance. As seen in iFRAP measurements, in heterochromatin the part of the slower fractions increased. In FCS measurements the 'bound' fraction doubled to a value of 42 %, whereas the fast species in heterochromatin consisted of 58 %.

5.4. Kinetic model of HP1

Combining both FRAP and FCS yielded a model of three species of HP1 in euchromatin and heterochromatin and a single freely diffusive HP1 species in the cytoplasm (Fig. 5.3). Whereas in iFRAP the three distinct fractions can be 'seen' directly as a highly mobile, a transiently binding and an immobile fraction, in FCS only two species are distinguishable, namely the highly diffusive and a slower, chromatin bound fraction. Because of bleaching during data acquisition in FCS the bound and transiently bound molecules are normally not observable. However, in this case they were detected because of their movement in association to a diffusing polymer, probably the ~100 kb chromatin-loop (Fig. 5.2). But the inherent species of transiently and stably bound are not distinguishable and both account to the ACF as one single species, diffusing with a very small diffusion coefficient.

The analysis showed a free and unrestricted exchange of HP1 between euchromatin and heterochromatin, as all nuclear regions exhibit equal species of HP1 (compare also (Schmiedeberg et al., 2004)). This fact was also relevant for iFRAP experiments when a complete heterochromatin focus was bleached and nevertheless recovery was observable. Accordingly, the mobile species diffuses throughout the whole nucleoplasm in a decelerated manner (compared to cytoplasm) because of unspecific interactions ('stickiness') with chromatin or with its proposed interaction partners like H1, H3K9me and Suv39h1 or isolated nucleosomes at histone cores (Fig. 5.3, eu1 and het1).

Possible interactions of transiently binding and immobile species in euchromatin and heterochromatin are illustrated in Fig. 5.3, too. In heterochromatin multiple interaction partners for HP1 have been proposed (Hiragami and Festenstein, 2005; Maison and Almouzni, 2004). Thus, HP1 binding is mediated via its low affinity interaction with H3K9me3, the core globular domain of H3, the linker histone H1, a ncRNA and a number of HP1 associated proteins, like the histone methylase Suv39h1. Within this interaction network binding affinity increases and HP1 is stably bound ($k_{off} \leq 0.02\ s^{-1}$). The fraction of HP1 that binds transiently in heterochromatic regions is supposed to a reduced set of interaction partners, probably in different combinations (Fig. 5.3, het2). This type of moderate affinity is assumed to occur within less dense regions of the heterochromatin. This intrinsic heterogeneity of heterochromatin density is not resolved with the resolution of the CLSM (Görisch et al., 2005).

In euchromatin the same species were found, binding with similar stability (i.e. similar k_{off}) to its targets, just the targets itself and the amount of targets vary slightly. This time, 'stable HP1' is assumed to bind preferably to dimethylated H3K9, Suv39h1, that was also found in euchromatin, and other euchromatic HMTases, H1, the histone core of H3 and a single stranded ncRNA. This kind of binding is assumed to happen in a 'heterochromatin-like' structure of euchromatin which is established for gene repression (Fig. 5.3, eu3; compare also Fig. 1.2 B). The more moderate, transient binding is again related to a partial binding to single interaction partners directly in euchromatin (Fig. 5.3, eu2).

The dynamic nature of HP1 fractions observed here suggests a continuous exchange of HP1 molecules and thus, provides a mechanism for regulating the chromatin conformation: Each time a HP1-dimer dissociates from chromatin, various regulatory factors, as for example activating histone modifiers, compete against HP1 for this binding site and therefore lead to either highly condensed or decondensed chromatin states and active or repressed genes, respectively (dynamic competition model, compare (Cheutin et al., 2003; Schmiedeberg et al., 2004)).

Furthermore, this high dynamic of HP1 is in concordance to the observed low affinity binding to single interaction partners (Eskeland et al., 2007) and thus, only different binding mechanisms together exhibit higher affinity and therefore allow stable binding as proposed for the HP1 fraction stably integrated into heterochromatin. Although HP1 is partly highly mobile it seems to be even an important structural factor of heterochromatin maintenance.

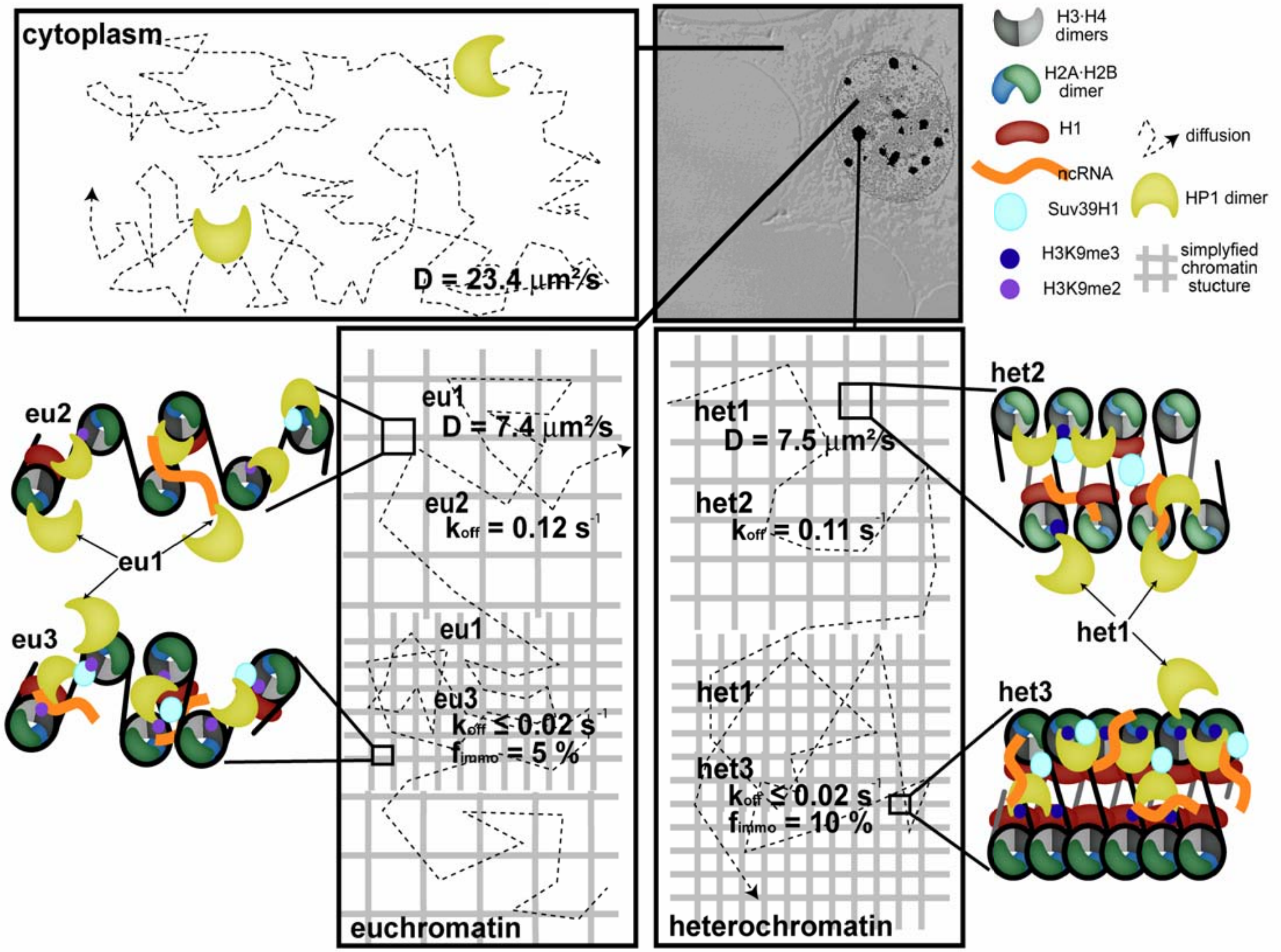

Figure 5.3: Kinetic model of HP1 mobility and interactions in the cell. A highly diffusive species was found in the cytoplasm. Within the nucleus different fractions of HP1 molecules were detected: A highly mobile fraction diffuses throughout the whole nucleus showing unspecific binding interactions (eu1 and het1, respectively); some HP1 molecules bind transiently to euchromatin or heterochromatin (eu2 and het2) and a third fraction is stably incorporated into chromatin via interaction with various binding partners (eu3 and het1). Values for diffusion coefficients and binding constants are given for HP1α. The simplified chromatin structure illustrates previously proposed density-states of chromatin.

5.5. FCS results for lysine specific demethylase 1

Measurements were carried out with two different homologues, human(h)- and mouse(m)-LSD1, both transfected into murine fibroblasts. In FCS measurements the concentration of LSD1 in different regions was estimated. Due to localization experiments that showed less staining in heterochromatin a lower concentration in this region was expected, but measured values do not fulfill this expectation, similar concentrations for both chromatin regions were obtained.

For mobility measurements in nucleoplasm two species were expected: A freely diffusive one, so as to spread the enzyme, and a second fraction that transiently binds to chromatin in order to demethylate either H3K9me2 in euchromatin or H3K9me3 in heterochromatin. However, in euchromatin only a single species was found. In heterochromatin, only the mLSD1 data gave some indication for a second species, human LSD1 showed no second decelerated species.

Measurements with mLSD1 revealed a fraction of LSD1 that had similar *D*-values within the whole cell, a second slower fraction was observed only in heterochromatin. Missing a second fraction of mLSD1 also in euchromatin and totally in measurements with hLSD1, a insufficiency in binding was proposed. A reduced binding affinity could depend on the location of the GFP fused to the N-terminus of hLSD1 or the lacking amino acids at the N-terminus of mLSD1.

So far no mobility measurements of LSD1 have been published and thus, further measurements have to be conducted, preferably with different, new cloned C-terminal GFP-fusions, to get reliable results.

5.6. Conclusions & perspectives

By now fluorescence recovery after photobleaching, FRAP, and fluorescence correlation spectroscopy, FCS, are well established methods to measure dynamics of molecules within living cells. However, until now they have mostly been applied as individual applications. Here, a combined FRAP and FCS approach was implemented to measure the mobility and interaction kinetics of macromolecules in a more comprehensive manner. Data analysis was enhanced to that effect, to extract values of interest, like diffusion coefficients and off-rates.

New insights were obtained with respect to determining diffusion, binding interactions, and immobilization of macromolecules in the nucleus in a spatially resolved manner.

The results obtained with this approach resulted in a comprehensive kinetic model describing the mobility and interaction behavior of HP1 in the cell nucleus that is summarized in Fig. 5.3. Three mobility states were identified and assigned to the different classes of binding sites of HP1. FCS and iFRAP allowed it to measure within small cellular regions and a high spatial resolution was obtained. Thus, a comparison of measurements in euchromatin and in heterochromatin revealed surprising results: The characteristic kinetic constants of HP1 mobility in euchromatin and in heterochromatin displayed only minor differences. The off-rates were essentially equal in both regions. These results and the only 2-fold higher immobile fractions can be explained simply by the higher amount of binding sites within heterochromatin. Therefore, the results obtained in this thesis are in contrast to the current concept of HP1 accumulation in heterochromatin due to the presence of high affinity binding sites only in this region.

As differences in organization and function of euchromatin and heterochromatin cannot be explained by HP1 accumulation or dynamics, further experiments should be conducted investigating differences in binding partners and functionality. This approach can be done in double-staining experiments like FRET (fluorescence resonance energy transfer) or in an extension of FCS, fluorescence cross-correlation spectroscopy could provide information.

A further improvement of the HP1 model was obtained by FCS measurements: Until now quantitative FCS measurements were carried out only in euchromatin and only for one component a diffusion constant was reported (Schmiedeberg et al., 2004). Their estimated diffusion coefficients were very small and the formation of large aggregates with HP1 was proposed, but not quantitatively investigated. The diffusion times reported suggest the existence of large HP1-loaded complexes of hundreds of MDa in size. However, no other evidence has been published for the existence of such large complexes containing HP1.

In contrast, in this thesis all HP1 species have been characterized quantitatively. Beneath the mobile fraction, the data indicate the existence of a component stably integrated into chromatin that displays confined translocation in its chromatin bound form. For the kinetic off-rates of the stably bound component a lower limit of $k_{off} = 0.02\ \mathrm{s}^{-1}$ was determined.

Further complementary experiments could be conducted that are particularly suited to investigate binding site dissociation, e.g. FLIP or CP.
The knowledge of the stable integration of HP1 into chromatin loops can possibly be used to extend the approach to investigate the mobility of these chromatin loops.

HP1 can be regarded as a central heterochromatin protein, as it is able to bind to a lot of different binding domains and therefore is assumed to work as assembly platform for different heterochromatin proteins. Here, its mobility and binding interactions were identified and a model was proposed that involves the different binding partners as methylated histones, HMTases, ncRNA etc. To get an overall picture of HP1 binding and functionality in chromatin organization, also the various interaction partners and binding sites of HP1 have to be investigated in a more detailed way in *in vivo* measurements. For two of them, namely ncRNAs and the histone demethylase LSD1, first interesting results were presented in this work and motivate to proceed.

References

Axelrod, D., D.E. Koppel, J. Schlessinger, E. Elson, and W.W. Webb. 1976. Mobility measurement by analysis of fluorescence photobleaching recovery kinetics. *Biophys J.* 16:1055-69.

Bannister, A.J., and T. Kouzarides. 2005. Reversing histone methylation. *Nature*. 436:1103-6.

Beaudouin, J., F. Mora-Bermúdez, T. Klee, N. Daigle, and J. Ellenberg. 2006. Dissecting the contribution of diffusion and interactions to the mobility of nuclear proteins. *Biophys. J.* 90:1878-94.

Berg, O.G., and P.H. von Hippel. 1985. Diffusion-controlled macromolecular interactions. *Annual Review of Biophysics and Biophysical Chemistry*. 14:131-160.

Bornfleth, H., K. Sätzler, R. Eils, and C. Cremer. 1998. High precision distance measurements and volume-conserving segmentation of objects near and below the resolution limit in three-dimensional confocal fluorescence microscopy. *Journal of Microscopy*. 189:118-136.

Cantor, C.R., and P.R. Schimmel. 1980. Biophysical Chemistry. Part II: Techniques for the Study of Biological Structure and Function. Freeman, New York.

Carrero, G., D. McDonald, E. Crawford, G. de Vries, and M.J. Hendzel. 2003. Using FRAP and mathematical modeling to determine the in vivo kinetics of nuclear proteins. *Methods*. 29:14-28.

Case, D.A., T.A. Darden, T.E.I. Cheatham, C.L. Simmerling, J. Wang, R.E. Duke, R. Luo, K.M. Merz, D.A. Pearlman, M. Crowley, R. Walker, W. Zhang, B. Wang, S. Hayik, A. Roitberg, G. Seabra, K.F. Wong, F. Paesani, X. Wu, S. Brozell, V. Tsui, H. Gohlke, L. Yang, C. Tan, J. Mongan, V. Hornak, G. Cui, P. Beroza, D.H. Mathews, C. Schafmeister, W.S. Ross, and P.A. Kollman. 2006. Amber 9. University of California, San Francisco.

Cheutin, T., A.J. McNairn, T. Jenuwein, D.M. Gilbert, P.B. Singh, and T. Misteli. 2003. Maintenance of stable heterochromatin domains by dynamic HP1 binding. *Science*. 299:721-5.

Cremer, T., and C. Cremer. 2001. Chromosome Territories, Nuclear Architecture and Gene Regulation in Mammalian Cells. *Nature Reviews Genetics*. 2:292-301.

Cremer, T., and C. Cremer. 2006. Rise, fall and resurrection of chromosome territories: a historical perspective Part II. Fall and resurrection of chromosome territories during the 1950s to 1980s. Part III. Chromosome territories and the functional nuclear architecture: experiments and models from the 1990s to the present. *European journal of histochemistry*. 50:223-72.

Daujat, S., U. Zeissler, T. Waldmann, N. Happel, and R. Schneider. 2005. HP1 binds specifically to Lys26-methylated histone H1.4, whereas simultaneous Ser27 phosphorylation blocks HP1 binding. *J Biol Chem*. 280:38090-5.

Davidson, M.W., and M. Abramowitz. 1999. Optical Microscopy. National High Magnetic Field Laboratory, The Florida State University, Tallahassee, Florida.

Day, R.N. 2005. Imaging protein behavior inside the living cell. *Mol Cell Endocrinol*. 230:1-6.

Dialynas, G.K., S. Terjung, J.P. Brown, R.L. Aucott, B. Baron-Luhr, P.B. Singh, and S.D. Georgatos. 2007. Plasticity of HP1 proteins in mammalian cells. *J Cell Sci*. 120:3415-24.

Edidin, M., Y. Zagyansky, and T.J. Lardner. 1976. Measurement of membrane protein lateral diffusion in single cells. *Science*. 191:466-8.

Eigen, M., and R. Rigler. 1994. Sorting single molecules: Application to diagnostics and evolutionary biotechnology. *Proc. Natl Acad. Sci. USA*. 91:5740-5747.

Elson, E.L., and D. Magde. 1974. Fluorescence correlation spectroscopy. I. Conceptual basis and theory. *Biopolymers*. 13:1-27.

Eskeland, R., A. Eberharter, and A. Imhof. 2007. HP1 binding to chromatin methylated at H3K9 is enhanced by auxiliary factors. *Molecular and cellular biology*. 27:453-65.

Felsenfeld, G., and M. Groudine. 2003. Controlling the double helix. *Nature*. 421:448-53.

Festenstein, R., S.N. Pagakis, K. Hiragami, D. Lyon, A. Verreault, B. Sekkali, and D. Kioussis. 2003. Modulation of heterochromatin protein 1 dynamics in primary Mammalian cells. *Science*. 299:719-21.

Gamble, M.J., and W.L. Kraus. 2007. Visualizing the histone code on LSD1. *Cell*. 128:433-4.

Garcia-Bassets, I., Y.S. Kwon, F. Telese, G.G. Prefontaine, K.R. Hutt, C.S. Cheng, B.G. Ju, K.A. Ohgi, J. Wang, L. Escoubet-Lozach, D.W. Rose, C.K. Glass, X.D. Fu, and M.G. Rosenfeld. 2007. Histone methylation-dependent mechanisms impose ligand dependency for gene activation by nuclear receptors. *Cell*. 128:505-18.

Garcia De La Torre, J., M.L. Huertas, and B. Carrasco. 2000. Calculation of hydrodynamic properties of globular proteins from their atomic-level structure. *Biophysical Journal*. 78:719-730.

Görisch, S.M., P. Lichter, and K. Rippe. 2005. Mobility of multi-subunit complexes in the nucleus: chromatin dynamics and accessibility of nuclear subcompartments. *Histochemistry and Cell Biology*. 123:217-228.

Görisch, S.M., M. Wachsmuth, C. Ittrich, C.P. Bacher, K. Rippe, and P. Lichter. 2004. Nuclear body movement is determined by chromatin accessibility and dynamics. *Proceedings of the National Academy of Sciences of the USA*. 101:13221-13226.

Grewal, S.I., and S.C. Elgin. 2007. Transcription and RNA interference in the formation of heterochromatin. *Nature*. 447:399-406.

Grewal, S.I., and D. Moazed. 2003. Heterochromatin and epigenetic control of gene expression. *Science*. 301:798-802.

Haustein, E., and P. Schwille. 2003. Ultrasensitive investigations of biological systems by fluorescence correlation spectroscopy. *Methods*. 29:153-66.

Hediger, F., and S.M. Gasser. 2006. Heterochromatin protein 1: don't judge the book by its cover! *Curr Opin Genet Dev*. 16:143-50.

Heitz, P. 1928. Das Heterochromatin der Moose. *Jahrb Wiss Botanik*. 69:762818.

Hell, S. 2007. Far-field optical nanoscopy. *Science*. 316:1153-8.

Hell, S.W. 2003. Toward fluorescence nanoscopy. *Nat Biotechnol*. 21:1347-55.

Heuvelman, G.L. 2008. Development and design of a spatially and temporally resolved fluorescence fluctuation microscope for the analysis of molecular mobilities and interactions. *In* Fakultät für Physik und Astronomie. Ruprecht-Karls-Universität Heidelberg, Heidelberg.

Hiragami, K., and R. Festenstein. 2005. Heterochromatin protein 1: a pervasive controlling influence. *Cell Mol Life Sci*. 62:2711-26.

Humphrey, W., A. Dalke, and K. Schulten. 1996. VMD: visual molecular dynamics. *J Mol Graph*. 14:33-8, 27-8.

Jenuwein, T., and C.D. Allis. 2001. Translating the histone code. *Science*. 293:1074-80.

Kim, S.A., K.G. Heinze, and P. Schwille. 2007. Fluorescence correlation spectroscopy in living cells. *Nat Methods*. 4:963-73.

Knippers, R. 1997. Molekulare Genetik. Thieme Verlag, Stuttgart.

Kouzarides, T. 2007. Chromatin modifications and their function. *Cell*. 128:693-705.

Krouwels, I.M., K. Wiesmeijer, T.E. Abraham, C. Molenaar, N.P. Verwoerd, H.J. Tanke, and R.W. Dirks. 2005. A glue for heterochromatin maintenance: stable SUV39H1 binding to heterochromatin is reinforced by the SET domain. *The Journal of cell biology*. 170:537-49.

Magde, D., E.L. Elson, and W.W. Webb. 1974. Fluorescence correlation spectroscopy. II. An experimental realization. *Biopolymers*. 13:29-61.

Maison, C., and G. Almouzni. 2004. HP1 and the dynamics of heterochromatin maintenance. *Nature Reviews Molecular Cell Biology*. 5:296-304.

Maiti, S., U. Haupts, and W.W. Webb. 1997. Fluorescence correlation spectroscopy: diagnostics for sparse molecules. *Proceedings of the National Academy of Sciences of the USA*. 94:11753-11757.

McNally, J.G. 2008. Quantitative FRAP in analysis of molecular binding dynamics in vivo. *Methods Cell Biol*. 85:329-51.

Merzlyak, E.M., J. Goedhart, D. Shcherbo, M.E. Bulina, A.S. Shcheglov, A.F. Fradkov, A. Gaintzeva, K.A. Lukyanov, S. Lukyanov, T.W. Gadella, and D.M. Chudakov. 2007. Bright monomeric red fluorescent protein with an extended fluorescence lifetime. *Nat Methods*. 4:555-7.

Metzger, E., M. Wissmann, N. Yin, J.M. Muller, R. Schneider, A.H. Peters, T. Gunther, R. Buettner, and R. Schule. 2005. LSD1 demethylates repressive histone marks to promote androgen-receptor-dependent transcription. *Nature*. 437:436-9.

Minc, E., Y. Allory, H.J. Worman, J.C. Courvalin, and B. Buendia. 1999. Localization and phosphorylation of HP1 proteins during the cell cycle in mammalian cells. *Chromosoma*. 108:220-34.

Minsky, M. 1957. Microscopy apparatus, USA.

Muelhardt, C. 2003. Der Experimentator: Molekularbiologie/Genomics. Spektrum Akademischer Verlag, Heidelberg, Berlin.

Murray, J.M. 2005. Confocal Microscopy, Deconvolution, and Structured Illumination Methods. *In* Live Cell Imaging - A laboratory manual. D.L.S. R.D. Goldman, editor. Cold Spring Harbor Laboratory Press, Cold Spring Harbor, New York. 239-279.

Ormo, M., A.B. Cubitt, K. Kallio, L.A. Gross, R.Y. Tsien, and S.J. Remington. 1996. Crystal structure of the Aequorea victoria green fluorescent protein [see comments]. *Science*. 273:1392-5.

Pack, C., K. Saito, M. Tamura, and M. Kinjo. 2006. Microenvironment and effect of energy depletion in the nucleus analyzed by mobility of multiple oligomeric EGFPs. *Biophys J*. 91:3921-36.

Pearlman, D.A., D.A. Case, J.W. Caldwell, W.R. Ross, T.E. Cheatham III, S. DeBolt, D. Ferguson, G. Seibel, and P. Kollman. 1995. AMBER, a computer program for applying molecular mechanics, normal mode analysis, molecular dynamics and free energy calculations to elucidate the structures and energies of molecules. *Comp. Phys. Commun.* . 91:1-41.

Rabut, G., and J. Ellenberg. 2005. Confocal Microscopy, Deconvolution, and Structured Illumination Methods. *In* Live Cell Imaging - A laboratory manual. D.L.S. R.D. Goldman, editor. Cold Spring Harbor Laboratory Press, Cold Spring Harbor, New York. 101-126.

Reymann, J., D. Baddeley, M. Gunkel, P. Lemmer, W. Stadter, T. Jegou, K. Rippe, C. Cremer, and U. Birk. 2008. High precision structural analysis of subnuclear complexes in fixed and living specimens via Spatially Modulated Illumination (SMI) microscopy. *Chromosome Research*. under revision.

Rigler, R., Ü. Mets, J. Widengren, and P. Kask. 1993. Fluorescence correlation spectroscopy with high count rate and low background: analysis of translational diffusion. *European Biophysics Journal*. 22:169-175.

Rippe, K. 2007. Dynamic organization of the cell nucleus. *Current opinion in genetics & development*. 17:373-380.

Rippe, K., J. Mazurkiewicz, and N. Kepper. 2008. Interactions of histones with DNA: nucleosome assembly, stability and dynamics. *In* DNA interactions with polymers and surfactants. R.S. Dias and B. Lindman, editors. Wiley, London. 135-172.

Schmiedeberg, L., K. Weisshart, S. Diekmann, G. Meyer Zu Hoerste, and P. Hemmerich. 2004. High- and low-mobility populations of HP1 in heterochromatin of mammalian cells. *Mol Biol Cell*. 15:2819-33.

Schneider, R., A.J. Bannister, and T. Kouzarides. 2002. Unsafe SETs: histone lysine methyltransferases and cancer. *Trends Biochem Sci*. 27:396-402.

Schwille, P. 2001. Fluorescence Correlation Spectroscopy and Its Potential for Intracellular Applications. *Cell Biochemistry and Biophysics*. 34:383-408.

Schwille, P., and E. Haustein. 2002. Fluorescence Correlation Spectroscopy: An Introduction to its Concepts and Applications, Göttingen.

Sprague, B.L., and J.G. McNally. 2005. FRAP analysis of binding: proper and fitting. *Trends Cell Biol*. 15:84-91.

Strahl, B.D., and C.D. Allis. 2000. The language of covalent histone modifications. *Nature*. 403:41-45.

Tewes, M. 1998. Aufbau eines Experiments zur Fluoreszenzkreuzkorrelationsspektroskopie, Erweiterung der theoretischen Grundlagen und biologische Anwendungen. *In* Fakultät für Physik und Astronomie. Ruprecht-Karls-Universität Heidelberg, Heidelberg.

Tsien, R.Y. 1998. The green fluorescent protein. *Annu. Rev. Biochem.* 67:509-44.

van Holde, K.E. 1989. Chromatin. Springer, Heidelberg.

Wachsmuth, M. 2001. Fluoreszenzfluktuationsmikroskopie: Entwicklung eines Prototyps, Theorie und Messung der Beweglichkeit von Biomolekülen im Zellkern. *In* Fakultät für Physik und Astronomie. Ruprecht-Karls-Universität Heidelberg, Heidelberg.

Wachsmuth, M., M. Caudron-Herger, and K. Rippe. 2008a. Genome Organization: Combining stability, plasticity and specificity. *submitted*.

Wachsmuth, M., T. Jegou, U. Nehrbass, and K. Rippe. 2008b. Differences in dynamics of hetero- and euchromatin as revealed by fluorescence correlations spectroscopy of linker histone H1. *Submitted.*

Wachsmuth, M., W. Waldeck, and J. Langowski. 2000. Anomalous diffusion of fluorescent probes inside living cell nuclei investigated by spatially-resolved fluorescence correlation spectroscopy. *Journal of Molecular Biology*. 298:677-689.

Wachsmuth, M., T. Weidemann, G. Muller, U.W. Hoffmann-Rohrer, T.A. Knoch, W. Waldeck, and J. Langowski. 2003. Analyzing intracellular binding and diffusion with continuous fluorescence photobleaching. *Biophysical Journal*. 84:3353-63.

Wachsmuth, M., and K. Weisshardt. 2007. Fluorescence Photobleaching and Fluorescence Correlation Spectroscopy: Two Contemplementary Technologies To Study Molecular Dynamics in Living Cells. *In* Imaging Cellular and Molecular Biological Functions. S.L. Shorte and F. Frischknecht, editors. Springer Verlag, Berlin, Heidelberg. 183-234.

Weidemann, T. 2002. Quantitative Untersuchung der Verteilung, Mobilität und Bindung von fluoreszenzmarkierten Histonen in vitro und in vivo mit Fluoreszenzfluktuationsmikroskopie. *In* Fakultät für Biowissenschaften. Ruprecht-Karls-Universität Heidelberg, Heidelberg.

Weidemann, T., M. Wachsmuth, T.A. Knoch, G. Muller, W. Waldeck, and J. Langowski. 2003. Counting nucleosomes in living cells with a combination of fluorescence correlation spectroscopy and confocal imaging. *Journal of Molecular Biology*. 334:229-240.

Yamamoto, K., and M. Sonoda. 2003. Self-interaction of heterochromatin protein 1 is required for direct binding to histone methyltransferase, SUV39H1. *Biochemical and biophysical research communications*. 301:287-92.

Zlatanova, J., and K. van Holde. 1996. The linker histones and chromatin structure: new twists. *Progress in Nucleic Acid Research and Molecular Biology*. 52:217-259.

Acknowledgements

Von Herzen möchte ich mich bei all jenen bedanken, die mich während meiner Arbeit unterstützt haben und mir immer mit Rat und Tat zur Seite standen.

PD Dr. Karsten Rippe danke ich für die Möglichkeit meine Diplomarbeit in seiner interdisziplinären Arbeitsgruppe und diesem tollen Team durchführen zu können. Vielen Dank für die nette Betreuung und die Unterstützung während dieser Zeit.

Recht herzlich möchte ich mich bei Herrn Prof. Dr. Dr. Christoph Cremer für das Interesse an dieser Arbeit und für die Unterstützung seitens der physikalischen Fakultät bedanken.

Bei Dr. Maiwen Caudron-Herger und Caroline Marth möchte ich mich besonders für die nette Betreuung im Labor bedanken. Caro, vielen lieben Dank für deine geduldige Einführung in die ‘Trickkiste’ der Molekularbiologie! Liebe Maiwen, unsere Zusammenarbeit während der ganzen Zeit hat sehr viel Spaß gemacht und ließ auch die vielen Stunden ‘im dunklen Kämmerchen’ nie langweilig werden.

Dr. Malte Wachsmuth und Dr. Joël Beaudouin danke ich für die Einführung in die FCS und FRAP, außerdem für die große Unterstützung bei der Datenanalyse.

Gerrit Heuvelman und Dr. Nick Kepper danke ich für die Unterstützung durch die Matlab-Programmierung und bei der Modellierungsarbeit. Auch möchte ich mich bei Sabine Kaltofen für die Überlassung ihrer Modellierungsergebnisse bedanken.

Fabian Erdel möchte ich für die schnelle Mikroskopie-Hilfe am Ende meiner Arbeit danken.

Allen Mitgliedern des chromcon-Teams möchte ich für die stete Hilfsbereitschaft, die großartige Unterstützung und den Spaß im Labor danken. Die gemeinsamen ‘kreativen Pausen’ waren einfach unschlagbar.

Bei Agnes Wyzgol möchte ich mich für das sehr gewissenhafte Korrekturlesen und ihre großartige Freundschaft bedanken.

Mein größter Dank gilt meiner Familie für die uneingeschränkte und liebevolle Unterstützung, nicht nur während dieser Diplomarbeit, sondern während des gesamten Studiums. Ohne eure Liebe und eure aufmunternden Worte und Gesten wäre mir manches nicht so gut gelungen, ihr habt mir das Alles erst ermöglicht.